TECHNISCHE UNIVERSITÄT MÜNCHEN
Lehrstuhl für Physik funktionaler Schichtsysteme, E10

Torque magnetometry on graphene and Fermi surface properties of VB_2 and MnB_2 single crystals studied by the de Haas-van Alphen effect

Stephan Gerhard Albert

Vollständiger Abdruck der von der Fakultät für Physik der Technischen Universität München zur Erlangung des akademischen Grades eines

Doktors der Naturwissenschaften

genehmigten Dissertation.

Vorsitzender: Univ.-Prof. Dr. Martin Zacharias
Prüfer der Dissertation:
1. Univ.-Prof. Dr. Dirk Grundler
2. Univ.-Prof. Christian Pfleiderer, Ph. D.

Die Dissertation wurde am 24.02.2015 bei der Technischen Universität München eingereicht und durch die Fakultät für Physik am 23.03.2015 angenommen.

Short Abstract

Magnetic properties of two- and three-dimensional materials, id est large-area graphene and single crystals, respectively, of VB_2 and MnB_2, are studied at low temperatures and in high magnetic fields by torque magnetometry. Magnetic quantum oscillations are not observed for five differing graphene samples, consistent with sample quality available to date. Single crystals of VB_2 and MnB_2 of large size and unprecedented crystalline quality exhibit a pronounced de Haas-van Alphen effect. We report the angular and temperature dependencies of two de Haas-van Alphen frequencies for each crystal. They allow us to make a detailed comparison with band structure calculations and the isostructural compounds CrB_2 and MgB_2.

Es werden magnetische Eigenschaften von zwei- und dreidimensionalen Materialien, nämlich großflächiges Graphen und VB_2- und MnB_2-Einkristalle, bei tiefen Temperaturen und in hohen Magnetfeldern mit Drehmoment-Magnetometrie untersucht. Magnetische Quantenoszillationen werden für fünf verschiedenartige Graphen-Proben in Übereinstimmung mit heute verfügbarer Qualität nicht beobachtet. Große VB_2- und MnB_2-Einkristalle mit außergewöhnlicher Qualität weisen einen ausgeprägten de-Haas-van-Alphen-Effekt auf. Wir zeigen die Winkel- und Temperaturabhängigkeit von jeweils zwei de-Haas-van-Alphen-Frequenzen. Dies ermöglicht einen Vergleich mit Bandstrukturdaten und den isostrukturellen Verbindungen CrB_2 und MgB_2.

Abstract

Technological innovation relies on the continuous research of novel materials. If techniques for scalable growth, reliable manipulation of material properties, and integration of different materials are developed, novel materials can ultimately lead to new tailored device applications with new functionalities and superior performance compared to existing technologies.
The electronic structure is at the heart of many properties of a material. Investigation of the de Haas-van Alphen (dHvA) effect, the quantum oscillations of magnetization, allows to directly probe the electronic structure at the Fermi surface. In this thesis, we employ highly sensitive torque cantilever magnetometry at low temperatures and in high magnetic fields to study the magnetization of three different novel materials: large-area samples of graphene and single crystals of vanadium diboride (VB_2) and manganese diboride (MnB_2). Additionally, we design and implement a new experimental setup for cantilever magnetometry with an interferometric readout scheme. The following results are obtained:

- **Magnetometry experiments on large-area graphene samples:** Torque magnetometry experiments at temperatures down to 280 mK and in fields up to 15 T are performed on five different types of large-area graphene samples: graphene, grown by chemical vapor deposition (CVD), monolithically integrated with the employed cantilever sensor; CVD-grown graphene on a silicon substrate with a thermal silicon oxide layer; epitaxial monolayer graphene (MLG) on the silicon terminated side of $6H$-silicon carbide substrates of two differing thicknesses; quasifree-standing monolayer graphene (QFMLG) with an intercalated hydrogen layer on the silicon terminated side of $6H$-silicon carbide. None of the different approaches provides a signal that can be attributed to the respective graphene layer. It is concluded that presently large-area graphene samples have an electronic quality and homogeneity that is not sufficient for the observation of magnetic quantum oscillations.

- **Sample head for cantilever magnetometry with interferometric readout:** An experimental sample head to be used in a vacuum loading ^{3}He system for cantilever magnetometry experiments with an interferometric readout scheme is designed and implemented along the following guidelines: integration into an existing ^{3}He system and use in existing superconducting solenoids, sample fine-positioning allowing for a sub-micrometer control and stability of translation in three directions and a tilt compensation with 0.02° resolution, and sub-angstrom readout sensitivity of the cantilever position.

- **Investigation of the dHvA effect of VB_2:** We study the angular, temperature, and field dependence of the dHvA effect of a VB_2 single crystal at temperatures down to 280 mK and in magnetic fields up to 15 T. Two distinct dHvA frequencies are observed, one of which belongs to a closed extremal orbit and the other to an open extremal orbit on the Fermi surface of VB_2. Comparison with band structure calculations[1] suggests that both observed dHvA orbits stem from bands with a predominant V-d character. The measured effective masses are enhanced over the calculated band masses by factors of 1.6 and 1.4, respectively. This allows us to estimate upper bounds of the electron phonon coupling constant for V-d-derived bands of 0.4-0.6.

- **Investigation of the dHvA effect of MnB_2:** We study the angular, temperature, and field dependence of the dHvA effect of a MnB_2 single crystal at temperatures down to 280 mK and in magnetic fields up to 15 T. Two distinct dHvA frequencies are observed, both belonging to closed Fermi surface sheets. Comparison with band structure calculations[1], considering an antiferromagnetic ordering of consecutive Mn planes along the c-axis, suggests that both dHvA orbits originate from the same Fermi surface sheet and arise from a band with Mn-d character. The measured effective masses are enhanced over the calculated band masses by factors of 1.6 and 1.5, respectively. Accordingly, the derived upper bounds for the electron phonon coupling constant of the Mn-d-derived band is 0.5-0.6. An analysis of corresponding data for isostructural CrB_2 and MgB_2

[1] Density functional calculations were performed by Dr. Jan Kuneš, Institute of Physics, Academy of Sciences, Cukrovarnicka 10, Praha 6 16253, Czech Republic.

provided in literature reveals that VB_2, CrB_2, and MnB_2 share similar scales for the electron phonon coupling constant with MgB_2 depending on the B-p_{xy} contribution to the respective electronic states despite profound differences in the general electronic structures.

Contents

Scientific collaborations

Parts of this thesis have profited from scientific collaborations. The author would like to state the contributions by the respective researchers and research groups:

- The VB_2 and MnB_2 single crystals were grown and provided by Andreas Bauer and Alexander Regnat from the group of Prof. Christian Pfleiderer, Technische Universität München.
- Band structure calculations of VB_2 and antiferromagnetic MnB_2 were performed by Dr. Jan Kuneš, Academy of Sciences, Prague, Czech Republic.
- Samples of epitaxial graphene on SiC were grown by Florian Speck and Felix Fromm from the group of Prof. Thomas Seyller, formerly at Friedrich-Alexander-Universität Erlangen-Nürnberg, presently at Technische Universität Chemnitz.
- Samples of CVD-grown graphene were provided by Max Seifert and Lucas Hess from the group of PD José Antonio Garrido, Technische Universität München.
- GaAs/AlAs heterostructures for the preparation of micromechanical sensors were provided by Dr. Christian Heyn in the group of Prof. Wolfgang Hansen, Universität Hamburg, and by the group of Prof. Anna Fontcuberta i Morral, École Polytechnique Fédérale de Lausanne, Switzerland.
- MgZnO/ZnO heterostructures were provided by Dr. Yusuke Kozuka from the group of Prof. Masashi Kawasaki, University of Tokyo, Japan.

The author would like to express his gratitude for the productive collaboration.

1 Introduction

Much of the rapid technological progress of the 20th and the beginning 21st century has been driven by microelectronics and in particular the dramatic advances in semiconductor technology. In daily as well as professional life, we are surrounded by the products of this progress, such as computers, smartphones, digital cameras, flat TV screens, navigation systems, chip card systems, miniaturized sensors for a vast variety of purposes, et cetera. They have revolutionized our life and the economies of many countries are increasingly dependent on the corresponding industries. Much of this progress relies on the development of controlled growth processes of special materials, techniques to manipulate their properties, and the ability to integrate different materials with tailored physical characteristics in one device. However, while existing technologies and materials are pushed to their limits, a continuous search for alternatives is needed if technological innovation is to be maintained. For example, the semiconductor industry is primarily based on silicon. The famous empiric law of Moore [1] states that the number of transistors per area in an integrated circuit approximately doubles every two years. This prophecy has now been fulfilled for half a century with an astonishing precision. Yet, - like any real-world exponential growth - it will eventually hit limitations. There are fundamental physical limits imposed by thermodynamics, electrodynamics, and quantum dynamics [2]. But there are also limitations set by the material used and for this reason Moore's law cannot be maintained forever with silicon-based devices [3]. Therefore, a permanent research on novel materials for more powerful chips as well as other next-generation applications is essential.

One of the most intriguing materials of this kind is graphene, a sheet of carbon atoms considered to be the first two-dimensional crystal. Since its existence has been experimentally proven [4] and methods for large-scale growth have been demonstrated [5, 6], graphene has attracted an unprecedented attention of scientific and industrial research [7]. The European Union has decided to fund graphene related research with one billion euro over a period of ten years [8]. Because of its unusual properties, such as

extraordinary electrical and thermal conductivity, high electron mobility, and mechanical robustness, it holds promise for numerous applications. For example, it could be used as a conductive, yet transparent layer in displays, dissipate energy in integrated circuits, be implemented in novel types of biosensors [9], and maybe even become a substitute for silicon in transistors when patterned [10] or combined to heterostructures with other materials [11].
Another class of candidates for future technological advances are materials hosting correlated electron systems. The term "correlation" describes a mutual relationship between the electrons, i. e. that they cannot be viewed as independent from each other in a single-particle picture, which is possible in silicon and graphene in good approximation. Rather, their mutual influence must be considered to correctly describe the material's properties. Electronic correlations give rise to macroscopic quantum phenomena, such as superconductivity and (anti-)ferromagnetism. Thus, electronic correlations can alter the properties of materials dramatically, giving rise to novel ground states and thereby paving the way for possible novel functionality. It is thus not surprising that much of the recent research towards innovation on the material level has focused on materials with correlated electron systems. Vanadium diboride (VB_2), chromium diboride (CrB_2) [12, 13], and manganese diboride (MnB_2), three representatives of the class of transition metal diborides, are isostructural and differ mainly by the addition of an extra electron when the atomic number of the transition metal constituent is increased from vanadium over chromium to manganese. Yet, they have three different magnetic ground states [14, 15]. Furthermore, they are isostructural to superconducting MgB_2, which has the highest known transition temperature of all conventional phonon-mediated superconductors [16]. They are hence an interesting object of study for the electronic requirements of the two correlation phenomena of magnetic ordering and superconductivity.
A key ingredient in the understanding of most macroscopic properties of a material is the knowledge of its electronic structure as given by its dispersion relation. Thereby, electrons directly located at the Fermi energy define the properties. The de Haas-van Alphen (dHvA) effect [17], i. e. the oscillations of magnetization as a function of inverse magnetic field as a purely quantum mechanical phenomenon, is a powerful tool to map out the Fermi surface, i. e. the electronic states at the Fermi energy. In this thesis, torque cantilever magnetometry has been employed to study graphene and

the dHvA effect of VB_2 and MnB_2.

The outline of this thesis is as follows: In Chapter 2, the theoretical derivation of the dHvA effect of bulk electron systems is sketched and the framework for the interpretation of the dHvA effect is introduced. Chapter 3 is dedicated to the presentation of torque cantilever magnetometry, which is the measurement technique employed in this thesis for the study of graphene, VB_2, and MnB_2. A treatment of the mechanical properties of the specific cantilever sensors used in this thesis, which is relevant for the interpretation of the experimental data, is included. In Chapter 4, numerical calculations of the dHvA effect in graphene and different approaches for the experimental study of the dHvA effect in graphene are presented. One of these approaches is exemplified and the absence of a dHvA signal in the experimental data is discussed. In Chapter 5, we describe the design and implementation of an experimental setup for torque cantilever magnetometry with interferometric readout. Chapter 6 gives an introduction to the class of transition metal diborides and specifically to the investigated representatives VB_2 and MnB_2. Chapter 7 discusses measurements of the dHvA effect in VB_2, the extraction of dHvA frequencies from band structure calculations, and properties of the Fermi surface topology as inferred from angle-dependent measurements and calculations. Additionally, the analysis of the temperature and field dependence of the dHvA effect allows for the determination of the effective masses of the charge carriers as well as the associated mean free paths. In Chapter 8, measurements of the dHvA effect in MnB_2 are reported. The study of the angular, temperature, and field dependence of the dHvA effect provides valuable information on the Fermi surface topology of MnB_2 as well as effective masses of charge carriers along with mean free paths. The measured properties are compared to the respective quantities as extracted from band structure calculations. A synoptic discussion of dHvA measurement results, Fermi surface properties, and electronic states of VB_2, CrB_2, MnB_2, and MgB_2 is included. Finally, a summary of the results and a brief outlook is given in Chapter 9.

2 Theoretical concepts

In this chapter, fundamental theoretical concepts, which are relevant for the understanding of the experimental results obtained in this thesis, are introduced. The experimental results are based on the observation of the de Haas-van Alphen effect. This effect is the phenomenon of quantum oscillations in the magnetization of an electron system. It was first observed in bismuth by de Haas and van Alphen in 1930 [17]. We sketch the theoretical derivation of the de Haas-van Alphen effect by starting from the Landau quantization of free electrons in a magnetic field in Sec. 2.1. This is followed by a qualitative explanation for the appearance of quantum oscillations in general (Sec. 2.2) and a more quantitative treatment of magnetic oscillations in particular (Sec. 2.3). We then present the Lifshitz-Kosevich formalism considering finite temperature and disorder (Sec. 2.4), which is of great experimental importance, and introduce the nomenclature for highly anisotropic Fermi surfaces (2.5).

2.1 Landau quantization of free electrons in a magnetic field

The Landau quantization of free electrons (or any other charged particles) in a magnetic field lies at the heart of quantum oscillatory phenomena. The derivation can be found in standard textbooks (e. g. Ref. [18]). Because of its central role in this thesis, we recapitulate the derivation below.
For this, we consider a free electron of charge $-e$ (e is the positive elementary charge) travelling in a constant magnetic field $\mathbf{B}$. The Hamiltonian of this electron is given by

$$H = \frac{1}{2m_\mathrm{e}} \left(\mathbf{p} + e \cdot \mathbf{A}\right)^2 , \tag{2.1}$$

where m_e is the electron mass, $\mathbf{p} = \frac{\hbar}{\mathrm{i}} \nabla$ the momentum operator, and $\mathbf{A}$ the vector potential, which is related to $\mathbf{B}$ by $\mathbf{B} = \nabla \times \mathbf{A}$. The operator $\mathbf{P} = \mathbf{p} + e \cdot \mathbf{A}$ is called the canonical momentum. Without loss of gen-

erality, we assume the field to be oriented along the z-axis, $\mathbf{B} = B\hat{e}_z$. In the symmetric gauge, the vector potential is $\mathbf{A} = \frac{1}{2}(-yB, xB, 0)$. The Hamiltonian Eq. 2.1 then decomposes into two commuting terms

$$H = H_\perp + H_z, \quad \text{with} \tag{2.2}$$

$$H_\perp = \frac{1}{2m_\mathrm{e}}\left(P_x^2 + P_y^2\right), \tag{2.3}$$

$$H_z = \frac{1}{2m_\mathrm{e}}p_z^2. \tag{2.4}$$

The component H_z of the Hamiltonian is solved by plane waves $\exp(\mathrm{i}k_z z)$, i. e. the degree of freedom associated with the motion of the electron in the z-direction is unaffected by the magnetic field. We perform a simple transformation of the canonical momentum operators by rescaling

$$\pi_i = \frac{1}{\sqrt{eB}}P_i, \quad i \in \{x, y\}. \tag{2.5}$$

The Hamiltonian $H_\perp$ then takes the form

$$H_\perp = \frac{1}{2}\frac{eB}{m_\mathrm{e}}\left(\pi_x^2 + \pi_y^2\right). \tag{2.6}$$

It is easily shown that the new operators obey the commutation relations

$$[\pi_y, \pi_x] = \mathrm{i}\hbar, \quad [\pi_x, \pi_x] = [\pi_y, \pi_y] = 0. \tag{2.7}$$

The Hamiltonian of Eq. 2.6 and the commutation rules for π_x and π_y resemble the corresponding equations for the one-dimensional harmonic oscillator with conventional operators $\hat{x}$ and $\hat{p}$ for space coordinate and momentum. By defining operator a and its Hermitian conjugate $a^\dagger$

$$a = \frac{\pi_y + \mathrm{i}\pi_x}{\sqrt{2\hbar}}, \qquad a^\dagger = \frac{\pi_y - \mathrm{i}\pi_x}{\sqrt{2\hbar}}, \tag{2.8}$$

the Hamiltonian Eq. 2.6 can be expressed in the standard form of the harmonic oscillator in terms of ladder operators

$$H_\perp = \hbar\omega_\mathrm{c}\left(a^\dagger a + \frac{1}{2}\right). \tag{2.9}$$

Here, we introduced the cyclotron frequency ω_c defined by

$$\omega_c = \frac{eB}{m_e}. \tag{2.10}$$

The eigenenergies of the combined Hamiltonian $H = H_\perp + H_z$ are

$$E = \left(n + \frac{1}{2}\right)\hbar\omega_c + \frac{(\hbar k_z)^2}{2m_e}, \quad \text{with} \quad n \in \mathbb{N}_0, \tag{2.11}$$

i. e. the sum of the eigenenergies of the one-dimensional harmonic oscillator (cf. e. g. Ref. [19]) and of the energy associated with the free motion in z-direction $\hbar^2 k_z^2/(2m_e)$. This result is the well known Landau quantization of free electrons in a magnetic field. While the movement of the electrons along the z-direction is unaffected by the magnetic field (in a classical picture the z-component of the Lorentz force vanishes), the wave numbers k_x and k_y are not good quantum numbers in the presence of the magnetic field anymore. Instead, the electrons have the energy quantization of the harmonic oscillator. The corresponding eigenenergies are called Landau levels. The above result can also be derived in a semi-classical picture for electrons moving in reciprocal space (K-space) by imposing the Bohr-Sommerfeld quantization. In this picture, the electrons move on circles perpendicular to the field in real and reciprocal space under the influence of the Lorentz force. Hereby, only discrete radii $k_\perp$ in K-space are allowed by the quantization rule. They are given by

$$\frac{\hbar^2 k_\perp^2}{2m_e} = \left(n + \frac{1}{2}\right)\hbar\omega_c. \tag{2.12}$$

2.2 The origin of quantum oscillations

After the derivation of the Landau quantization, we now turn to a qualitative explanation for the emergence of quantum oscillatory phenomena from the Landau quantization.
For free electrons in zero magnetic field, the states (k_x, k_y, k_z) in K-space are equidistantly spaced (where the exact spacing depends on the boundary conditions). In a magnetic field, however, the states for fixed k_z assem-

ble[1] on discrete circles with radii given by Eq. 2.12. If the k_z-axis is also considered, the circles become cylinders, the famous Landau tubes. The Landau levels are degenerate[2]. The degeneracy of the Landau levels can be derived by calculating the number of electron states in zero magnetic field which assemble on one Landau circle if the field is applied. Per unit area, the density of states in two-dimensional K-space is $1/(2\pi)^2$. This constant is multiplied by the annular difference area $\pi k_{\perp,n+1}^2 - \pi k_{\perp,n}^2$ of two neighboring Landau circles with quantum numbers n and $n+1$ in Eq. 2.12 to arrive at the Landau level degeneracy D_L per unit area

$$D_\mathrm{L} = \frac{eBg_\mathrm{s}}{2\pi\hbar}, \tag{2.13}$$

where g_s takes the spin degeneracy into account. It can be shown that this result is rigorously true for arbitrary dispersion relations [20]. Both the Landau energies and their degeneracies increase linearly with magnetic field B such that the number of states in a given K-space volume stays constant for arbitrary field strength B.

For a given Fermi energy E_F (i. e. N electrons in a given volume V) of the free electron gas at $T = 0$, only electron states inside a sphere in K-space with radius $k_\mathrm{F} \propto (N/V)^{1/3}$ are occupied. The surface of the sphere is referred to as Fermi surface. With magnetic field applied, this means that only those parts of the Landau tubes are occupied, which lie inside the sphere. This is sketched in Fig. 2.1 (a). In this picture, the origin of quantum oscillations can be understood qualitatively. For this, we consider a two-dimensional cross section of the Fermi sphere perpendicular to $\mathbf{B}$ with area $\mathcal{A}$ as depicted in Fig. 2.1 (b). The projection of the Landau tubes onto the cross section are Landau circles of radii $k_\perp$ implicitly given by Eq. 2.12 and the three-dimensional Fermi surface itself is represented by a Fermi circle (green) in this cross section. The Landau circles represent degenerate electron states of constant energy and only Landau

[1] Sometimes, the term "condense" is used in text books, which we avoid due to possible misleading associations.

[2] At this point, it is often omitted in textbooks what the second quantum number is when going from (k_x, k_y) in zero field to the Landau level index n. In fact, the second quantum number is X, which corresponds to the average spatial coordinate of the circles on which the electrons travel in a semiclassical picture. For this reason, it is not a contradiction to Pauli's exclusion principle that one Landau level can be occupied by more than one electron.

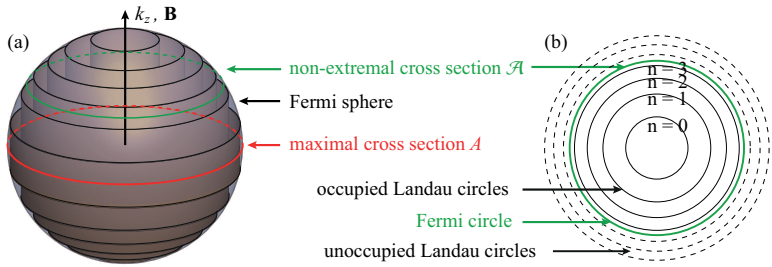

Figure 2.1: (a) Landau tubes in K-space inside the Fermi sphere of an isotropic free electron gas. The electron states are quantized on Landau tubes, which have a cylindrical shape along magnetic field $\mathbf{B}$. The surfaces of constant energy of the free electron gas are spherical. Only those parts of the Landau tubes inside a sphere of radius k_F corresponding to the Fermi energy E_F are occupied. A non-extremal cross section (green) and the maximal cross section (red) of the Fermi sphere are indicated. (b) Non-extremal cross section of the Landau tubes and of the Fermi surface . The Landau levels and the Fermi surface are represented by circles. Only Landau circles inside the Fermi circle are occupied (solid). The dashed Landau circles are not occupied.

circles within the Fermi circle are occupied. As B increases, the radii of the Landau circles grow and consequently the associated eigenenergies increase as well. Accordingly, also the total energy, given by the sum over the eigenenergies of the Landau circles within the Fermi circle multiplied by their degeneracy, increases. However, when a Landau circle crosses the Fermi circle, it is depleted and consequently the total energy decreases. When B is further increased, the process repeats. Hence, this process of growing Landau circles, which consecutively leave the cross-sectional area $\mathcal{A}$, constitutes a periodic behavior of the total energy[1]. By calculating the required field B_n for the n-th Landau circle to coincide with the Fermi circle, it is easily shown that the oscillatory behavior is periodic in $1/B$ with

[1] We note that in a rigorous treatment the considered two-dimensional case is slightly more involved if the total energy U is considered because oscillations of the chemical potential need to be taken into account to fix the total electron number. The explanation above is meant to provide an intuitive understanding of the origin of quantum oscillations, which is the periodic crossing of Landau levels through the Fermi energy. For this qualitative understanding, the explanation is adequate.

period $2\pi e/(\hbar\mathcal{A})$ or alternatively frequency

$$\mathcal{F} = \frac{\hbar\mathcal{A}}{2\pi e}. \tag{2.14}$$

Returning to the three-dimensional case of a spherical Fermi surface, the above considerations apply for any arbitrary cross-sectional slab of the sphere perpendicular to $\mathbf{B}$ with respective frequencies $\mathcal{F}$ given by their respective cross-sectional areas $\mathcal{A}$. However, the cumulative behavior of the slabs is totally dominated by so-called extremal cross sections. These are cross sections for which the cross-sectional area $\mathcal{A}(k_z)$ as a function of the K-space coordinate k_z parallel to $\mathbf{B}$ is stationary, i. e.

$$\frac{\partial\mathcal{A}}{\partial k_z} = 0. \tag{2.15}$$

In the case of a spherical Fermi surface, there is one extremal area, which is a maximal area. It is identical with the cross section through the center of the Fermi sphere, i. e. it is the cross-sectional circle with the same radius as the radius k_F of the Fermi sphere. In the following, we denote extremal cross sections by A (instead of $\mathcal{A}$) and their associated frequencies by f (instead of $\mathcal{F}$). The total dominance of extremal cross sections can be rigorously shown [20]. It can also be appreciated intuitively: The Landau tubes *intersect* the Fermi surface at non-extremal cross sections while the n-th Landau tube *touches* the Fermi surface at the extremal cross section for a corresponding field B_n in a tangential manner. If we consider the distribution of states on the Landau tubes in k_z-direction, it is clear that the states that coherently contribute to the frequency f associated with the extremal area A drastically outnumber other states belonging to non-extremal areas and frequencies, respectively. For this reason, only frequencies f associated with extremal cross sections A of the Fermi surface are of physical relevance. We restate Eq. 2.14 for this case:

$$f = \frac{\hbar A}{2\pi e}. \tag{2.16}$$

This is a famous result first derived by Onsager [21].
As qualitatively explained above, the total energy U of an electron system shows quantum oscillations in $1/B$ with periodicity given by Eq. 2.16.

Because the total energy is related to other thermodynamical potentials by Legendre transformations and physical observables are related to the thermodynamical potentials via partial derivatives, quantum oscillations in general exist for a variety of quantities. Most notable are the Shubnikov-de Haas effect for electrical conductivity and the de Haas-van Alphen oscillations for magnetization, whose derivation is sketched in the following section.

2.3 The de Haas-van Alphen effect

We now turn to the quantum oscillations of the magnetization of an electron system. These oscillations were first observed in bismuth by de Haas and van Alphen in 1930 [17] and the effect became to be known under the name of its discoverers although a quantum-mechanical understanding was not provided before Onsager's paper in 1952 [21]. In this section we constrain ourselves to stating some results of the derivation of the de Haas-van Alphen effect. For a formal derivation, which involves some subtle mathematical arguments, the reader is referred to Ref. [20]. The relations stated relate to zero temperature and zero Landau level broadening.
Most often, de Haas-van Alphen oscillations are examined in systems with fixed electron number N and at fixed temperature T. The thermodynamical potential associated with these conditions is the free energy F. It is related to the (internal) energy U by a Legendre transformation

$$F = U - TS, \tag{2.17}$$

where S is the entropy. The free energy F can be obtained by evaluating the associated canonical partition function Z_c. If the free energy F is known, the components of the magnetization can be derived by a partial differentation

$$M_i = -\left(\frac{\partial F}{\partial B_i}\right)_{N,T}. \tag{2.18}$$

However, for ensembles which obey Fermi-Dirac statistics, as for example electrons, the calculation of the canonical partition function Z_c is difficult because the fixed particle number imposes some troublesome constraints on the summation. Therefore, it is more convenient to abandon particle conservation and to consider the grand canonical ensemble Ω, which is

related to the free energy through another Legendre transformation

$$\Omega = F - \mu N. \tag{2.19}$$

The grand canonical ensemble is not a function of N anymore, but of the chemical potential μ. This means that the chemical potential μ is fixed instead of the particle number N. Its advantage is that the corresponding grand canonical partition function Z_g is easier to evaluate. The potential and the partition function are connected by $\Omega = -k_\mathrm{B}T \ln Z_\mathrm{g}$. For particles with single-particle energy states ϵ and the Fermi-Dirac statistics, this leads to [22, 23]

$$\Omega = -k_\mathrm{B}T \sum_\epsilon \ln\left[1 + \exp\left(\frac{\mu - \epsilon}{k_\mathrm{B}T}\right)\right], \tag{2.20}$$

where the sum runs over all single-particle energy states ϵ. At $T = 0$, the grand canonical potential is $\Omega = U - N\mu$ and the grand canonical potential for free electrons in a volume V in a magnetic field with the energy states $E_j(k_z)$ given in Eq. 2.11 becomes

$$\Omega = V \sum_j D_\mathrm{L} \int_0^{k_j} \frac{\mathrm{d}k_z}{2\pi} \left(E_j(k_z) - \mu\right), \tag{2.21}$$

where D_L is the degeneracy of the Landau levels including spin degeneracy (Eq. 2.13). Both the sum and the integral in Eq. 2.21 are constrained by the occupation: For given Landau level index j, the integral is to be taken from 0 to k_j, implicitly given by $\hbar^2 k_j^2/(2m) = \mu - (j + 1/2)\hbar\omega_\mathrm{c}$. The sum over j runs over values for which $(j + 1/2)\hbar\omega_\mathrm{c} < \mu$. Hereby, the condition of free electrons with a spherical Fermi surface can be relaxed to a parabolic dispersion characterized by a band mass m_b (replacing m_e) within the considered two-dimensional cross sections and to a Fermi surface arbitrarily shaped along k_z, i. e. not restricted to a sphere. Much of the involved mathematics, which continues the derivation from this point, is related to finding appropriate approximations of the sum in Eq. 2.21 by integrals, observing the constraints on the upper boundaries of the sum and the integral, and finally expressing the result in a Fourier series. Here we only state the result for the oscillatory part of the grand-canonical potential

Ω_{osc} for one extremal area A

$$\Omega_{\mathrm{osc}} = \text{const.} \times \frac{B^{5/2}}{\sqrt{A''}} \sum_{p=1}^{\infty} \frac{1}{p^{5/2}} \cos\left[2\pi p \frac{f}{B} + \phi_p\right]. \tag{2.22}$$

Here, the frequency f is defined by Eq. 2.16 for the considered extremal area A and ϕ_p is a phase depending on the harmonic of f, numbered by the sum index p. The prefactor $1/\sqrt{A''}$ contains the curvature of the cross-sectional area $\mathcal{A}$ as a function of k_z, i. e. along the field direction, at the position of the extremal cross section $k_z(A)$:

$$A'' \equiv \left| \frac{\partial^2 \mathcal{A}(k_z)}{\partial k_z^2} \right|_{k_z = k_z(A)}. \tag{2.23}$$

The prefactor expresses a circumstance that has already been discussed qualitatively: The lower the curvature at the extremal area is, the more intimate is the touching of a Landau tube with the Fermi surface, i. e. the larger is the interval along k_z of states on the tube that constructively contribute to the frequency of the extremal area. In the limiting case of a cylindrical Fermi surface, the cross-sectional area is constant along k_z and the curvature is zero. In this case all states on the Landau tube contribute to f.
The magnetization $\mathbf{M}$ is now obtained by taking the gradient derivative of Ω with respect to $\mathbf{B}$ at fixed chemical potential μ and temperature T

$$\mathbf{M} = -\left(\nabla_{\mathbf{B}} \Omega\right)_{\mu,T}. \tag{2.24}$$

When the gradient is considered in spherical coordinates, the components of $\mathbf{M}$ can be separated into a component $M_{\parallel}$ parallel to $\mathbf{B}$ (which we still assume to be oriented parallel to $\hat{e}_z$ w. l. o. g.) and two components $M_{\perp,x}$, $M_{\perp,y}$ in perpendicular directions $\hat{e}_x$, $\hat{e}_y$ to $\mathbf{B}$

$$M_{\parallel} = -\frac{\partial \Omega}{\partial B}, \tag{2.25}$$

$$M_{\perp,x} = -\frac{1}{B} \frac{\partial \Omega}{\partial \theta_x}, \tag{2.26}$$

$$M_{\perp,y} = -\frac{1}{B} \frac{\partial \Omega}{\partial \theta_y}, \tag{2.27}$$

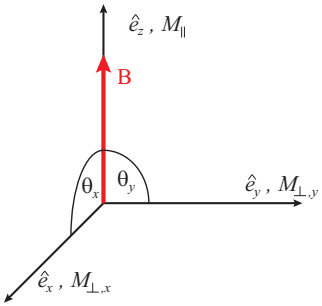

Figure 2.2: Definitions of the angles θ_x and θ_y with respect to the coordinate system, which serve for the derivation of the perpendicular components $M_{\perp,x}$ and $M_{\perp,y}$ from the grand canonical potential. The magnetic field $\mathbf{B}$ is assumed to be oriented along the z-axis w. l. o. g.

where θ_i denotes the angle of $\mathbf{B}$ in the plane spanned by $\hat{e}_z$ and $\hat{e}_i$, which is illustrated in Fig. 2.2[1]. We stress this point because it will have some relevance in the understanding of the torque measurement technique and the interpretation of experimental results in the following chapters.
Execution of the derivatives yields the oscillatory parts of the magnetization components (with higher order terms dropped) [20]:

$$M_\parallel^{\mathrm{osc}} = \text{const.} \times \frac{B^{1/2}}{\sqrt{A''}} \sum_{p=1}^{\infty} \frac{1}{p^{3/2}} \sin\left[2\pi p \frac{f}{B} + \phi_p\right] \tag{2.28}$$

$$M_{\perp,x}^{\mathrm{osc}} = -\frac{1}{f}\frac{\partial f}{\partial \theta_x} M_\parallel^{\mathrm{osc}} \tag{2.29}$$

$$M_{\perp,y}^{\mathrm{osc}} = -\frac{1}{f}\frac{\partial f}{\partial \theta_y} M_\parallel^{\mathrm{osc}}. \tag{2.30}$$

The above equations express the oscillation of the magnetization as a function of inverse field $1/B$. The frequency of the oscillation is f as defined by the Onsager relation Eq. 2.16 and higher harmonics thereof. We hence have derived the de Haas-van Alphen effect, i. e. the quantum oscillations of the magnetization, on theoretical grounds. Henceforth, we refer to f as

[1] For the derivatives w. r. t. the angles θ_i, the orientation of $\mathbf{B}$ is allowed to vary around $\hat{e}_z$. We choose θ_x and θ_y for the evaluation instead of conventional spherical coordinates $\theta_\mathbf{B}$, $\phi_\mathbf{B}$ because we evaluate the derivatives at the pole where $\phi_\mathbf{B}$ is ill-defined.

de Haas-van Alphen (dHvA) frequency.
At this point, it is worthwhile to comment on the consequences of deriving the dHvA effect using the grand-canonical potential Ω. In principle, Eqs. 2.28-2.30 strictly hold only for fixed chemical potential μ, which equivalently means that they imply oscillations of the particle number N as a function of $1/B$. Obviously, this does not express the concrete experimental situation in most cases. However, it turns out that the oscillations in particle number are small for three-dimensional systems, such as bulk solid state crystals, because the number of electrons that constructively participate in the dHvA oscillation is small compared to the entire electron number. Therefore, Eqs. 2.28-2.30 are generally a very good approximation for three-dimensional systems. In two-dimensional systems, the situation is however very different. For this reason, operations which are equivalent to reversing the Legendre transformation Eq. 2.19 need to be performed when calculating the dHvA effect for these systems.
The relations for the perpendicular components Eqs. 2.29 and 2.30 depend on the logarithmic derivatives $\frac{1}{f}\frac{\partial f}{\partial \theta_i}$ of the dHvA frequency f w. r. t. θ_i. These logarithmic derivatives represent the variation of the cross-sectional area of the Fermi surface for changes of the orientation of $\mathbf{B}$. For a completely symmetric Fermi surface, e. g. a sphere, these terms vanish and perpendicular components of the magnetization are consequently absent. Therefore, they are often referred to as anisotropy terms. For the torque measurement technique of dHvA oscillations, the anisotropy terms are of great importance (Sec. 3.1).

2.4 Lifshitz-Kosevich theory of finite temperature and inhomogeneity

So far we have only considered electrons at zero temperature and confined to infinitely sharp Landau levels. In the following, we present a formalism to include the effects of finite temperature and broadened Landau levels in the description of de Haas-van Alphen oscillations.
We start with the treatment of the temperature dependence. At zero temperature the Fermi-Dirac distribution is a step function and Landau tubes are fully occupied for energies $E_j(k_z) < \mu = E_\mathrm{F}$[1]. At finite temperature

[1] In the three-dimensional case the oscillations of μ are negligible and we can therefore set $\mu = E_\mathrm{F}$.

T, the Fermi-Dirac distribution $\mathcal{N}_{\mathrm{FD}}$

$$\mathcal{N}_{\mathrm{FD}}(\epsilon, \mu, T) = \frac{1}{1 + \exp\frac{\epsilon-\mu}{k_{\mathrm{B}}T}} \tag{2.31}$$

smears out the occupation over neighboring Landau levels in the proximity of μ. The consequence is a suppression of the dHvA amplitude by the temperature reduction factor

$$R_{\mathrm{T}} = \frac{X}{\sinh X}, \quad \text{with} \quad X = \frac{2\pi^2 k_{\mathrm{B}} m^\star T}{\hbar e B}. \tag{2.32}$$

In the above equation, we use the effective mass $m^\star$ instead of the band mass m_{b}. The band mass takes into account only the scattering of a Bloch electron in the crystal lattice. Compared to the band mass, the effective mass is renormalized by many-body interactions, e. g. electron-electron and phonon-electron interactions. An extensive treatment of many-body interactions is beyond the scope of this thesis. However, we do want to emphasize at this point that the effective mass $m^\star$, not the band mass m_{b}, appears in the temperature reduction factor when many-body effects are included in the description of the dHvA effect [20]. This is different from the reduction factor due to disorder, which we treat in the following.
In a real electron system such as a crystal, residual disorder leads to electron scattering. If a characteristic scattering time τ and an exponential decay of the occupation of a state by the scattering process with time constant τ is assumed, a Lorentzian broadening of the Landau levels

$$\mathcal{L}(\epsilon, E_n, \tau) = \frac{1}{\pi} \frac{\hbar/(2\tau)}{(\epsilon - E_n)^2 + (\hbar/(2\tau))^2} \tag{2.33}$$

is the consequence. The broadening of the Landau levels also causes a suppression of the dHvA amplitude by the Dingle reduction factor

$$R_{\mathrm{D}} = \exp\left(-\frac{\pi m_{\mathrm{b}}}{eB\tau}\right). \tag{2.34}$$

As mentioned above, the band mass m_{b}, not the effective mass $m^\star$, enters the Dingle reduction factor R_{D}, different from the temperature reduction factor R_{T}. This fact appears to be counterintuitive. An increased scatter-

ing on phonons, for example, would be expected to give rise to a reduction similar to Eq. 2.34 and hence the effective mass $m^\star$ should appear in this relation in some form. The reasons for its absence are complicated [24], but the effect is documented experimentally [25]. The reduction due to disorder Eq. 2.34 was first derived by Dingle [26] while the temperature reduction Eq. 2.32 has been first elaborated by Lifshitz and Kosevich in a comprehensive treatment of the de Haas-van Alphen effect [27, 28].
Often Eqs. 2.32 and 2.34 are merely stated although they can be derived relatively easily in an original manner [20]. The basic idea is that in a non-ideal sample, various inhomogeneities can be taken into account by assuming a smearing of the phase ϕ of the dHvA frequency with a characteristic phase distribution function $D(\phi)$. The superposition of dHvA oscillations $\propto \sin(f/B + \phi)$ of varying phase ϕ weighted by the distribution function $D(\phi)$ amounts to a reduction factor proportional to the Fourier transform of the distribution function $D(\phi)$. The effect of finite temperature T can be considered as an example of phase smearing if a real electron system at temperature T with chemical potential μ is thought of as an ensemble of electron systems at $T = 0$ with a distribution of Fermi energies χ around μ such that at a given energy ϵ a fraction $\mathcal{N}_{\mathrm{FD}}(\epsilon, \mu, T)$ of hypothetical electron systems has $\chi > \epsilon$. In other words, a fraction $\mathcal{N}_{\mathrm{FD}}(\epsilon, \mu, T)$ of the hypothetical electron systems has the state with energy ϵ occupied. It is easily shown that the required distribution of Fermi energies is $-\partial\mathcal{N}_{\mathrm{FD}}/\partial\epsilon|_{\epsilon=\chi}$. The deviation $\chi - \mu$ of the Fermi energy of a hypothetical electron system from the average Fermi energy μ is equivalent to a phase shift of the dHvA frequency of the respective electron system. We omit the required mathematics, but state that the temperature reduction factor $R_{\mathrm{T}} = X/\sinh X$ thus arises as the Fourier transform of the negative derivative of the Fermi-Dirac distribution. Similarly, a Lorentzian broadened Landau level can be treated as an ensemble of electron systems at $T = 0$ with a distribution of Fermi energies χ around μ, where the distribution is proportional to $1/\left((\chi - \mu)^2 + (\hbar/2\tau)^2\right)$. Here, the analytical form of the Dingle reduction factor Eq. 2.34 as an exponentially decaying function is fairly obvious since this is the well known Fourier transform of a Lorentzian.
In the limit $\hbar\frac{eB}{m^\star} \lesssim 2\pi^2 k_{\mathrm{B}} T$, i. e. for low fields or high temperatures, re-

spectively, the temperature reduction factor becomes

$$R_{\mathrm{T}} \approx \frac{4\pi^2 k_{\mathrm{B}} T}{\omega_{\mathrm{c}} \hbar} \exp\left(-\frac{2\pi^2 k_{\mathrm{B}} T}{\omega_{\mathrm{c}} \hbar}\right). \tag{2.35}$$

In this form, it is similar to the Dingle reduction factor. In other words, the effect of a finite scattering time τ is similar to the temperature reduction for sufficiently high temperatures. For this reason, often a temperature equivalent to the scattering time τ is specified, which indicates sample purity. This so-called Dingle temperature is defined by

$$T_{\mathrm{D}} = \frac{\hbar}{2\pi k_{\mathrm{B}} \tau}. \tag{2.36}$$

To arrive at the expressions for the magnetization at finite temperature and with a finite scattering time τ, Eqs. 2.28-2.30 can simply be multiplied by the two reduction factors:

$$M_{\parallel}^{\mathrm{osc}}(T,\tau) = M_{\parallel}^{\mathrm{osc}} R_{\mathrm{T}} R_{\mathrm{D}}, \tag{2.37}$$

$$M_{\perp,x}^{\mathrm{osc}}(T,\tau) = M_{\perp,x}^{\mathrm{osc}} R_{\mathrm{T}} R_{\mathrm{D}}, \tag{2.38}$$

$$M_{\perp,y}^{\mathrm{osc}}(T,\tau) = M_{\perp,y}^{\mathrm{osc}} R_{\mathrm{T}} R_{\mathrm{D}}. \tag{2.39}$$

These equations are referred to as Lifshitz-Kosevich relations. They are of great experimental importance because they allow the extraction of the effective mass $m^\star$ of a dHvA orbit by studying the temperature dependence of the magnetization oscillations and the extraction of the quotient of band mass and scattering time m_{b}/τ by examination of the field dependence of the magnetization oscillations.

2.5 Topology of Fermi surfaces

In the previous sections, we have mostly used the concept of the Fermi sphere of free electrons in order to explain the origin of the dHvA effect. The enormous experimental importance and power of the dHvA effect are rooted in the ability to reconstruct arbitrarily shaped Fermi surfaces by mapping out their extremal cross-sectional areas. The specific shape of the Fermi surface of a crystal depends on its band structure, i. e. the $\mathbf{k}$-dependent dispersion of the electrons. A presentation of methods for the

calculation of crystal band structures is beyond the scope of this thesis. Here, we only introduce a nomenclature for Fermi surfaces that arise from energy bands with strongly differing dispersion in different K-space directions.

The isotropic shape of the Fermi sphere of free electrons reflects the completely isotropic dispersion. The dispersion of a real electron system in a crystal given by its band structure is in general not isotropic. Scattering on the crystal lattice and many-body interaction with phonons and other electrons will alter the dispersion depending on K-space orientation and energy. For the nomenclature of different Fermi surface topologies, we refer to Fig. 2.3. Figure 2.3 (a) shows an ellipsoidal Fermi surface. This Fermi surface reflects a dispersion that is similar to the one of free electrons. An ellipsoid as in Fig. 2.3 (a) arises as Fermi surface instead of the spherical surface when the dispersion in the different K-space directions differs slightly, which is expressed by different band masses m_{b}. If, in contrast, the dispersion of the electrons drastically differs for one K-space direction k_z compared to the other two perpendicular directions, i. e. their energy is (quasi) independent from k_z, the resulting Fermi surface will have a cylindrical shape. This is depicted in Figs. 2.3 (b,c). In the ideal case of zero dispersion in one direction, the Landau surface is a cylinder as depicted in Fig. 2.3 (b). Because of the lack of dispersion in one direction, this is referred to as two-dimensional Fermi surface. A real system will however feature at least a small dispersion in k_z-direction. The corresponding Fermi surface would then resemble a warped cylinder as illustrated in Fig. 2.3 (c). This is called a quasi-two-dimensional Fermi surface. Similarly, in the complete absence of dispersion in two directions, the Fermi surface is a plane. In a real system the plane features some corrugations. These Fermi surfaces are shown in Figs. 2.3 (d,e) and referred to as one-dimensional and quasi-one-dimensional Fermi surface, respectively.

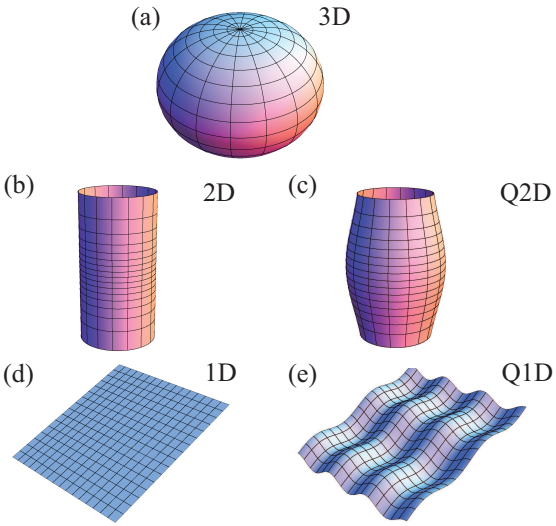

Figure 2.3: Nomenclature of Fermi surfaces from bands with different anisotropic dispersions. (a) Ellipsoidal Fermi surface that arises from bands for which the dispersion in different K-space directions differs only slightly. (b) Idealized case of a Fermi surface, which arises from a band with zero dispersion in one direction. The Fermi surface is a cylinder. This is referred to as two-dimensional Fermi surface. (c) Quasi-two-dimensional Fermi surface from a band with little dispersion in one direction compared to the other two directions. (d) One-dimensional Fermi surface, which arises from a band with zero dispersion in two directions. (e) Quasi-one-dimensional Fermi surface from a band with little dispersion in two directions compared to the third direction.

3 Torque measurements using micromechanical cantilevers

For the measurement of the de Haas-van Alphen effect several measurement methods exist. The traditional technique, which was also employed by de Haas and van Alphen in the original discovery of the effect in bismuth [17], makes use of the force acting on a magnetic moment in an inhomogeneous magnetic field. However, there is a serious intrinsic disadvantage of this method: Because of the inhomogeneity of the field, the energy of a Landau level n is not constant in space or, equivalently, the position of the Fermi energy E_{F} relative to the Landau level depends on the spatial position. In the language of Sec. 2.4, this constitutes a phase smearing of the dHvA frequencies, inherent to the measurement technique. For this reason, the power of the original method is rather limited.
Nowadays, there are essentially three established and widely used methods: (1) The torque technique exploits the torque $\Gamma = \mathbf{M} \times \mathbf{B}$ acting on a sample with magnetization $\mathbf{M}$ in a magnetic field $\mathbf{B}$. This method was used for the experiments presented in this thesis. (2) In the modulation technique [29–33], a small oscillating field is superimposed onto the field B, which causes the sample magnetization M also to oscillate around the value $M(B)$. The sample is placed in the proximity of a pick-up coil, where the oscillating magnetization induces an electro-magnetic field. Hereby, the physical quantity derived from the measurement signal is not the magnetization itself, but its first and higher-order derivatives $\mathrm{d}^k M/\mathrm{d}B^k$ with respect to B. (3) Similarly to the modulation technique, pulsed field experiments in high field laboratories utilize the electromagnetic field induced in a pick-up coil by the rapid variation of the magnetization in the pulsed field [34]. All techniques have their specific advantages. The modulation technique allows for a phase sensitive detection, the pulsed field experiments can reach field regimes which are not accessible by static fields while the torque technique is easily integrated in experimental conditions with limited space. The static torque technique also leaves the electron system in its thermodynamic ground state, which is particu-

larly important for experiments with two-dimension electron systems [35]. In this chapter, we present the torque measurement technique used for the experiments of this thesis. The technique employs micromechanical cantilever magnetometers (MCMs) with a capacitive readout scheme. The chapter is organized as follows: In Sec. 3.1, the basic working principle of the measurement technique and of the readout is explained. Section 3.2 describes the specific MCMs which we employ and their fabrication. Sections 3.3 and 3.4 treat the coupling of different torque components to the measurement signal and the calibration of the MCMs. In Sec. 3.5, we briefly sketch the experimental setup it its entirety and specify the sensitivity achieved in the magnetization experiments.

3.1 Cantilever torque magnetometry

The torque measurement principle of a micromechanical cantilever magnetometer (MCM) is straightforward: The sample is mounted on the free end of a flexible, singly clamped beam. In the presence of a magnetic field $\mathbf{B}$, a torque Γ acts on the sample if it has a non-vanishing magnetization component perpendicular to $\mathbf{B}$:

$$\Gamma = \mathbf{M} \times \mathbf{B}. \tag{3.1}$$

The torque will deflect and/or twist the beam. The resulting deflection and/or torsion can be read out by some means and thus provide a measure for the magnetization of the sample. The measurement principle requires a non-parallel component of the magnetization with respect to $\mathbf{B}$, i. e. an anisotropic magnetization $\mathbf{M} \nparallel \mathbf{B}$. The parallel magnetization component $M_{\parallel}$ cannot be detected. As discussed in Sec. 2.3, the oscillatory magnetization due to the dHvA effect can exhibit components $M^{\mathrm{osc}}_{\perp,x}$, $M^{\mathrm{osc}}_{\perp,y}$ perpendicular to $\mathbf{B}$ if the Fermi surface is anisotropic. Hence, dHvA oscillations can be detected by the torque technique as long as the corresponding Fermi surface sheet is not completely isotropic. For symmetry reasons, dHvA frequencies are generally stationary around high-symmetry directions of a crystal and the anisotropy term consequently vanishes in these directions. The torque method for mapping out a Fermi surface thus has intrinsic blind spots for the magnetic field along these directions. This is, however, not a severe limitation since usually the torque is detectable at a small angular deviation (of a few degrees or less) from the high-symmetry direction.

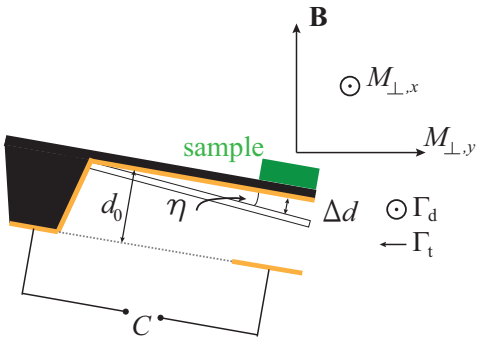

Figure 3.1: Measurement principle of cantilever torque magnetometry. A sample is mounted on the free end of a clamped cantilever beam. In the presence of a magnetic field $\mathbf{B}$, a torque $\Gamma = \mathbf{M} \times \mathbf{B}$ acts on the sample with magnetization $\mathbf{M}$. The torque has two components Γ_d and Γ_t associated with the magnetization components perpendicular to $\mathbf{B}$, $M_{\perp,y}$ and $M_{\perp,x}$, respectively. The bending torque component Γ_d deflects the cantilever from its equilibrium position by an angle η. This corresponds to a linear deflection Δd of the cantilever, changing its equilibrium distance d_0 to the substrate. The torsional torque component Γ_t twists the cantilever by an angle τ (not shown). Readout of the cantilever deflection can be achieved with capacitive means by monitoring the capacitance C, which is formed by the (metallized) cantilever and a suitable counter electrode on the substrate.

For a more detailed analysis of the coupling of the magnetization components to the MCM, we refer to Fig. 3.1, where a cantilever beam, onto which a sample is attached, is depicted. The magnetic field $\mathbf{B}$ effects two perpendicular magnetization components $M_{\perp,x}$, $M_{\perp,y}$, where the former points out of the plane of projection and the latter is oriented approximately along the cantilever's beam. The magnetization component $M_{\perp,y}$ will exert a bending torque component Γ_d on the cantilever whereas magnetization component $M_{\perp,x}$ causes a torsional torque component Γ_t. The bending component Γ_d deflects the cantilever beam from its equilibrium position by an angle η. By contrast, the torsional component Γ_t twists the cantilever beam along its axis by an angle τ (not shown). Several methods exist for the detection of the cantilever deflection. Most widely used are techniques which rely on an optical readout, e. g. employing a laser interferometer [36], a piezoresistive readout [37, 38], and a capacitive read-

out [39]. For the experiments of this thesis, we used the capacitive method. For this technique, the cantilever is either conductive itself or possesses a conductive layer on its bottom side (Fig. 3.1). The cantilever forms a capacitor of capacitance C_0 together with a suitable counter electrode on a substrate, on which the cantilever is mounted. The bending component Γ_d causes a deviation Δd from the cantilevers equilibrium distance d_0 from the substrate. This effects a change of capacitance ΔC_d which can be detected. In principle, also the torsional component Γ_t will influence the capacitance C. We will however show that the effect of the torsional component is negligible for the experiments presented in this thesis.

3.2 Copper beryllium cantilevers

The cantilevers used for the experiments presented in this thesis are made from the alloy copper beryllium (CuBe). They were produced from a CuBe foil of $50\,\mu\mathrm{m}$ thickness.
For the preparation, the cantilever contours were defined by means of optical lithography on one side of the CuBe foil while a protective photoresist layer was applied onto the other side. The foil was then immersed into a $FeCl_3$ etching solution in order to etch the defined cantilever structure from the CuBe foil. Subsequently, the photoresist was removed by rinsing the cantilever with acetone.
The cantilever is shown in Fig. 3.2 in a schematic view. It consists of a $4 \times 5\,\mathrm{mm}^2$ paddle to carry the sample and two beams of $160\,\mu\mathrm{m}$ width each. The cantilever is mounted onto a printed circuit board using one, two, or three $50\,\mu\mathrm{m}$ thick spacer parts, which were also produced from the CuBe foil. The circuit board contains an electrode, which forms a capacitor together with the cantilever's paddle for detection. In Fig. 3.3 the dimensions of the cantilever are specified. These parameters will be relevant for the following section.

3.3 Coupling of torque components to capacitive readout

In the following, we discuss the capacitive readout for torque magnetometry quantitatively and derive equations for the relation of the capacitance change effected by the bending and the torsional torque component, respectively. We argue that the torsional component is completely sup-

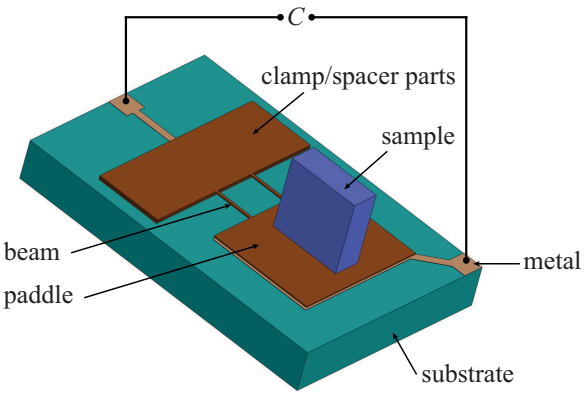

Figure 3.2: Schematic view of the CuBe cantilevers employed for this thesis. The cantilever consists of a $4 \times 5\,\mathrm{mm}^2$ paddle and two beams of $160\,\mu\mathrm{m}$ width. It is fabricated from a $50\,\mu\mathrm{m}$ thick CuBe foil. The sample is placed onto the central part of the paddle. The cantilever is attached to a substrate using spacer parts to adjust the height of the cantilever over the substrate. The substrate comprises a contact for the cantilever and a suitable counter electrode such that the cantilever's paddle and the counter electrode form a capacitor. Its capacitance can be detected in order to acquire a measure for the deflection of the cantilever and hence the magnetization of the sample.

pressed by the specific cantilever design used. This fact will be relevant for the interpretation of the experiments presented in Chs. 7 and 8.
We start with the quantitative treatment of the bending torque component Γ_d. Following Hooke's law, the deflection angle η (cf. Fig. 3.1) is proportional to Γ_d for sufficiently small deflections, where we define the spring constant k_d by

$$\Gamma_\mathrm{d} = k_\mathrm{d}\eta. \tag{3.2}$$

The spring constant k_d can be determined by applying Euler-Bernoulli beam theory. For a cantilever with rectangular paddle and beam and a torque distributed over the paddle, the corresponding equations and boundary conditions have been solved in Ref. [40]. Here, we only state the result for the spring constant in terms of geometric dimensions and material con-

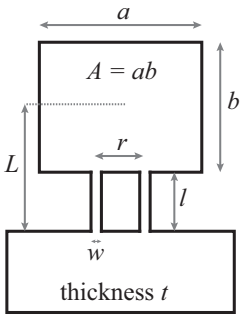

Figure 3.3: Specification of the geometrical dimensions of the CuBe cantilever: paddle width $a = 5.0\,\mathrm{mm}$, paddle length $b = 4.0\,\mathrm{mm}$, distance from clamp to paddle center $L = 3.5\,\mathrm{mm}$, beam length $l = 1.5\,\mathrm{mm}$, beam distance $r = 1.5\,\mathrm{mm}$, beam width $w = 160\,\mu\mathrm{m}$. The thickness of the cantilever is $t = 50\,\mu\mathrm{m}$. The area of the paddle is denoted by $A = ab$.

stants[1]:

$$\Gamma_\mathrm{d} = k_\mathrm{d}\eta = \underbrace{\frac{2YI_\mathrm{s}L}{\left(L+\frac{b}{2}\right)\left(L-\frac{b}{2}\right)}}_{k_\mathrm{d}} \cdot \eta, \tag{3.3}$$

where L and b are as defined by Fig. 3.3, Y is the Young's modulus of the cantilever's material, i. e. CuBe, and I_s is the second areal moment of inertia for a deflection of the cantilever in the discussed direction. For a beam of constant rectangular cross section with width W and thickness T, it is given by $I_\mathrm{s} = \frac{1}{12}WT^3$. For the bending degree of freedom, we can treat the two beams in Fig. 3.3 of width w and thickness t as one beam of width $2w$ and thickness t. Hence the areal moment of inertia I_s is given by

$$I_\mathrm{s} = \frac{1}{6}wt^3. \tag{3.4}$$

[1] We omit some terms given in Ref. [40], which can be neglected in the approximation of a thin beam width compared to the paddle width.

In the small-angle approximation, the linear deflection of the cantilever Δd at the position of the paddle center is proportional to η:

$$\Delta d = L\eta. \tag{3.5}$$

We now turn to the capacitance change effected by the deflection. The capacitance C formed by the paddle and the counter electrode can be expanded in a power series in $\Delta d/d_0$, where d_0 is the equilibrium distance between cantilever and substrate:

$$C(d_0 + \Delta d) = \frac{\epsilon_0 A}{d_0 + \Delta d} = C_0 \left(1 - \frac{\Delta d}{d_0} + \mathcal{O}\left(\frac{\Delta d^2}{d_0^2}\right)\right), \tag{3.6}$$

where ϵ_0 is the vacuum permittivity and $A = ab$ the area size of the paddle. From the power series, we read off the capacitance change ΔC_d from the bending torque Γ_d in leading order:

$$\Delta C_\mathrm{d} = C_0 \frac{\Delta d}{d_0} = C_0 \frac{L}{d_0}\eta = \frac{C_0 L}{d_0 k_\mathrm{d}}\Gamma_\mathrm{d}, \tag{3.7}$$

where we have used Eqs. 3.5 and 3.2 to replace Δd and η, respectively. The torque Γ_d couples in first order to the capacitance.

We now proceed with the discussion of the effect of the torsional torque Γ_t component on the capacitance signal, where we again refer to Fig. 3.3 for the geometrical definitions. The torsional movement of the double beam cantilever is more complicated: It involves both a twisting and a bending of the two beams at the same time because a torsion as indicated in Fig. 3.1 will lift one beam upwards and press the other one downwards while twisting both of them. Here, we are only interested in an estimate of the scale of the torsional capacitance change relative to the change effected by the bending. For this, the following model should be sufficient. We assume a torsional angular deflection τ and approximate the two contributions to the resulting torque from twisting and up- and down-bending of the two beams separately. Hereby, we ignore the paddle, i. e. we assume that the paddle is completely stiff and that the torque acts directly on the beams. We consider Fig. 3.4, where the two cantilever beams are sketched in a cross-sectional view both in their equilibrium position and at a finite torsional angle τ. At the position of the beams, the linear deflection v_l is given by

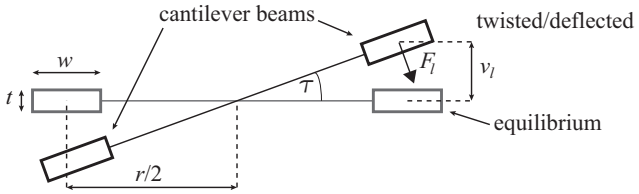

Figure 3.4: Torsional degree of freedom of the cantilever. A component Γ_t of the torque twists the cantilever around its central axis by an angle τ. This causes a simultaneous up- and down-bending of the two beams as well as a torsion of both beams. The coupling of this motion to the capacitance signal can be neglected. For details, the reader is referred to the text.

$$v_l = \tau \frac{r}{2}. \tag{3.8}$$

With Euler Bernoulli beam theory, the deflection v_l at the end of the beam can be related to a force F_l acting at the same position:

$$F_l = \frac{3YI_\mathrm{b}}{l^3} v_l, \tag{3.9}$$

where the areal moment of inertia is $I_\mathrm{b} = \frac{1}{12} wt^3$. For a rotation around the central axis of the configuration, the lever is $r/2$. Hence the first contribution $\Gamma_{\mathrm{t},1}$ to the torsional torque, arising from the up- and down-bending, is

$$\Gamma_{\mathrm{t},1} = 2 \cdot \frac{r}{2} \cdot \underbrace{\tau \frac{r}{2} \frac{3YI_\mathrm{b}}{l^3}}_{F_l}, \tag{3.10}$$

where the leading factor of two takes the second beam into account and where we have used Eq. 3.8. The contribution $\Gamma_{\mathrm{t},2}$ from the twisting of the beams is readily calculated from the textbook formula for beam torsions [41]

$$\Gamma_{\mathrm{t},2} = 2 \cdot \frac{GI_\mathrm{t}}{l} \tau. \tag{3.11}$$

Here, G stands for the shear modulus, I_t for the torsion constant, and the leading factor of two again accounts for the second beam. The torsion constant is $I_\mathrm{t} = \beta_t wt^3$, where β_t depends on the ratio of w and t. For the values as in Fig. 3.3 one finds $\beta_\mathrm{t} \approx 0.26$ [42].

Collecting $\Gamma_{\mathrm{t},1}$ and $\Gamma_{\mathrm{t},2}$, we obtain the spring constant k_{t} for the torsional degree of freedom of the cantilever:

$$\Gamma_{\mathrm{t}} = k_{\mathrm{t}}\tau = \underbrace{\left(\frac{2GI_{\mathrm{t}}}{l} + \frac{3YI_{\mathrm{b}}r^2}{2l^3}\right)}_{k_{\mathrm{t}}} \cdot \tau. \tag{3.12}$$

It now remains to relate the deflection τ caused by Γ_{t} to a capacitance change. The capacitance C of the capacitor formed by the substrate electrode and with the paddle tilted around its central axis by angle τ is easily retrieved by integration:

$$C(\tau) = \frac{\epsilon_0 b}{\tau} \ln\left(\frac{1 + \frac{a}{2d_0}\tau}{1 - \frac{a}{2d_0}\tau}\right). \tag{3.13}$$

We apply the expansion $\ln\left(\frac{1+\epsilon}{1-\epsilon}\right) = 2\epsilon + \frac{2}{3}\epsilon^3 + \mathcal{O}(\epsilon^5)$ to arrive at the power series of the capacitance in τ

$$C(\tau) = C_0 + \frac{C_0 a^2}{12 d_0^2}\tau^2 + \ldots \tag{3.14}$$

The leading order correction to C_0

$$\Delta C_{\mathrm{t}} = C_0 \frac{a^2}{12 d_0^2}\tau^2 = C_0 \frac{a^2}{12 d_0^2}\left(\frac{\Gamma_{\mathrm{t}}}{k_{\mathrm{t}}}\right)^2 \tag{3.15}$$

is quadratic in τ. This is intuitive as the tilting does not change the distance between the paddle and the substrate on average.
We are now able to compare the coupling of the torsional torque component and the bending torque component to the measurement signal, i. e. the capacitance, with each other. For this we evaluate the ratio of ΔC_{t} from Eq. 3.15 and ΔC_{d} from Eq. 3.7

$$\frac{\Delta C_{\mathrm{t}}}{\Delta C_{\mathrm{d}}} = \frac{a^2}{12 d_0 L} \cdot \frac{\tau^2}{\eta} = \frac{a^2}{12 d_0 L} \cdot \frac{k_{\mathrm{d}} \Gamma_{\mathrm{t}}^2}{k_{\mathrm{t}}^2 \Gamma_{\mathrm{d}}}. \tag{3.16}$$

For comparative purposes, we assume equal torsional and bending torque components $\Gamma \equiv \Gamma_{\mathrm{t}} \equiv \Gamma_{\mathrm{d}}$ and use the geometric and material parameters

(Y = 130 GPa, G = 50 GPa, [43]) to arrive at

$$\frac{\Delta C_\mathrm{t}}{\Delta C_\mathrm{d}} = 0.007 \cdot \frac{\Gamma}{10^{-6}\,\mathrm{Nm}}. \tag{3.17}$$

The resulting ratio depends linearly on the considered torque scale Γ. This is caused by the different order of coupling of bending and torsional torque to the measurement signal. Typical scales of the oscillatory torque components of dHvA oscillations discussed in the following chapters are $1{\cdot}10^{-11}$ Nm$-1{\cdot}10^{-7}$ Nm and in some exceptional cases $1{\cdot}10^{-6}$ Nm. Hence, the coupling of the magnetization component $M_{\perp,x}$ effecting the torsional torque Γ_t to the measurement signal is usually less than 0.1% relative to the component $M_{\perp,y}$. Thus, it can be neglected. This insight will be important for the interpretation of the experimental results in Chs. 7-8.

3.4 Calibration

We now turn to the discussion of the calibration scheme used for the cantilevers described in Sec. 3.2. As discussed in the previous section, the degree of freedom associated with a torsional motion of the cantilever around its central axis can be neglected in the experiments. Therefore, we drop the indices that distinguish between the torsional and the bending torque component and the two perpendicular magnetization components, respectively, in the following.
In principle, Eq. 3.7 along with the explicit expression of k_d in Eq. 3.3 provides the required relation of the torque Γ acting on the sample to the measurement quantity ΔC. By Eq. 3.1 the perpendicular magnetization $M_\perp$ can be deduced. However, the measurement principle allows for a convenient in-situ calibration of the cantilever to derive the experimental calibration constant K defined by

$$\Gamma = K\,\Delta C. \tag{3.18}$$

For the calibration, a dc voltage U is applied between the cantilever paddle and the counter electrode on the substrate. This causes an attractive electrostatic force F acting on the paddle, given by

$$F = \frac{1}{2}\frac{C_0 U^2}{d_0}. \tag{3.19}$$

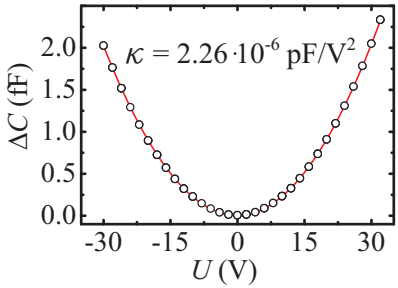

Figure 3.5: Calibration curve of a CuBe cantilever. A dc voltage U is applied between the cantilever paddle and the counter electrode. This deflects the cantilever and effects a change in capacitance ΔC. The open circles represent measured data for the capacitance change ΔC versus applied voltage U. A quadratic fit routine is used (red line) to obtain the parameter κ defined by $\Delta C = \kappa U^2$, which is a measure for the sensitivity of the magnetometer.

The force acting on the paddle is equivalent to a torque given by

$$\Gamma = \beta F L = \frac{\beta C_0 L U^2}{2 d_0}, \tag{3.20}$$

where L is the lever, i. e. the distance from the paddle center to the clamp of the cantilever. The factor β accounts for the reduced mechanical response of a cantilever, which is subject to a force at the end of the beam, compared to a cantilever deflected by a torque acting at the same position. This has been discussed in detail [40]. It is a function of the geometrical dimensions of paddle and beam. Here we only give the value for the specific double-beam cantilever of Sec. 3.2, which is $\beta = 0.98$.
Combining Eqs. 3.18 and 3.20, a quadratic dependence of ΔC on U is obtained

$$\Delta C = \kappa U^2, \quad \text{with} \quad \kappa = \frac{\beta C_0 L}{2 d_0 K}. \tag{3.21}$$

The constant κ can readily be determined by a quadratic fit to capacitance data as a function of applied voltage U. Figure 3.5 shows an exemplary calibration curve for a CuBe cantilever. The experimental calibration con-

stant K is then inversely related to the constant from the quadratic fit

$$K = \frac{\beta C_0^2 L}{2\epsilon_0 A \kappa}, \tag{3.22}$$

where we used $C_0 = \epsilon_0 A/d_0$ to replace d_0 by the paddle area A and the equilibrium capacity C_0 since A and C_0 are easier to determine than d_0. At this point, it is worthwhile to consider the dependence of K on the equilibrium capacitance C_0. By Eq. 3.18 we have

$$K = \frac{\Gamma}{\Delta C}. \tag{3.23}$$

Using Eq. 3.7 we can replace ΔC by $\Delta C = C_0 \frac{\Delta d}{d_0}$:

$$K = \frac{\Gamma}{\Delta d} \cdot \frac{d_0}{C_0}. \tag{3.24}$$

Since the deflection $\Delta d \propto \Gamma$ caused by the torque is independent of the capacitance and $d_0 \propto 1/C_0$, we have

$$K \propto \frac{1}{C_0^2}. \tag{3.25}$$

This means that K for the same cantilever mounted at different distances to the substrate d_0 has an inverse quadratic dependence on C_0 or equivalently a quadratic dependence on d_0. For experiments with samples for which the total capacitance signal varies over a considerable range depending on field strength B due to a large non-oscillatory magnetization signal, this scaling dependence of K is important to obtain a correct field-dependent calibration constant.

3.5 Experimental setup and sensitivity

Observation of the de Haas-van Alphen effect requires low temperatures and high magnetic fields. The experiments presented in the following chapters were performed in two superconducting solenoids from *Cryogenic Limited*, each of which is integrated into a liquid Helium cryostat. They are capable of providing maximum fields of 14 T and 15 T at the

field center. The 15 T-magnet was set up in the framework of this thesis. It additionally features two removable insert coils, which can provide either a gradient field of 5 T/m or or an ac field, whose amplitude depends on the modulation frequency. The insert coils were not used for the experiments in this thesis. The specified field homogeneity of the main solenoids are 10^{-4} and $5 \cdot 10^{-5}$ in a $1\,\mathrm{cm}^3$ spherical volume around the field center for the 14 T-magnet and the 15 T-magnet, respectively. The homogeneity guarantees that the effect of possible forces on the cantilever arising from a non-vanishing field gradient via $\nabla(\mathbf{M} \cdot \mathbf{B})$ is negligible compared to the effect of the torque signal. Their relative scale is $1/B \cdot \partial B/\partial x \cdot L$, where L is the length of the lever. For the specified homogeneity and $L = 3.5\,\mathrm{mm}$, this parameter is $3 \cdot 10^{-5}$ and hence force contributions are irrelevant.
Low temperatures were achieved by mounting the cantilever on its substrate on the sample head of a ^{3}He system. For operation, the parasitic ^{3}He system is immersed into the liquid helium bath of the combined magnet-cryostat such that the position of the cantilever at the sample head coincides with the field center. The high field homogeneity around the field center specified above allows a manual positioning of the ^{3}He system relative to the field axis since an accuracy on the millimeter scale is sufficient. In the liquid helium bath, the ^{3}He system can provide temperatures down to $T = 280\,\mathrm{mK}$. In detail, two systems from *Oxford Instruments plc* (Heliox VL) and *ICE Oxford Ltd* ($^3\mathrm{ICE}^{\mathrm{DIPPER}}$) were employed. The former is able to achieve a reliable temperature control from $0.3\,\mathrm{K}$ to $\sim 50\,\mathrm{K}$ while the latter has a rotary sample stage which allows for angle-dependent measurements.
Both ^{3}He systems were equipped with coaxial cables for the capacitive readout of the cantilever torque signal described in Sec. 3.3. The coaxial wiring guarantees shielding from stray capacitances and fields, which would severely deteriorate the capacitance signal. For the readout highly sensitive capacitance bridges from *Andeen Hagerling* (model 2500A and 2700A) were used. Figure 3.6 depicts a photographical in-situ image of a CuBe cantilever. It is mounted with a clamp to the substrate. The area on the substrate surrounding the cantilever is also metallized in order to provide a defined electrical ground for the three-terminal capacitance measurements with the *Andeen Hagerling* bridge. In the picture, parts of the coaxial wiring as well as a gear of the rotational stage of the $^3\mathrm{ICE}^{\mathrm{DIPPER}}$ (out of focus) can be seen. The cantilever carries the MnB_2 sample, experimental data of which are discussed in Ch. 8. For measurements with a

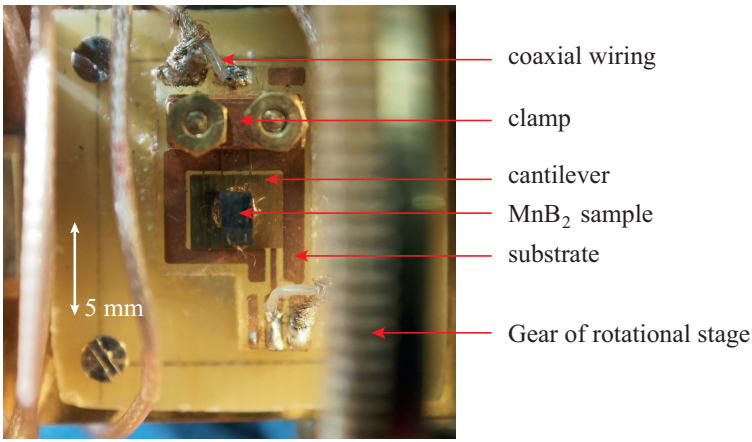

Figure 3.6: Photographical in-situ image of a CuBe cantilever carrying the MnB_2 sample of Ch. 8. The cantilever is mounted to a substrate using spacer parts and screws. The area on the substrate surrounding the cantilever is metallized such that an electric ground can be defined in the proximity of the cantilever for the three-terminal capacitance measurement. Parts of the coaxial wiring for the capacitive readout are visible. Also, a gear of the rotational stage of the ^{3}ICE$^{\text{DIPPER}}$ can be seen (out of focus).

small variation of the overall capacitance C and typical averaging times of the capacitance bridge set to $\sim 1\,\text{s}$, the rms noise of the bridge was $\delta C \approx 2\,\text{aF}$. This allows to estimate the sensitivity with which the magnetization M can be measured via $\Delta M = \delta\Gamma/B = K\delta C/B$. The magnetization resolution δM hence depends on the calibration constant K and the field B at which it is detected. In Table 3.1 we list the values for K and the maximal resolution δM_{max} for the different experimental series of the following chapters. Hereby, the maximal sensitivity δM_{max} is given at the highest accessible field strength $B = 15\,\text{T}$. The values given for K differ due to fabrication variances[1] and different mounting distances d_0 from the substrate. We also note that the values given in Table 3.1 relate to the specific cantilevers that were used for the majority of the respective series. Due to infrastructural reasons, parts of some series were performed

[1] For example, the width of the cantilever beams can vary as a result of varying etching durations etc.

Experimental series	K (Nm/pF)	$\delta M_{\max}$ (J/T) at B = 15 T
VB_2 ([100]-[120])	$0.998 \cdot 10^{-5}$	$\sim 1.5 \cdot 10^{-12}$
VB_2 ([001]-[100])	$2.82 \cdot 10^{-5}$	$\sim 3.8 \cdot 10^{-12}$
VB_2 ([001]-[120])	$0.405 \cdot 10^{-5}$	$\sim 0.5 \cdot 10^{-12}$
MnB_2 ([100]-[120])	$2.09 \cdot 10^{-5}$	$\sim 2.8 \cdot 10^{-12}$

Table 3.1: List of experimentally determined calibration constants K and corresponding maximal sensitivities $\delta M_{\max}$ for a rms capacitance noise of $\delta C \approx 2$ aF at magnetic field B = 15 T. The majority of the experimental series indicated in the first column has been performed using a cantilever with the respective parameters. The Miller indices in the first column relate to the plane in which the orientation of the magnetic field $\mathbf{B}$ was varied in the respective series. See Chs. 7-8

or repeated in subsequent cool-down cycles with different cantilevers. For measurements with a strongly varying overall capacitance signal, the capacitance signal has a considerable variation even within the averaging time ~ 1 s of the bridge. Therefore, the effective resolution δM is reduced compared to the maximal resolution $\delta M_{\max}$ in this case. Furthermore, it was found that the capacitance bridge performs a re-balancing after every change of the overall signal by 2.5 fF. The re-balancing causes jumps in the capacitance signal of a field sweep as a function of B on the order of 5-10 aF. These jumps also result in an effective reduction of the ideally attainable resolution.

4 Torque magnetometry experiments on graphene

In this chapter we present torque magnetometry measurements on the two-dimensional carbon allotrope graphene. Graphene, a truly two-dimensional crystal, is briefly introduced in Sec. 4.1. This is followed by numerical calculations of the de Haas-van Alphen effect for two-dimensional electron gases with a linear dispersion relation as in graphene in Sec. 4.2. We then turn to a listing of the separate experiments and of the specific graphene samples which have been investigated in Sec. 4.3. The chapter is concluded by a discussion of the experimental outcome in Sec. 4.4.

4.1 Graphene - a truly two-dimensional crystal

Graphene is a two-dimensional crystalline allotrope of carbon. It consists of a monolayer of sp^2-hybridized carbon atoms in a honeycomb lattice (Fig. 4.1 (a)) and can be regarded as the base structural material for building other carbon allotropes: An appropriately cut graphene sheet can be wrapped to a zero-dimensional C_{60} fullerene. Graphene sheets can also be rolled up to form one-dimensional carbon nanotubes or stacked to form three-dimensional graphite. Graphene has theoretically been studied for decades [44–46], but was assumed not to exist as a stand-alone crystal. The free state was predicted to be thermodynamically unstable towards decomposition and formation of wrapped or rolled structures such as fullerenes and nanotubes [47]. This assumption was falsified in 2004 when Novoselov et al. isolated monolayers from graphite with a technique of striking simplicity and straightforwardness [4]: They mechanically exfoliated graphene from pyrolytic graphite by repeated peeling using a commercial adhesive tape and subsequently deposited the isolated graphene flakes on silicon oxide substrates. This ignited tremendous research efforts both in academia and industry and graphene became one of the most active fields of research in science in the last decade [7, 48–52]. This enthusiasm is justified by unique properties of graphene, such as ex-

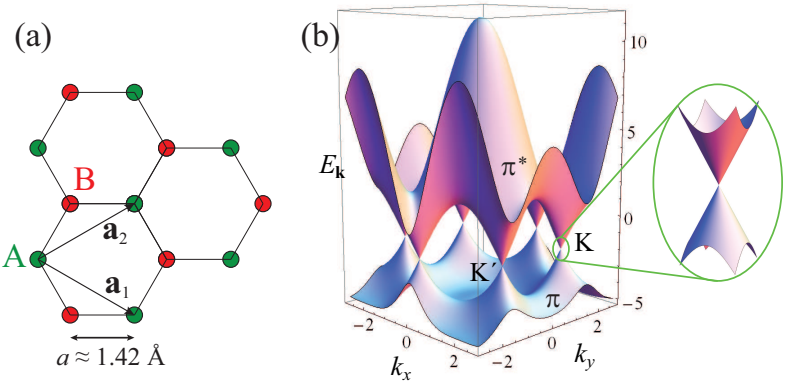

Figure 4.1: (a) Graphene lattice structure. The graphene honeycomb lattice consists of two equivalent sublattices A and B. The hexagonal lattice with a basis of two atoms per unit cell is spanned by unit vectors $\mathbf{a}_1$ and $\mathbf{a}_2$. (b) Dispersion relation of the π and π^* bands of graphene for $t = 2.7\,\text{eV}$ and $t' = -0.2\,t$. Energy units in eV. K-space coordinate units in $1/a$. A blow-up of the energy bands at one of the Dirac points is shown.

treme mechanical strength as well as extraordinarily high electronic and thermal conductivities, making it a promising candidate for a vast variety of applications in electronics, photonics, sensor technology, et cetera [9].

4.2 Theory of the de Haas-van Alphen effect of Dirac electrons

One of the most remarkable properties of graphene is its electronic structure. Graphene is a zero-gap semiconductor. Valence and conduction band touch each other at the K-points of the Brillouin zone. Expansion of the dispersion relation around these points yields a linear dependence of energy on momentum. Charge carriers in graphene hence mimic relativistic massless particles as described by the Dirac equation. This constitutes a profound difference compared to the situation in three-dimensional crystals as well as other two-dimensional electron gases (2DESs), where the dispersion relation is generally parabolic. The linear dispersion relation

also modifies quantum oscillatory phenomena, such as the Shubnikov–de Haas effect and the de Haas-van Alphen effect, which has been discussed for parabolic three-dimensional systems in Ch. 2 and for parabolic 2DESs in Ref. [40]. In fact, the exact confirmation of the predicted anomalies of the quantum Hall effect for Dirac fermions constituted the smoking gun in the seminal papers of Novoselov et al. [53] and Zhang et al. [54]. Magnetization experiments on graphene therefore seem worthwhile from a fundamental point of view since they could allow for the first-time observation of the dHvA effect of particles obeying a relativistic dispersion relation and would thus combine one of the best-known effects in solid state physics with the physics of Dirac particles. Moreover, they might also provide a means to measure the Fermi velocity, which is the proportionality constant of the linear dispersion relation, and a method to test the band structure for possible deviations from linearity. In more advanced experiments with structured graphene one might even think of the observation of the effects of different edge states on the magnetization, such as zigzag and armchair edges [55–57].

The band structure with its linear dispersion relation is at the heart of much of graphene physics. We therefore briefly comment on its features before we turn to the presentation of numerical calculations of the dHvA effect in graphene. Analytic results, which also include the quantum limit[1], are not available in literature. The numerical calculations were performed to assess the scale of the magnetization signal for different samples and also to highlight the differences compared to conventional 2DESs.

The band structure of graphene was calculated as early as 1947 using a tight-binding model Hamiltonian [44]. The calculations yield for the binding π and the anti-binding π^* band:

$$E_{\pm}(\mathbf{k}) = \pm t\sqrt{3 + f(\mathbf{k})} - t' f(\mathbf{k}), \tag{4.1}$$

where

$$f(\mathbf{k}) = 2\cos\left(\sqrt{3}k_y a\right) + 4\cos\left(\frac{\sqrt{3}}{2}k_y a\right)\cos\left(\frac{3}{2}k_x a\right), \tag{4.2}$$

and where t is the nearest-neighbor hopping energy and t' is the next-to-nearest-neighbor hopping energy. This band structure is depicted in

[1] Analytic results for low magnetic fields, i. e. $\hbar\omega_c \ll E_F$, were reported in Ref. [58].

Fig. 4.1 (b). The upper and the lower band touch each other at the K and K′-points of the Brillouin zone. Expansion of the dispersion relation around these points yields

$$E_{\pm}(\mathbf{q}) \approx \pm\hbar v_{\mathrm{F}} |\mathbf{q}| + \mathcal{O}\left((q/K)^2\right), \tag{4.3}$$

where $\mathbf{q}$ measures the momentum relative to the K- and K′-points and the Fermi velocity is $v_{\mathrm{F}} = 3ta/(2\hbar)$. The parameters t and t' are generally reported to be $t \approx 2.7\,\mathrm{eV}$ and $|t'| \lesssim 0.2t$ [49] yielding a Fermi velocity of $v_{\mathrm{F}} \approx 1 \cdot 10^6$ m/s. Equation 4.3 represents the aforementioned linear dispersion relation in the proximity of the K- and K′-points, which are also called Dirac points for this reason. The linear dispersion relation manifests itself in a cone-like shape of the band structure at the Dirac points, which is shown in a blow-up in Fig. 4.1 (b).
The Landau levels for charged particles with linear dispersion relations are given by [59]

$$E_n = \hbar\omega_{\mathrm{c}}\sqrt{n}, \quad \text{with} \quad n \in \mathbb{N}_0, \tag{4.4}$$

where the cyclotron frequency is $\omega_{\mathrm{c}} = \sqrt{2}v_{\mathrm{F}}\sqrt{(eB/\hbar)}$. Different from the parabolic case, the Landau levels according to Eq. 4.4 are not equally spaced due to the dependence on $\sqrt{n}$. Moreover, the lowest (zeroth) Landau level is pinned to zero energy while in the parabolic case the energy of the lowest Landau level $\hbar\omega_{\mathrm{c}}/2$ depends linearly on the magnetic field B (cf. Eq. 2.10). However, because both the Landau level index n and the magnetic field B enter Eq. 4.4 with a square root dependence, quantum oscillations for Dirac electrons are also periodic in $1/B$ as in the parabolic case. The Landau level degeneracy scales linearly with B:

$$D_{\mathrm{L}} = \frac{g_{\mathrm{s}} g_{\mathrm{v}}}{2\pi} \frac{eB}{\hbar}. \tag{4.5}$$

Hereby, the factor $g_{\mathrm{v}} = 2$ takes into account an additional degeneracy in graphene, which is a consequence of the honeycomb lattice consisting of two identical sublattices A and B (cf. Fig. 4.1). This degeneracy is generally termed “valley” or “pseudospin” degeneracy additional to the normal spin degeneracy g_{s}. We refrain from a further treatment of this degeneracy and only mention that it gives rise to interesting analogies between graphene and quantum electrodynamics [7, 49].
A routine for the numerical calculation of the dHvA effect at zero tem-

perature applies the following steps: First, the dependence of the chemical potential $\mu(B)$ on the magnetic field B must be derived by imposing particle conservation. As pointed out in Ch. 2, this is important for two-dimensional electron systems, where the oscillations of the chemical potential are not negligible. The particle sheet density n_0 is given by

$$n_0 = \int_0^{\mu(B)} D(B,\epsilon)\mathrm{d}\epsilon, \tag{4.6}$$

where $D(B,\epsilon)$ is the magnetic field-dependent density of states (DOS). Without disorder, it is a sum of Dirac delta functions at the positions of the Landau levels multiplied by the Landau level degeneracy, $D(B,\epsilon) = \sum_{n=0}^{\infty} D_\mathrm{L}\delta(\epsilon - E_n)$. In order to consider disorder, the δ-functions can be smeared out to properly normalized Lorentzians. Implicit solution of 4.6 yields the oscillations of the chemical potential $\mu(B)$.
As a second step, the total internal energy can now be calculated

$$U(B) = \int_0^{\mu(B)} D(B,\epsilon)\,\epsilon\,\mathrm{d}\epsilon. \tag{4.7}$$

Different to the case of parabolic 2DESs, the internal energy has a non-trivial non-oscillatory contribution $\tilde{U}$ due to fact that the Landau levels are not equally spaced. In the course of this thesis, we have derived an exact analytic expression for this contribution to U. It can be expressed as

$$\tilde{U}(B) = D_\mathrm{L}\left(\frac{E_\mathrm{F}}{2} + H_{n_B-1}^{(-1/2)}\right). \tag{4.8}$$

Hereby, the Fermi energy E_F is given by $E_\mathrm{F} = \hbar v_\mathrm{F}\sqrt{\pi n_0}$, the number n_B corresponds to the hypothetical fractional Landau level index coinciding with the Fermi energy, $n_B = (E_\mathrm{F}/(\hbar\omega_\mathrm{c}))^2$, and $H_s^{(t)}$ denotes the generalized harmonic number given by

$$H_s^{(t)} = \sum_{k=1}^{s} \frac{1}{k^t}, \quad s \in \mathbb{N}, \tag{4.9}$$

whose definition can be extended to arbitrary complex arguments s and t by

$$H_s^{(t)} = \zeta(t) - \zeta(t, s+1), \tag{4.10}$$

where $\zeta(t)$ is the Riemann zeta function and $\zeta(t, s+1)$ is the Hurwitz zeta function [60, 61]. Subtraction of $\tilde{U}(B)$ from $U(B)$ yields the oscillatory component of the internal energy

$$U_{\mathrm{osc}}(B) = U(B) - \tilde{U}(B). \tag{4.11}$$

The magnetization oscillations can now be obtained by numerical differentiation with respect to B

$$M_{\mathrm{osc}}(B) = -\frac{\partial U_{\mathrm{osc}}}{\partial B}. \tag{4.12}$$

Figure 4.2 illustrates exemplary results of this numerical dHvA routine. The calculations were performed for $n_0 = 1 \cdot 10^{13}\,\mathrm{cm}^{-2}$, which is the typical sheet density of electron-doped epitaxial graphene on silicon carbide [62, 63], which has been investigated in the course of this thesis (Sec. 4.3). Charge carrier densities of exfoliated graphene are typically smaller by about one order of magnitude. The electron density n_0 corresponds to a Fermi energy of $E_{\mathrm{F}} = 0.37\,\mathrm{eV}$. An energy-independent Lorentzian broadening with a width of 0.3 meV was included. Figure 4.2 (a) depicts the oscillations of the chemical potential $\mu_{\mathrm{osc}}(B)$ as a function of B, measured relatively to the Fermi energy, as inferred by implicit solution of Eq. 4.6. The chemical potential oscillates periodically in $1/B$ in such a manner that the electron density remains constant. Because the amplitude of the oscillations increases as a function of B, the oscillations of the chemical potential need to be taken into account in the calculation of the total energy unless $\hbar\omega_{\mathrm{c}} \ll E_{\mathrm{F}}$. In the quantum limit, i. e. when the Landau level with index $n = 1$ exceeds the Fermi energy, the chemical potential jumps to the zeroth Landau level, i. e. zero energy according to Eq. 4.4, which corresponds to $-E_{\mathrm{F}}$ when measured relatively to the Fermi energy E_{F}. This is different to the parabolic case where the energy of the zeroth level linearly scales with B and where hence the chemical potential, being pinned to the zeroth level, linearly increases as a function of B in the quantum limit (cf. Ref. [40]). Figures 4.2 (b,c) illustrate the dependence of the total internal energy U as a function of B and $1/B$, respectively, as obtained by Eq. 4.7. As noted above, unlike to the parabolic case, the total energy U features a non-oscillatory contribution. This is a consequence of the fact that the Landau levels are not equally spaced due to the square root dependence on the index n. Additional to the oscillations caused by

the consecutive passing of Landau levels through the Fermi energy as B increases, the internal energy U also depends on the number of occupied Landau levels, i. e. the number of Landau levels with energy below the Fermi energy. This fact is special to the case of a linear dispersion relation and expressed by the analytic result $\tilde{U}$ in Eq. 4.8. Another difference to the parabolic case is again the quantum limit where the internal energy drops to zero corresponding to the energy of the zeroth Landau level. In a similar fashion as for the chemical potential, the internal energy linearly increases with B in the quantum limit for a parabolic dispersion relation. In Fig. 4.2 (d) the oscillatory component $U_{\mathrm{osc}} = U - \tilde{U}$ of the internal energy is shown as obtained by subtraction of the non-oscillatory contribution given by Eq. 4.8. Numerical differentiation of U_{osc} leads to the dHvA oscillations of magnetization M_{osc}, which are depicted in Figs. 4.2 (e,f) as a function of B and $1/B$, respectively. As B increases, the amplitude of the dHvA oscillations also increases slightly. This is again a consequence of the Landau levels not being equidistant in energy for a linear dispersion relation. In 2DESs with parabolic dispersion relations, the amplitudes are constant in the ideal case of zero level broadening.

4.3 Overview of graphene samples, magnetization experiments, and experimental technique

In the course of the research for this thesis, several magnetization experiments with graphene samples produced by different techniques have been carried out:

(1) Graphene was grown on copper foils by chemical vapor deposition by Dr. Paul Berberich (group of the present author). The copper foil was etched away in an acid solution from where the floating graphene sample was skimmed with a GaAs single crystal sample covered with an Al_2O_3 layer for better visibility of the graphene sheet. Subsequently, a micromechanical cantilever magnetometer (MCM) was prepared from the combined GaAs/Al_2O_3/graphene sample such that graphene was monolithically integrated into the magnetometer [64].

(2) Graphene was grown on copper foils by chemical vapor deposition [6,65] in the group of Dr. José Garrido of Technische Universität

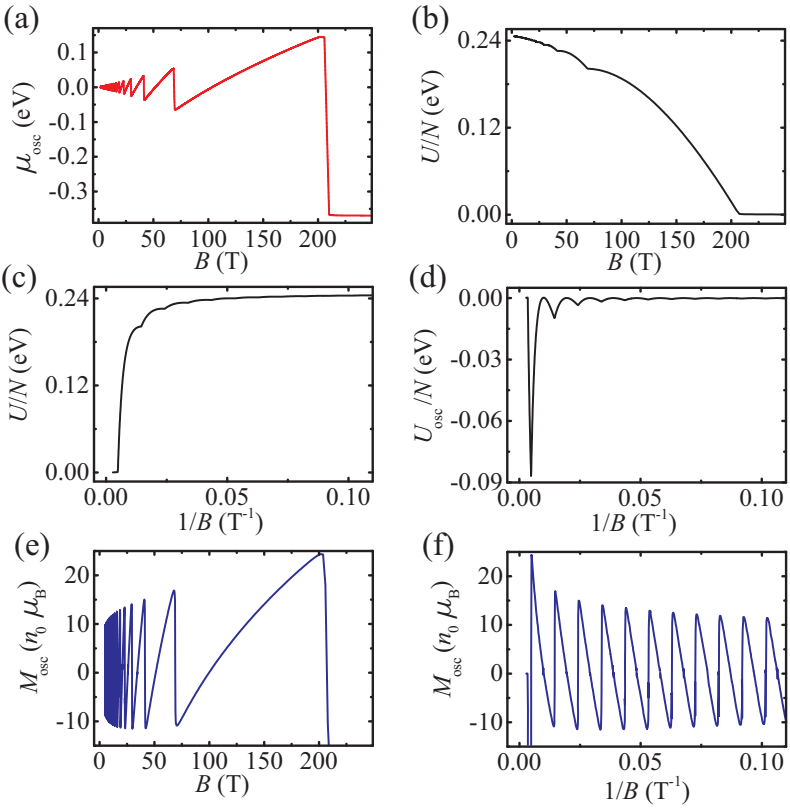

Figure 4.2: Numerical calculation of the dHvA effect for a two-dimensional electron system with linear dispersion relation. The calculation was performed for a sheet density of $n_0 = 1 \cdot 10^{13}\,\mathrm{cm}^{-2}$ and with an energy-independent Lorentzian broadening of the Landau levels of 0.3 meV. (a) Oscillating contribution μ_{osc} to the chemical potential as a function of magnetic field strength B. (b) Energy per electron U/N as a function of field strength B. (c) Energy per electron U/N as a function of inverse field strength $1/B$. (d) Oscillatory component of the energy per electron U_{osc}/N as a function of inverse field strength $1/B$. (e) Oscillatory component M_{osc} of magnetization as a function of field strength B in units of $n_0\mu_{\mathrm{B}}$. (f) Oscillatory component M_{osc} of magnetization as a function of inverse field strength $1/B$ in units of $n_0\mu_{\mathrm{B}}$.

München. The copper foil was again etched away and the graphene sample was skimmed with a silicon sample of $45\,\mu m$ thickness covered with 300 nm thermal SiO_2. The Si/SiO_2/graphene sample was then transferred onto a GaAs-based MCM. This modification of the previous experiment was performed since it had been assumed that the graphene sample had suffered from a severe deterioration in terms of electronic quality in the preparation process of the MCM with monolithically integrated graphene [66]. Figure 4.3 (b) shows a photographical image of the Si/SiO_2/graphene sample attached to the paddle of the GaAs-based MCM.

(3) Graphene was epitaxially grown on the Si-terminated side of $6H$-SiC samples of $140\,\mu m$ thickness in the group of Prof. Thomas Seyller of Friedrich-Alexander-Universität Erlangen-Nürnberg (present affiliation: Technische Universität Chemnitz). Raman spectroscopy examination of the samples verified a coverage with predominantly monolayer graphene (MLG). The SiC/Graphene samples were attached onto a GaAs-based MCM [66]. Figures 4.3 (a,c) show atomic force microscopy (AFM) images of one of the investigated epitaxial graphene samples, where Fig. 4.3 (a) depicts the height profile and Fig. 4.3 (c) the phase contrast at the same sample position.

(4) The previous experiment was repeated with MLG samples on thinner SiC samples ($40\,\mu m$ thickness) in order to reduce a strong paramagnetic signal attributed to point defects of the SiC substrate [67].

(5) Quasi-free-standing monolayer graphene (QFMLG) was epitaxially grown on $6H$-SiC samples with an intercalated hydrogen layer [68] in the group of Prof. Thomas Seyller. The homogeneity of the graphitization process was examined with Raman spectroscopy by scanning a sample in $10\,\mu m$ steps from the edge to the middle. It was found that only at a distance of $\sim 100\,\mu m$ from the edge, the graphitization process led to predominantly MLG/QFMLG. Closer to the edge, multilayer graphene or graphite, respectively, dominated [69]. For this reason, the graphitic residues at the sample edges were etched away in an oxygen plasma incinerator with a protective resist coating applied to the central sample region. The resist was subsequently removed and the sample was attached to a GaAs-based

MCM [67]. Figure 4.3 (d) shows a photographical image of the QFMLG sample on SiC with a droplet of the protective PMMA resist applied before incineration.

(6) The development of Si-based MCMs on the micrometer scale with 200 nm thickness, which would in principle allow for the observation of the dHvA effect of exfoliated graphene flakes, was initiated [66].

The GaAs-based MCMs of experiments (1-5) use the same working principle as the CuBe-based MCMs described in Ch. 3, but achieve a sensitivity that exceeds the CuBe MCMs by approximately two orders of magnitude due to smaller dimensions. Figure 4.4 depicts a drawing, true to scale, of a GaAs MCM mounted to a sapphire substrate by fixing the cantilever's foot of dimensions $2 \times 3\,\mathrm{mm}^2$ with a conductive glue. The cantilever features a paddle, which carries the sample and whose bottom side is metallized with gold palladium (AuPd) for capacitive readout of the cantilever's deflection. The sapphire substrate also comprises appropriately formed Au-metallized surface areas in order to contact the paddle electrode and to form the counterelectrode for the paddle. The distance of the paddle and the substrate electrode is determined by the foot height and is usually set to 80-150 µm. The beam width is 100-200 µm and the paddle dimensions of $1.2 \times 2.0\,\mathrm{mm}^2$ determines the maximum sample size which can be examined (usually $1.0 \times 1.8\,\mathrm{mm}^2$). The preparation of the GaAs-based MCMs involves photolithographical, wet etching, and thermal evaporation techniques for metallization and is described in detail in Refs. [40, 70, 71].

4.4 Experimental outcome

Magnetization experiments (1-5) as listed in Sec. 4.3 were conducted in broad field and temperature ranges. In each case, our detailed data analysis showed that none of the different and complementary approaches provided us with a signal that could be attributed to the respective graphene layer. We refrain from a detailed discussion of all experimental results and only exemplify the experiments by a brief presentation of experiment (3) from Sec. 4.3.
The relevant graphene was synthesized on silicon carbide (SiC) by subli-

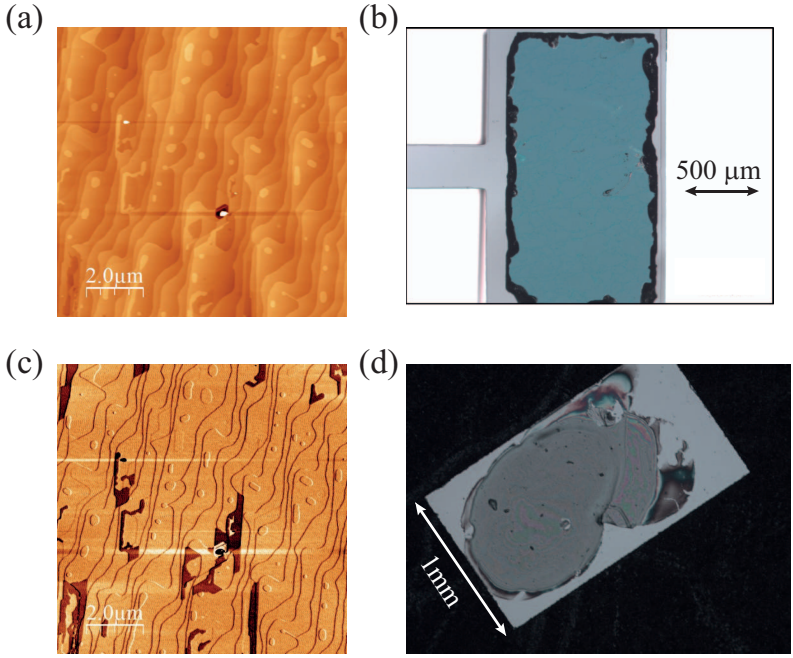

Figure 4.3: Various large-area graphene samples, which have been investigated. (a) AFM height profile of a sample of epitaxial graphene on the Si-terminated side of 6H-SiC. The typcial terrace structure of SiC when treated by chemical-mechanical polishing and subsequent annealing can be seen. (b) Sample of CVD-grown graphene on a Si substrate with a layer of thermal SiO_2 on the paddle of a GaAs-based cantilever. The graphene sheet forms wrinkles on the substrate, which are weakly visible. (c) AFM phase contrast profile of the same sample and at the same position as in Fig. (a). The darker areas can be attributed to regions with bilayer or few-layer graphene. (d) Sample of quasi-free standing monolayer graphene on the Si-terminated side of 6H-SiC, partially covered by a droplet of PMMA resist. The resist was applied in order to protect the central region of the sample in an incineration process step of few-layer graphene regions and graphitic residues at the sample edges.

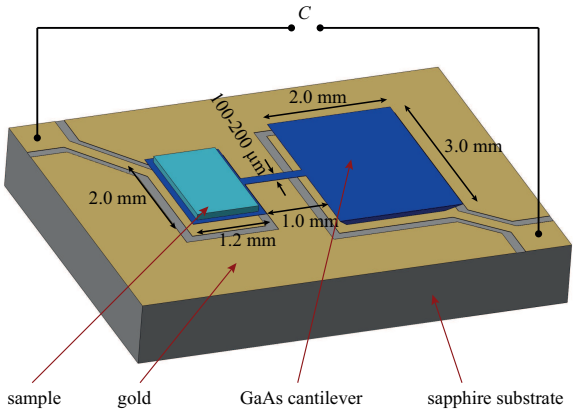

Figure 4.4: Drawing of a GaAs-based micromechanical cantilever magnetometer (MCM). The cantilever with a metallized bottom side is attached to a sapphire substrate. The substrate comprises appropriately formed Au-metallized surface areas in order to contact the cantilever paddle electrode and to form a counterelectrode for the paddle for capacitive readout of the cantilever's deflection. The thickness of the paddle and the beam is $\sim 4.5\,\mu$m. The dimensions of the cantilever paddle, onto which the sample is placed, are $1.2 \times 2\,\mathrm{mm}^2$ and the length and width of the beam are given by 1.0 mm and 100-200 µm, respectively.

mation of Si atoms [72,73]. Such epitaxial graphene is a graphene realization which features a lot of the salient features of ideal graphene. Amongst the scalable production techniques it yields graphene of the highest electronic quality [74]. Although the high substrate costs of SiC will probably prevent it from becoming a general competitor to Si-based devices, epitaxial graphene is a promising candidate for some niche applications [75]. For detailed reviews of epitaxial graphene physics and possible applications see Refs. [76–78].

The samples for experiment (3) were prepared from a 2 inch 6H-SiC wafer, which had been thinned down to $140\,\mu$m and intentionally polished by NOVASiC[1] using a chemical-mechanical technique to guarantee an atomically flat surface ready for epitaxy. The polished wafer was then cut into samples of size $1.0 \times 1.8\,\mathrm{mm}^2$ and graphene was epitaxially grown on the Si-

[1] NOVASiC, Allée du Lac d'Aiguebelette, Savoie Technolac, 73370 Le Bourget-du-Lac, France

terminated side of the samples in the group of Prof. Seyller at Friedrich-Alexander-Universität Erlangen-Nürnberg using a thermal graphitization technique which has been described in detail elsewhere [79, 80]. Raman spectroscopy established that the samples were covered by predominantly monolayer graphene (MLG) [66, 69]. The samples were also scrutinized by means of atomic force microscopy (AFM). Figures 4.3 (a,c) show typical AFM images of the investigated samples, where Fig. 4.3 (a) depicts the height profile and Fig. 4.3 (c) the phase contrast of the same position on the same sample. Both images show the typical terrace structure formed by the SiC substrate when treated by chemical-mechanical polishing and subsequent annealing in the epitaxial growth procedure. The step height between the terraces is ~ 1.5-3 nm, which corresponds to the scale of the $6H$-SiC unit cell with c = 15.1198 Å [81]. From the images it can also be inferred that the terrace width is on the scale of 1 µm, which establishes an excellent sample quality [69, 79]. The phase contrast image Fig. 4.3 (c) shows darker areas, which we attribute to regions with bilayer graphene or few-layer graphene (FLG) [69]. The area ratio covered by such undesired FLG crystallites is small, which confirms the finding from the scanning Raman spectroscopy.

Figure 4.5 shows typical raw capacitance data C versus magnetic field B from magnetization experiments performed with the epitaxial graphene samples on $6H$-SiC at temperature T = 290 mK with a GaAs MCM as depicted in Fig. 4.4. A large paramagnetic overall signal is found, which is argued to stem from point defects of the SiC samples [67]. To isolate a possible signal stemming from the epitaxial graphene layer, a low-order polynomial fitting function was subtracted from the raw data. The resulting reduced capacitance data ΔC are shown in Fig. 4.6 (a), where the color discerns data from different magnetic field sweeps (black: up-sweep 1, red: down-sweep 1, blue: up-sweep 2, green: down-sweep 2). Sawtooth-like features are present. They were traced to a technical issue in that the employed capacitance bridge re-balanced repeatedly. This process was periodic in changes of the overall signal by 2.5 fF. To eliminate this feature and to study the data in detail for graphene magnetization, we implemented an algorithm that detected the positions of the jumps, analyzed the respective amplitudes of the jumps, discarded data in a range of ±26 mT around the jumps, and subtracted the amplitudes in the original raw data C for all field values greater than the jump position in such a manner that the parasitic jumps were removed. The processed data are shown in Fig. 4.6 (b)

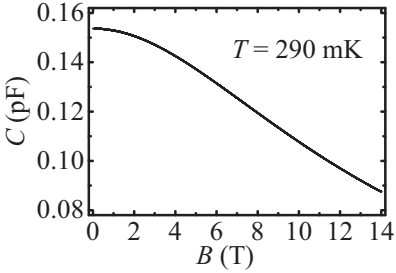

Figure 4.5: Raw capacitance data C versus magnetic field B from magnetization experiments performed with an epitaxial monolayer graphene sample on $6H$-SiC at temperature T = 290 mK. A large paramagnetic overall signal is found, which can be attributed to point defects of the SiC samples [67].

were the subtraction was performed for the reduced data ΔC for the purpose of illustration. Subsequently, a low-order polynomial was fitted to the reconstructed data C_{rec} to discard the paramagnetic substrate signal. The resulting data ΔC_{rec} are shown in Fig. 4.6 (c) versus inverse magnetic field. Figure 4.6 (c) contains an oscillating feature of two periods. It illustrates a principal dilemma when large overall signals are tested for possible (low-frequency) quantum oscillations on a scale which is lower by several orders of magnitude: If oscillations are present, a polynomial of reasonably high degree must be subtracted to isolate them. At the same time, it is difficult to discern between oscillating features artificially introduced by the subtraction of the polynomial and possible physical oscillations. To gain clarity, the experiment was repeated with a pure substrate, which had not undergone the graphitization procedure, under exactly the same experimental conditions as for the graphene samples. Subsequently, exactly the same data analysis was carried out. Figure 4.6 (d) depicts the resulting data. The close similarity to the data in Fig. 4.6 (c) suggests that the epitaxial graphene layer did not contribute a discernible magnetic signal. We attribute the remaining oscillating signals to artificially created oscillations when subtracting the polynomial fitting function.
As mentioned in Sec. 4.3, the experiment was modified and repeated in order to address issues which might have prevented the observation of a graphene magnetization signal. To reduce the influence of the substrate,

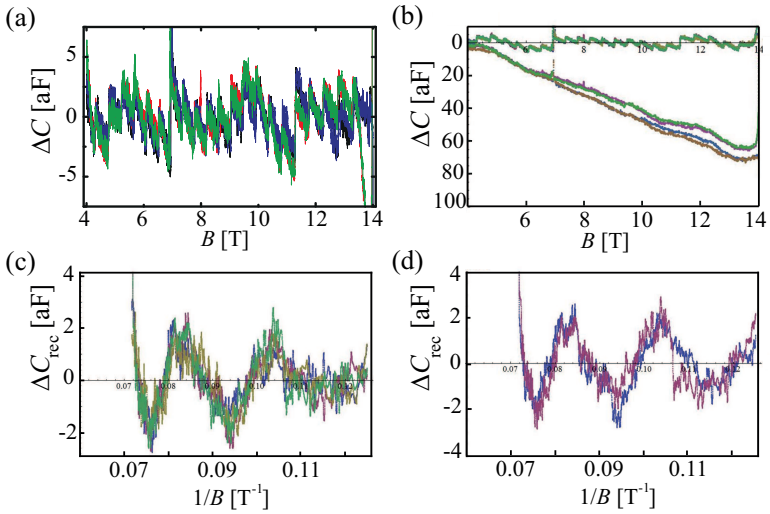

Figure 4.6: Analysis of the experimental raw data of Fig. 4.5 from a sample with epitaxial graphene on $6H$-SiC. (a) Capacitance data ΔC after subtraction of a low-order polynomial fitting function versus magnetic field B. The sawtooth feature stems from a period re-balancing of the employed capacitance bridge. (b) Elimination of the sawtooth jumps from the data in Fig. (a) after application of a dedicated algorithm. (c) Reconstructed capacitance data ΔC_{rec} after elimination of parasitic jumps in the raw data and subtraction of a low-order polynomial fitting function. (d) Capacitance data from a pure $6H$-SiC substrate sample after application of the same processing steps as illustrated in Figs. (a-c) for the $6H$-SiC sample with epitaxial graphene.

thinner samples (40 µm) were used. Additionally, samples where edges had been cleaned with oxygen plasma were investigated as well as samples with an intercalated hydrogen layer promising a better electron mobility [68]. Moreover, the capacitance bridge was operated in a mode in which it did not re-balance, but used the voltage deviation from the balancing point, found at the beginning of the field sweep, as the direct output. However, a magnetic signal attributed to graphene could not be deduced in any of the experiments.

We conclude that to date large-area graphene samples are not provided with an electronic quality and sample homogeneity sufficient for the observation of magnetic quantum oscillations of Dirac electrons. Electron mobilities at cryogenic temperatures of good epitaxial MLG and epitaxial QFMLG samples amount to $2000\,\mathrm{cm}^2/(\mathrm{Vs})$ [63] and $3000\,\mathrm{cm}^2/(\mathrm{Vs})$ [68], respectively, but this still falls short of the mobilities achieved in 2DESs in semiconductor and oxide heterostructures, where the dHvA effect is routinely observed, by approximately two to three orders of magnitude (e. g. $1 \cdot 10^5\,\mathrm{cm}^2/(\mathrm{Vs})$ [82], $1.4 \cdot 10^6\,\mathrm{cm}^2/(\mathrm{Vs})$ [83], $3.7 \cdot 10^5\,\mathrm{cm}^2/(\mathrm{Vs})$ [84], $2.9 \cdot 10^5\,\mathrm{cm}^2/(\mathrm{Vs})$ [85]). Measurements of Shubnikov-de Haas oscillations and the quantum Hall effect have been reported for epitaxial monolayer graphene by Jobst et al. [62, 63]. However, these experiments were performed in a high-field laboratory and the effects could only be clearly shown for magnetic fields $\gtrsim$ 10-12 T. For lower fields, no quantum oscillations were observed even after background subtraction routines similarly to ours had been applied [86]. Moreover, the Hall bar for the transport measurements in Refs. [62, 63] was patterned on a single SiC terrace (Fig. 4.3 (a)) and had lateral sizes on the scale of a few micrometers. Thus, a considerably higher electronic homogeneity can be assumed than for our samples where the epitaxial graphene layer extended over millimeters and numerous terraces. Reference [62] provides a histogram of charge carrier densities in 51 different MLG samples (Fig. 2) showing a considerable distribution of the densities between 7 and $13 \cdot 10^{12}\,\mathrm{cm}^{-2}$. If it is assumed that this distribution does not only apply to different samples, but also to different positions on the same sample due to doping by surface defects, crystallite grain boundaries etc., a considerable position-dependent variation of the dHvA frequency is the consequence. Following Schoenberg's arguments (cf. Sec. 2.34 and Ref. [20]), this would cause a massive smearing of dHvA oscillations due to sample inhomogeneity. In the light of these arguments, we consider our results to be consistent in that our high-

sensitivity torque magnetometers did not allow us to observe the dHvA effect in large-area graphene samples.

5 Sample head for cantilever magnetometry with interferometric readout

In this chapter, we present the design and assembly of a sample head for magnetization experiments at low temperatures down to 280 mK and high magnetic fields employing a cantilever-based magnetometer with a fiber-optical interferometric readout. We briefly explain the experimental motivation that led to the development of a new sample head (Sec. 5.1) before turning to general design considerations (Sec. 5.2) and their implementation in the final realization of the sample head (Sec. 5.3).

5.1 Motivation

The development of a new sample head was pursued in order to provide an additional system for torque magnetometry experiments employing an optical readout scheme and particularly to allow for the optical readout of cantilevers with lateral dimensions on the micrometer scale. In the following, the optical readout scheme is compared to the capacitive technique given in Sec. 3.3 and the desirability of a system designed for the employment of miniaturized cantilevers is briefly discussed.
For torque magnetometry on two-dimensional electron systems (2DESs), GaAs-based cantilevers have successfully been employed in a long series of studies [70, 82–85, 87–98]. While the CuBe cantilever, detailed in Sec. 3.2, have the advantage of being comparably robust, straightforward to produce, and able to support a large sample weight of a few grams, the semiconductor-based cantilevers from GaAs have a better sensitivity due to their smaller dimensions, which exceeds the CuBe cantilevers by approximately two orders of magnitude. Conventional readout of such GaAs cantilvers employs a capacitive scheme [70] which is essentially the same as for the CuBe cantilevers presented in Sec. 3.3. For this purpose, a thin AuPd layer is evaporated onto the backside of the GaAs cantilever. Thus, the metallized cantilever and a substrate with an appropriate counter electrode permit a capacitive readout of the cantilever's deflection.

An alternative route [93] is an optical readout where infrared laser light is guided through a fiber and directed onto a metallized surface of the cantilever's paddle or beam. The light is reflected and coupled back into the fiber thus forming a Fabry-Pérot interferometer. The distance between the cantilever and the fiber ending is controlled by a piezo stack. A feedback loop is employed to keep this distance constant by applying a voltage to the piezo stack. In this manner, the voltage applied to the piezo by the feedback loop can serve as a measurement signal proportional to the cantilever's deflection.
The two readout techniques complement each other. The capacitive technique is preferable in situations where the laser light could cause undesired effects on the investigated sample such as heating or electronic excitation. It also allows for rotations of the sample system and hence angle-dependent magnetization measurements in uniaxial magnets while the optical technique requires a fixed orientation of the cantilever relative to the fiber. Moreover, the capacitive technique is more robust with respect to external vibrational disturbance due to its open-loop design. The chief advantages of the optical readout are a further increase in sensitivity of approximately one order of magnitude for the GaAs cantilevers and, for 2DESs, the ability to incorporate field effect electrodes. The latter is difficult with the capacitive readout due to crosstalk effects.
The advancement of experimental capabilities to miniaturized cantilevers with dimensions of a few micrometers seems desirable for various reasons. Continued interest to study magnetic properties via micromechanical means [99, 100] and the ability of high-resolution dHvA measurements on crystals which cannot be grown in large single crystals yet are prime examples. Capacitive readout reaches its limits for cantilevers with such dimensions because the capacitance signal scales with the electrode area formed by the cantilever. For this reason, the optical technique is the preferred choice for microcantilevers. However, this demands the ability to exactly position the cantilever with respect to the optical fiber guiding the laser light. Moreover, the positioning needs to be adjustable in an ultracold environment because a misalignment can be caused by the cool-down from room temperature due to different thermal expansion coefficients of the materials of the sample head and in the cantilever itself.
The availability of a robust system for optical readout of the conventional GaAs cantilevers for increased experimental flexibility as well as the aforementioned requirements for experiments with miniaturized cantilevers were

the stimuli for the development of the sample head.

5.2 Design considerations

For the design of a sample head for torque magnetometry experiments in high magnetic fields at low temperatures, various geometrical, mechanical, and electrical constraints as well as experimental requirements need to be considered. In the following, we briefly discuss the main aspects.

(1) **General geometric considerations.** The sample head is to be attached to an existing vacuum loading ^{3}He system and the system is to be used in existing superconducting solenoids. This imposes two geometrical constraints. The sample head must fit into the inner vacuum chamber (IVC) of the ^{3}He system and the sample position within the sample head must allow to reach the field center of the solenoids when the ^{3}He system is immersed into the bath cryostat containing the solenoid.

(2) **Fine positioning of the cantilever.** For the optical readout technique, the cantilever's position needs to be adjustable along three spatial directions. Moreover, the angle of the normal of the cantilever should be adjustable. The fine positioning ability is important to optimize the coupling of the reflected light back into the fiber after cool-down to cryogenic temperatures. For miniaturized cantilevers it is essential because misalignment due to thermal expansion properties must be expected to be on the same scale as the cantilever's dimensions. The required positioning abilities demand for four positioning units corresponding to three spatial directions and one angle.

(3) **Experimental angle.** For the static equilibrium measurement technique on 2DESs, a finite angle ϑ between the magnetic field axis and the cantilever normal is required because the torque vanishes for zero angle. For the optical readout, a standard angle of $\vartheta = 15°$ is established. Future experiments might however apply a resonant measurement scheme where the torque effected by the sample magnetization shifts the spring constant and hence the oscillation frequency of the cantilever [101]. For this technique, it was decided that the sample head should also allow for an experimental angle of $\vartheta = 0°$.

(4) **Cantilever coordinates vs. lab coordinates.** It is preferable to position the cantilever with respect to a reference system which is spanned by the direction of the cantilever beam, the surface normal of the cantilever and the direction perpendicular to both the beam and the normal. This system is referred to as sample coordinates (x, y, z) and is depicted in Fig. 5.2 (a). For the design with experimental angle $\vartheta = 15°$, this reference system is not parallel to the lab coordinates (X, Y, Z), which are spanned by the direction of the magnetic field $\mathbf{B}$ and two directions perpendicular to $\mathbf{B}$. This difference needs to be adjusted for in such a manner that any linear positioning unit only drives one specified axis of the cantilever coordinates. Similarly, the angular positioning unit travels on a circle of radius $r = 32.8\,\mathrm{mm}$. It is preferable that the effect of the angular positioning unit at the sample position is only a variation of the angle with respect to the lab system, but no linear travel.

(5) **Experimental access, accommodation, and protection of wiring and optical fiber.** The experimental head must provide enough space to accommodate numerous wires and associated connectors. The positioning units alone require 4×2 wires for driving and 3×3 wires for readout. The piezo stack for the optical fiber and the calibration coil of the cantilever require four additional mandatory wires for the optical readout technique. This is complemented by additional optional wiring required by the experimental situation such as the implementation of a gate terminal or simultaneous electrical transport measurements. At the same time, experimental access in order to mount the sample must be guaranteed and both thin wires and the fragile optical fiber must be protected.

(6) **Wiring of the positioning units.** The working principle of the positioning units is a stepper slip-stick technology that requires the application of sawtooth voltage signals to a piezoelectric actuator, which represents a high capacitive load [102]. For this reason, the ohmic resistance of the wires driving the positioning units needs to be less than $5\,\Omega$ in order to guarantee the required sharp voltage flanks.

(7) **Load capacities.** The loads which the positioning units are able to move are limited. This needs to be taken into account when stacking different positioning units and designing other structural parts.

5.3 Implementation

Figure 5.1 depicts a computer-aided drawing of the sample head in the ϑ = $15°$ configuration. The sample head consists of a main body (transparent) in the upper part. The piezo stack (green) for the optical fiber is attached via a support plate to the main body. Two elongated side parts extend on opposite sides from the main body downwards. The side parts carry a stack of various parts. From bottom to top, the stack consists of: a carrier part, a linear z-positioner (blue), a spacer part 1, an angular positioner (blue), a linear y-positioner (blue), a spacer part 2, a linear x-positioner (blue), and a sample holder (black) carrying a chip carrier (brown) for the sample. The chip carrier is located at a position in the proximity of the piezo stack for the fiber, with its surface perpendicular to the piezo stack axis.
In the following, we describe how the various constraints outlined in the previous section were addressed in the final design:

(1) The general geometric constraints were met by observing corresponding limits for the overall dimensions. In order to accommodate the sample head inside the IVC, the cross section of the sample head perpendicular to its axis fits into a circle of radius $38\,\text{mm}$. This corresponds to the form of the IVC, which is cylindrical with an inner radius of $40.5\,\text{mm}$. Similarly, the length along the axis was chosen to be approximately $\sim 185\,\text{mm}$. The position of the sample chip carrier is located on the central axis and $13.5\,\text{mm}$ offset from the top of the sample head. This distance is dictated by the dimension of the existing solenoids and in particular the position of their magnetic field centers.

(2) In order to implement the required fine positioning abilities, three linear and one angular positioner employing a piezo slip-stick stepper technique, produced by attocube systems AG, were acquired. They are shown in blue in Fig. 5.1. The fine positioners are designed to function in ultracold environments and high magnetic fields and allow fine positioning with a precision of $\sim 1\,\mu\text{m}$ and $0.02°$ at T = $4\,\text{K}$. Figure 5.2 (b) depicts a linear positioner for horizontal travel.

(3) The main body was designed such that the support plate for the optical fiber can be mounted to the body at $\vartheta = 15°$ and $\vartheta = 0°$. For the sake of brevity, we restrict ourselves here to the illustration of

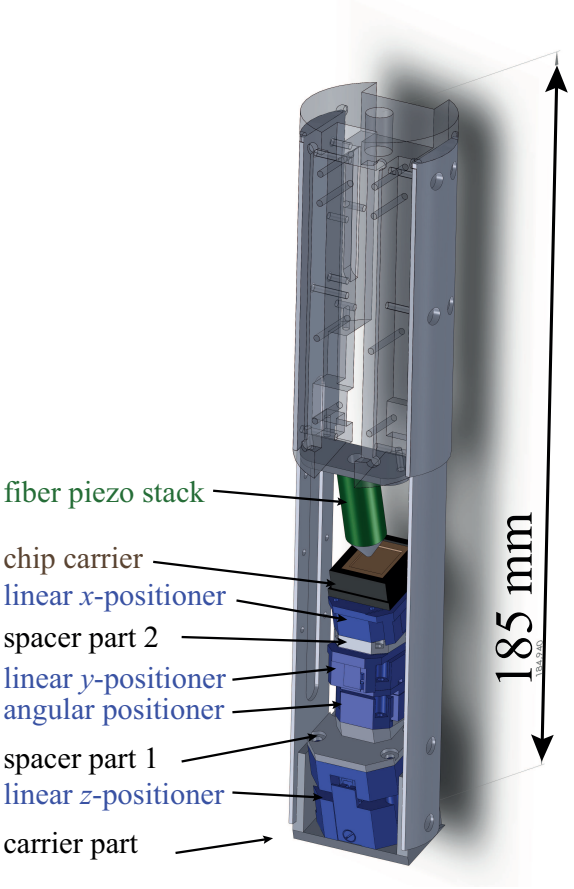

Figure 5.1: Computer aided drawing of the entire sample head in the 15° configuration. The main body of the sample head (transparent) houses the optical fiber (not shown) and experimental wiring along with associated connectors (not shown). The piezo stack holding the optical fiber is mounted on the main body. Two elongated side parts extend downwards and carry the positioning stack consisting of three linear and one angular positioner and different spacer parts with the chip carrier for the cantilever sample on top of the positioning stack.

the $15°$ configuration depicted in Fig. 5.1. The carrier part and the spacer parts for the positioning stack were also designed and built in another version in order to realize the $\vartheta = 0°$ geometry.

(4) The difference of sample coordinates (x, y, z) and (X, Y, Z) is adjusted for by the specific design of the structural parts of the positioner stack in such a manner that any linear positioner only drives one specified axis of the sample coordinates. This is illustrated in Fig. 5.3 (a). The carrier part tilts the z-positioner by $15°$ with respect to the Z-axis. Spacer part 1 reverses this angle again. It carries the angular positioner and the y-positioner whose axis is parallel to the corresponding lab axis Y. Spacer part 2 reintroduces the $15°$ angle for the x-axis of the sample coordinates. Spacer part 2 also adjusts the distance along the stack in such a way that the center of the circle along which the angular positioner travels exactly meets the sample surface (indicated by the circle). There are further detailed constraints on the design following from the general geometric constraints (1), which we omit here.

(5) The space to accommodate and protect wires, connectors, and the optical fiber is provided by the main body. It is machined to contain two separate cavities. One is designated for the fiber such that it can be isolated from the wiring. The other cavity houses the wiring. It contains a number of grooves and threads for mounting of various connectors. Also, one of the elongated side parts contains a groove to lead the experimental wiring to the chip carrier.

(6) The constraint on the ohmic resistance of the wiring used to drive the positioners requires the use of copper instead of Constantan, which is common in wiring for experiments at cryogenic temperatures below 1 K and is the wiring supplied by the manufacturer of the ^{3}He system. Due to its very high thermal conductivity, pure copper wiring for the positioners would however introduce a high heat load with negative consequences for the experiment. This suggests the use of superconducting NbTi wires. However, in high magnetic fields the superconducting phase could break down inflicting sudden jumps of the wire resistance to a few hundred Ohms. Furthermore, driving the positioners leads to substantial heating due to dissipation. A direct NbTi wiring to the positioners is therefore not advisable be-

cause the heating can destroy the superconducting state. Last but not least, the heat sinking of the positioners is aided by the experimental wiring, which should ensure a good thermal contact to the ^{3}He pot. For this reason, a hybrid solution is chosen, which is sketched in Fig. 5.3 (b). Copper wiring is employed between the connector at the outside of the ^{3}He system at room temperature and the 1 K-pot of the ^{3}He system. This guarantees a low ohmic contribution. The copper wiring is thermally anchored at the 1 K-pot. It is then continued by NbTi wiring between the 1 K-pot and the ^{3}He pot of the ^{3}He system. This superconducting section guarantees zero ohmic resistance while at the same time avoiding a thermal bridge from the 1 K-pot to the ^{3}He pot.The wiring then switches back to copper and is thermally anchored at the ^{3}He pot. From there it leads to the positioners. To facilitate efficient handling, connectors are integrated at various positions.

(7) The load constraints were fulfilled by the use of a stronger (and larger) z-positioner (type ANPz101) compared to the x, y-positioners (type ANPx51). Also, the spacer parts 1 and 2 were milled with large recesses in order to lower their mass. By doing so, the upper load constraints on the angular positioner could be met exactly.

Figure 5.4 depicts two photographical images of the sample head that has been built along the guidelines discussed above. All structural parts have been machined out of titanium. Also, all screws, which are used to mount the various parts onto each other, are out of titanium to achieve a high degree of expansion matching. Figure 5.4 (a) shows the sample head from a similar perspective view as the drawing in Fig. 5.1 and Fig. 5.4 (b) shows the opposite side. Various parts discussed above can be found in the implementation. We restrict ourselves to pointing out a few of them. At the top the copper made ^{3}He pot of the ^{3}He system can be seen as well as the ^{4}He capillary of the system. Also, a thermal anchor to the ^{3}He pot for the copper wires leading to the positioners is depicted. In Fig. 5.4 (a) the cavity housing the optical fiber is covered by a protective plate. On the opposite side, the cavity for the wiring and the connectors is open. Various connector plugs and numerous experimental wires are visible. Further down, the piezo stack for the optical fiber can be seen. This is followed by the sample holder with the chip carrier. Wiring for gate-controlled magnetization experiments and simultaneous transport measurements on a 2DES leads to

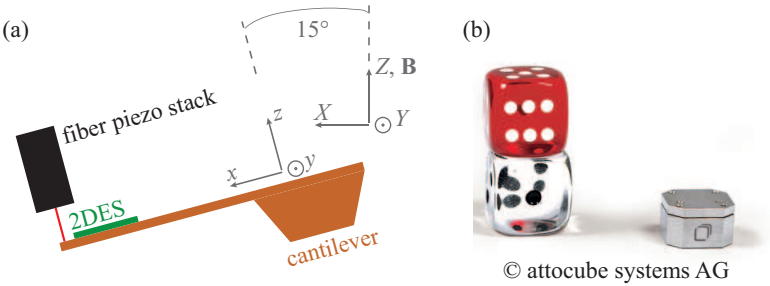

Figure 5.2: (a) Sample coordinate system (x, y, z) vs. lab coordinate system (X, Y, Z). The sample coordinates are rotated by 15° with respect to the lab coordinates in the standard constellation for experiments on two-dimensional electron systems (2DES) with optical readout. (b) Photographical image of a ANPx51-type linear positioner from attocube systems AG. Two units of this type are used as x- and y-positioners in the positioning stack of the sample head.

a printed circuit board onto which the holder for 32 pin-leadless chip carriers is mounted. The sample holder resides on the top of the positioning stack consisting of the three linear positioners, the angular positioner from attocube systems AG, and the various spacer parts. It can also be seen how the experimental wiring is guided through one of the side parts of the sample head.

The sample head was employed in numerous experiments not presented in this thesis. With respect to the measurement technique and the sample head's performance, these experiments were successful. The positioning system proved to work reliably under the experimental conditions. Figure 5.5 illustrates an exemplary experiment with the sample head. Figure 5.5 (a) shows a photographical image of a GaAs-based cantilever attached to a substrate that is mounted in the chip carrier of the sample head. The fiber for the optical readout scheme is also visible. It points onto a surface part of the cantilever's paddle which is metallized with gold for better reflection. Figure 5.5 (b) shows a microscope picture of the paddle of a GaAs-based cantilever with a sample attached, which has been prepared by the present author. The metallized surface part for the readout is visible in the upper part of the image. The transparent sample of rectangular shape can be seen below the metallized surface. It is an oxide heterostructure of

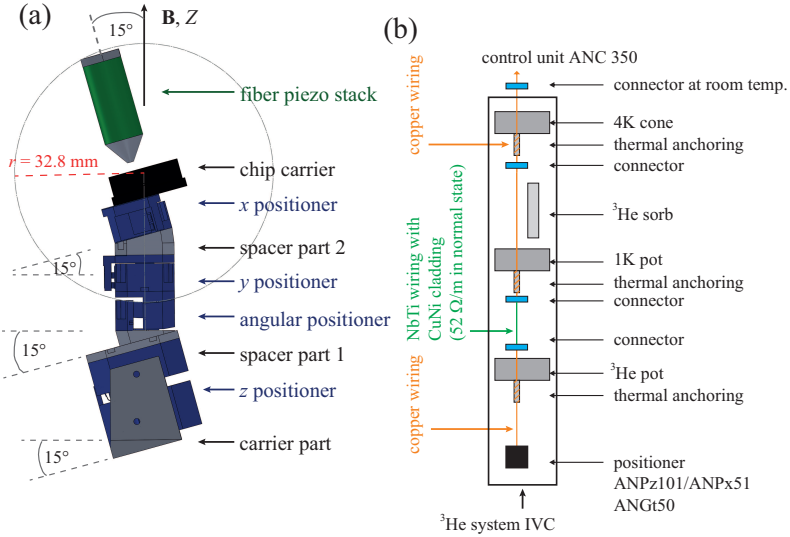

Figure 5.3: (a) Positioning stack in the 15° constellation. The stack is carried by a carrier part that introduces the 15° angle for the z-positioner. The angle is reversed by spacer part 1 carrying the angular positioner and the y-positioner. The 15° angle is reintroduced for the x-positioner by spacer part 2. The chip carrier for the cantilever sample is mounted on top of the positioning stack beneath the piezo stack for the optical fiber, which is attached to the main part of the sample head (not shown). The various 15° inclined parts guarantee that the sample coordinates x and z are parallel to the cantilever beam and the cantilever normal, respectively. (b) Schematic illustration of the wiring for the piezo slip-stick positioners from attocube systems AG. A hybrid solution of copper and NbTi superconducting wiring is employed inside the inner vacuum chamber (IVC) of the ^{3}He system in order to guarantee both low ohmic resistance to the piezo actuators and low heat load to the experiment at the same time.

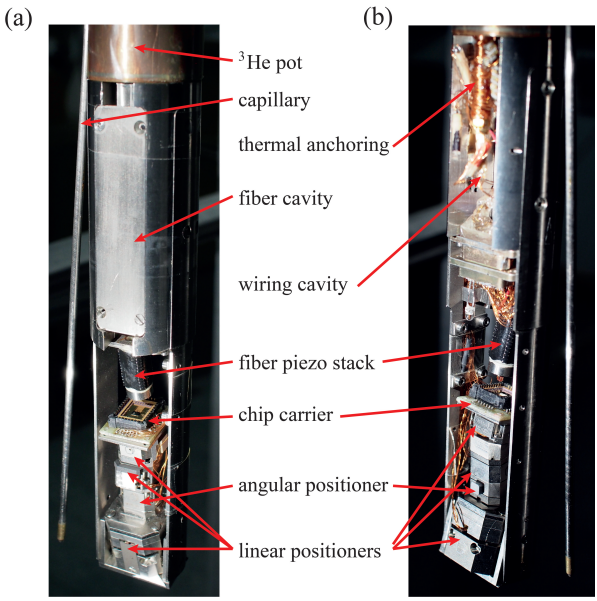

Figure 5.4: Photographical images of the sample head. Fig. (a) shows a similar perspective view as Fig. 5.1 and Fig. (b) shows the opposite side. The ^{3}He pot and the ^{4}He capillary of the ^{3}He system can be seen as well as a thermal anchor of the positioner wiring to the ^{3}He pot. The two cavities for the optical fiber and the wiring are indicated. Further down, the piezo stack for the optical fiber is visible. Beneath the piezo stack, the positioning stack consisting of the linear and angular positioners as well as the chip carrier with the sample can be seen.

MgZnO/ZnO, which features a 2DES at the interface. Shubnikov-de Haas oscillations have been reported for this material [103]. The sample was provided by the group of Prof. M. Kawasaki from the University of Tokyo. The sample has been prepared for simultaneous measurement of magnetization and electric transport by the present author. For this, four contacts to the 2DES were defined by optical lithography and realized by argon milling and in-situ evaporation of Ti/Al. They are visible in the corners of the sample. Corresponding contact lines were prepared on the cantilever for a four-point measurement of resistivity. The sample was glued in a flip-chip configuration onto the cantilever paddle in such a way that the

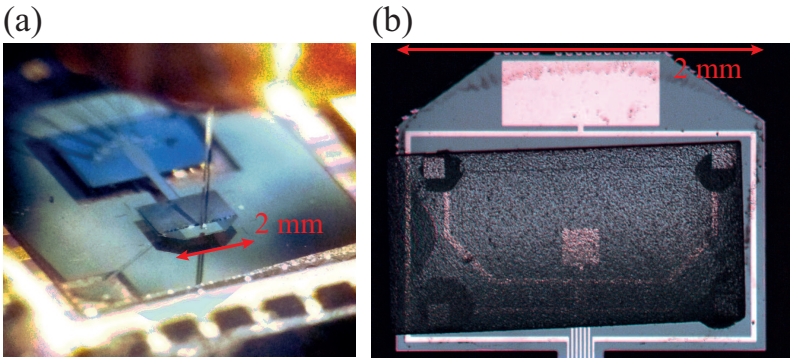

Figure 5.5: (a) Photographical in-situ image of GaAs-based cantilever mounted in the sample head with fiber-optical readout. Besides the GaAs cantilever, the optical fiber is visible. Image courtesy of F. Herzog (group of the present author). (b) Photographical image of the paddle of a GaAs-based cantilever with an attached MgZnO/ZnO sample for simultaneous measurement of electric transport and magnetization.

contacts on the sample match the corresponding contacts on the cantilever. For this, a conductive two-component glue was applied at the contact positions. The glue dots can bee seen in the image. Although the de Haas-van Alphen effect of a similar MgZnO/ZnO system had been measured with the capacitive readout scheme [104], the experiment with optical readout did not yield an oscillatory torque signal. This can probably be attributed to heating of the electron system caused by the laser light used for the readout, which suppresses the dHvA oscillations. However, in the group of the author there is ongoing experimental work to repeat this experiment with an optimized technique, which requires considerably less laser power. A success of this effort would enable the observation of the dHvA effect in the MgZnO/ZnO system using optical readout and thus open the way to new experiments with this intriguing material.

6 Materials and samples

In this chapter, we introduce the materials and the specific samples which have been investigated in this thesis. The examined materials are two representatives from the isostructural series of transition metal diborides, more specifically, VB_2 and MnB_2. In Sec. 6.1, the crystal structure of transition metal diborides as well as electronic properties common to this isostructural series are presented. This is followed by brief reviews of the specific electronic and magnetic properties of VB_2 in Sec. 6.2 and of MnB_2 in Sec. 6.3.

6.1 Transition metal diborides

Transition metal diborides $M B_2$ (where M is a transition metal) have attracted a long-standing interest as promising candidates for technical applications due to their high chemical inertness, mechanical robustness, resistivity against corrosion, high melting points, hardness, and good thermal and electrical conductivity [105–109]. They also provide an interesting object of investigation of how electronic and magnetic properties evolve with atomic number as one moves through the rows of transition metals in the periodic table while the crystal structure of the compounds remains unaltered. The discovery of the superconducting transition in MgB_2 at T_c = 39 K, being the highest transition temperature known in metallic superconductors [16, 110], has sparked additional interest in the transition metal diborides due to their isostructural composition with MgB_2.
Transition metal diborides $M B_2$ crystallize in the $C32$ (AlB_2) structure with the spacegroup $P6/mmm$. The $C32$ structure is depicted in Fig. 6.1. It consists of an alternating sequence of layers of closest-packed M atoms and layers of B atoms in a honeycomb lattice stacked in $[001]/c$-direction. Planes parallel to the B honeycomb layers and the hexagonal M hexagonal layers are sometimes referred to as basal planes in this thesis. The boron sublattices are isostructural to graphene and any boron atom is centered above 3 M atoms. An M atom has 6 nearest M neighbors and 12 nearest B neighbors. There is one formula unit (f. u.) per primitive unit

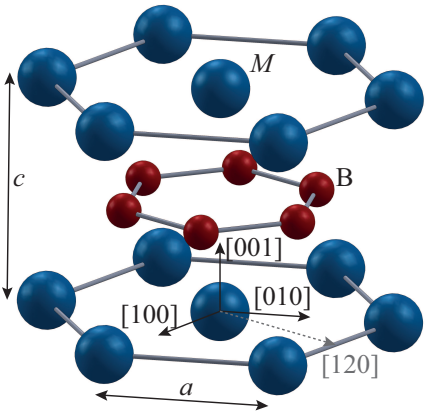

Figure 6.1: $C32$ crystal structure of transition metal (M) diborides MB_2. Closest-packed layers of M atoms and layers of B atoms in a honeycomb lattice alternate in $[001]/c$-direction.

cell. The distance between M layers is c and the distance between nearest M neighbors is a. Even though the crystal possesses a layered structure, the packing is dense and the interlayer bonding is relatively strong. The boron electron shells essentially hybridize to sp^2-orbitals forming strong intralayer σ-bonds and out-of-plane p_z-orbitals with a lower degree of localization bonding with d-electrons from the M layers.

Transition metal diborides share a range of common properties, but are also distinguished by profound differences. Among them is a remarkable variety of different magnetic ground states. While the diborides of the first three elements of the $3d$-row of transition metals have no magnetic order, for instance, the following compounds CrB_2 and MnB_2 show antiferromagnetic ordering [14, 111].

Considerable effort has been made to relate the common features of transition metal diborides as well as their differences to their electronic structure [12,13,112–117]. To gain insight into the nature of the chemical bonding in transition metal diborides and particularly into the electronic states at the Fermi energy E_F, studies of the diboride band structures and their density of states (DOS) have been performed employing different methodic approaches [113–115, 117]. In view of the experiments and calculations

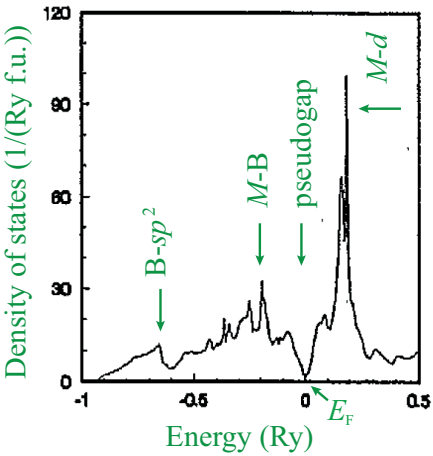

Figure 6.2: Typical density of states as a function of energy of transition metal (M) diborides $M\mathrm{B}_2$. Characteristic features of the DOS are a peak from sp^2-hybrid bonds in the B planes, another peak from M-B bonds, followed by a pseudogap in the proximity of the Fermi energy E_F. Above E_F a pronounced peak from localized M-d states is found. Figure taken from Ref. [114]. Green labels added by the present author.

presented in the following chapters, the widely accepted common characteristics of the DOS of transition metal diborides are briefly summarized as inferred from calculations without spin polarization. In Fig. 6.2, coming from negative energies (by convention, E_F is set to zero) a broadened peak reflects the sp^2-hybrid bonds of the boron planes, primarily consisting of B-2s and B-2p_{xy} atomic orbitals. Closer to E_F a second peak appears, which originates mostly from M-B bonding states, i. e. states with B-2p_z and M-3d character. This is followed by a pseudogap, a region of relatively low DOS. Beyond the pseudogap, a pronounced peak of localized M-3d states is found, which is followed by a series of anti-bonding states. When moving through the series of 3d-transition metals, the Fermi energy E_F approaches the 3d-peak of the DOS: For the first three elements of the series (Sc, Ti, and V), $n(E_\mathrm{F})$ is relatively low in the proximity of the pseu-

dogap. For the following elements Cr, Mn, and Fe[1], however, E_{F} resides in regions of high DOS. This suggests that the unpolarized state is unstable towards magnetic ordering [115].

6.2 Vanadium diboride

Vanadium diboride is the third representative of the class of $C32$ diborides in the $3d$-series of transition metals and the last in this series to be paramagnetic. Owing to this position, it has the highest value of $n(E_{\mathrm{F}})$ without magnetic ordering in this series. For this reason, it was revisited after the discovery of the superconducting state in MgB_2 as a potential candidate for superconductivity mostly in theoretical studies [116, 119, 120]. It seems worthwhile to examine VB_2 due to this property. Further, it can serve as a non-magnetic reference system for other diborides.
The VB_2 sample investigated in this thesis was provided by the group of Prof. Pfleiderer of Technische Universität München. It was grown by optical float-zoning [121]. Even though the very high melting temperature of 2750 K presented some problems for the growth process, nearly single-crystalline samples of VB_2 were obtained consisting of several grains with an orientation mismatch of a few degrees [121]. Details of the preparation procedure are given in Ref. [121]. The sample has a shape resembling a breadbox which was the result of rectangular cutting by a wiresaw while a rounded face stemming from the float-zoning process remained. It is depicted in Fig. 6.3 and had dimensions of $3.00 \times 2.00 \times 2.05\,\mathrm{mm}^3$ parallel to $[100]$, $[120]$, and $[001]$, respectively. The crystal orientations with respect to the perpendicular edges were established by Laue x-ray diffraction.

6.3 Manganese diboride

The compound MnB_2 follows CrB_2 and VB_2 in the isostructural series of the $3d$-transition metal diborides. Early studies of MnB_2 [122, 123] suggested weak ferromagnetism below T_{c} = 157 K/143 K with a saturation moment of $0.25\,\mu_{\mathrm{B}}$/f. u. and $0.19\,\mu_{\mathrm{B}}$/f. u., respectively. Subsequent measurements of electrical resistivity, magnetic susceptibility and anisotropy as well as nuclear magnetic resonance challenged this view in favor of

[1] FeB_2 is metastable in the Fe-B system [118], but its theoretical investigation is nevertheless instructive.

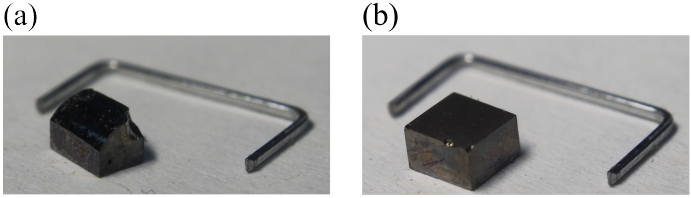

Figure 6.3: (a) Photographical image of the investigated VB_2 sample. It resembles a bread box with dimensions $3.00 \times 2.00 \times 2.05\,\mathrm{mm}^3$ parallel to $[100]$, $[120]$, and $[001]$, respectively. (b) Photographical image of the investigated MnB_2 sample. It has a cuboid shape with dimensions of $2.7 \times 2.8 \times 1.7\,\mathrm{mm}^3$ parallel to $[100]$, $[120]$, and $[001]$, respectively. Staples serve as a scale.

an antiferromagnetic order of in-plane magnetic moments localized at the Mn sites [14, 124]. Below the Néel temperature of $T_\mathrm{N} = 760\,\mathrm{K}$, an antiferromagnetic coupling of consecutive Mn planes was proposed while the moments within a single plane are aligned parallel with a moment of $3\,\mu_\mathrm{B}/\mathrm{f.u.}$ This state will be referred to as AF-c state in this thesis. The small experimental ferromagnetic component below T_c was attributed to a slight out-of-plane canting of the AF-c ordered moments at the Mn sites towards the c-axis. The essentially antiferromagnetic order was confirmed by neutron diffraction experiments of MnB_2 [125] stating an in-plane magnetic moment of $2.6\,\mu_\mathrm{B}/\mathrm{f.u.}$ Most theoretical surveys of the electronic properties of transition metal diborides merely suggested that MnB_2 is prone to itinerant magnetism [109, 115]. Only recently, the specific magnetism of MnB_2 attracted attention of theoretical approaches [126, 127]. It was shown that the AF-c order of local moments is energetically favorable over ferromagnetic order and that the canted AF-c structure is possible under both energetic as well as symmetry considerations. In accordance with the experimental findings, an itinerant character of the MnB_2 magnetism is disputed by these calculations in favor of an essentially localized Mn magnetism in MnB_2 [127]. At the same time, MnB_2 is presumed to be an example of Kübler's covalent magnetism [128] in that the DOS cannot be described with a rigid-shift behavior in the antiferromagnetic state due to the effects of covalent magnetism.

The MnB_2 sample investigated in this thesis was provided by the group of Prof. Pfleiderer of Technische Universität München. Similar to the VB_2 sample, it was grown by optical float-zoning. The sample is supposed to be the first large single crystal of MnB_2 [121]. Earlier experiments were primarily performed on sintered polycristalline samples that suffered from admixtures of MnB_4 and Mn_3B_4. The sample is depicted in Fig. 6.3. It has a cuboid shape with dimensions of $2.7 \times 2.8 \times 1.7\,\mathrm{mm}^3$ parallel to $[100]$, $[120]$, and $[001]$, respectively. Measurements of specific heat, susceptibility, and magnetization showed a smooth crossover below $\sim 130\,\mathrm{K}$ from the pure AF-c sate into the canted state [121]. For details of these measurements as well as the preparation, the reader is referred to Ref. [121].

We note that CrB_2 was the object of investigation of a previous study similar to this thesis [12, 13]. The compound CrB_2, being located between VB_2 and MnB_2, represents the onset of magnetic ordering in this isostructural series and an example of weak itinerant antiferromagnetism [111, 129, 130]. In contrast to the AF-c ordering of MnB_2, a cycloidal magnetic structure below $T_\mathrm{N} \approx 88\,\mathrm{K}$ with an ordering wave vector $\mathbf{q} = 0.285\,\mathbf{q}_{110}$ and $q_{110} = 2\pi/\frac{a}{2}$ was established [15,112]. Fermi surface properties inferred from dHvA measurements were found to be consistent with this ordering [12].

In summary, the series of VB_2, CrB_2, and MnB_2 presents an interesting example of the transition of $C32$ isostructural compounds from paramagnetism over weak itinerant antiferromagnetism to an interlayer antiferromagnetic coupling of localized moments.

Apart from Ref. [12], there are few studies which directly probe the Fermi surface properties of transition metal diborides by means of the dHvA effect and thus provide a test of the electronic structure calculations. For VB_2 pulsed field experiments for two selected field orientations have been reported [131]. Pluzhnikov et al. performed temperature-dependent dHvA measurements using the modulation technique on first row transition metal ScB_2, ZrB_2 from the second row, and HfB_2 from the third row [132] after general Fermi surface properties of ZrB_2 and HfB_2 had already been established in Ref. [133] and Ref. [134], respectively. For TiB_2, Tanaka et al. performed modulation technique measurements [135].
To the best of our knowledge, there are no studies of the dHvA effect in

MnB_2 previous to ours presented in this thesis.

7 De Haas-van Alphen effect and Fermi surface properties of VB_2

In this chapter the de Haas-van Alphen (dHvA) effect of nearly single crystalline VB_2 is investigated in order to derive Fermi surface properties of VB_2. The dHvA effect is derived from the quantum oscillatory component of the torque measured by cantilever magnetometry.
The chapter is organized as follows: The general experimental procedure is briefly explained in Sec. 7.1. Experimental results of the angular, temperature, and field dependence of the dHvA effect are presented and analyzed in Sec. 7.2-7.5. This is followed by a presentation and analysis of results of band structure calculations in Sec. 7.6-7.7 before turning to a comparison of the experimental findings and the calculations in Sec. 7.8.

7.1 Experimental procedure

For the magnetization measurements, the VB_2 sample, details of which have been described in Ch. 6, was attached to a double beam CuBe cantilever described in Sec. 3.2. The cantilever was mounted on a rotary stage attached to the cold head of a vacuum loading ^{3}He insert, which allowed for measurements between 0.28 K and 20 K. The ^{3}He insert was operated in a superconducting, axial 15 T-magnet. The capacitive readout technique introduced in Sec. 3.3 was used to determine the magnetic torque. Angle-dependent measurements were performed at the base temperature of $\sim$ 280 mK in magnetic fields of up to 15 T and temperature-dependent measurements were performed between 280 mK and 20 K. In order to find a compromise between time constraints on the one hand and an adequate resolution and the reduction of inductive heating on the other hand, magnetic sweep rates were varied between 0.3 T/min and 0.0025 T/min. For example, a typical run would consist of a relatively fast scan of the complete field range with 0.1 T/min and a slow scan for 12-15 T with 0.01 T/min. The angle of applied magnetic field $\mathbf{B}$ relative to the sample was varied in all three major planes of the $C32$ crystal structure. Figure 7.1 shows the

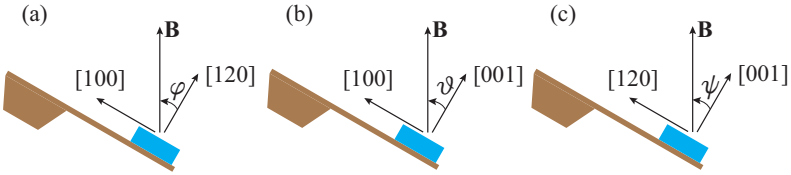

Figure 7.1: Side view of a CuBe cantilever with the VB_2 sample attached to it. The orientation of the magnetic field $\mathbf{B}$ was varied in all three major planes. Figures (a), (b), and (c) illustrate the denotation, where φ represents the angle of $\mathbf{B}$ in the basal plane relative to the $[120]$-axis while ϑ and ψ represent the azimutal angles relative to the c-axis for measurements with $\mathbf{B}$ in the $[001]$-$[100]$- and the $[001]$-$[120]$-plane, respectively.

different orientations of the crystal relative to the applied field. We denote the three corresponding angles by φ, ϑ, and ψ, where φ represents the angle in the basal plane relative to the $[120]$-axis while ϑ and ψ represent the azimutal angles relative to the c-axis for measurements in the $[001]$-$[100]$- and the $[001]$-$[120]$-plane, respectively. For φ amd ϑ, the angle was varied in increments of $7.5°$ while for ψ the increment was $10°$.

7.2 Experimental findings

Typical experimental data are illustrated in Fig. 7.2, where the torque Γ is plotted versus magnetic field strength $B = |\mathbf{B}|$ in every subfigure. Figures 7.2 (a) and (c) show raw data for the basal plane (angle φ) and the $[001]$-$[100]$-plane (angle ϑ), respectively. The change in capacitance has been translated into torque via the calibration scheme outlined in Sec. 3.4. Exemplary data for the $[001]$-$[120]$-plane (angle ψ) are very similar to ϑ-data and are therefore not shown for the sake of brevity. Figures 7.2 (b) and (d) show the oscillatory part Γ_{osc} of Γ after subtraction of the non-oscillatory background of the torque signal for different values of φ and ϑ. Curves are vertically offset for clarity. In order to eliminate the non-oscillatory signal part, a low-order polynomial was fitted to the raw data in B and then subtracted. The resulting data were then taken in $1/B$ and another low-order polynomial was subtracted if deemed necessary to further reduce the background.
For each rotational plane, one dHvA frequency is found. Each dHvA fre-

quency corresponds to an extremal orbit perpendicular to the given magnetic field $\mathbf{B}$ via the Lifshitz-Onsager relation Eq. 2.16. The frequency in the basal plane is on the order of 1.4 kT and denoted as f_α (with α being the corresponding extremal orbit), while the frequency f_β of orbit β for the ϑ-plane (and also the ψ-plane) is ~ 100-200 T. Figure 7.2 (a) shows data for $\varphi = -7.5°$ where f_α is visible in the raw data. As can be inferred from Fig. 7.2 (b), the amplitude of Γ_{osc} varies for different angles φ. Its maximal value in the accessible field range ≤ 15 T of $\sim 1 \cdot 10^{-10}$ Nm is adopted for $\varphi = -7.5°$ while it almost vanishes for $\varphi = -30°$, where it is as small as $1 \cdot 10^{-11}$ Nm. For other angles intermediate values are observed. In a likewise fashion, Fig. 7.2 (c) shows raw data for $\vartheta = -15°$, where the oscillatory part is maximal in the ϑ-plane. Figure 7.2 (d) shows the oscillatory part Γ_{osc} for four different values of ϑ. The amplitude of Γ_{osc} initially increases from $\vartheta = 0°$ to $\vartheta = -15°$, i. e. for $\mathbf{B}$ tilting away from the c-axis. For $\vartheta = -30°$ and $-45°$, it decreases again. We note that the amplitudes for the two observed dHvA frequencies f_α and f_β differ by roughly four orders of magnitude.

7.3 Angular dependence

As mentioned in Sec. 7.1, the orientation of $\mathbf{B}$ was varied in increments of 7.5° for φ and ϑ and 10° for ψ to study the angular dependence of the dHvA signals.

In the basal plane, the frequency f_α was traced over an angular range of 200°. For an exact determination of f_α, a fast Fourier transform (FFT) of the oscillatory part of the magnetization $M_{\mathrm{osc}} = \Gamma_{\mathrm{osc}}/B$ as a function of $1/B$ was analyzed for every angle φ. Figure 7.3 (a) shows the FFT spectrum for $\varphi = -7.5°$. Only one distinct frequency at $f_\alpha = 1385$ T is found. Magnetic field sweep rates and sampling rates were adjusted such that frequencies of up to ~ 15 kT could have been resolved if accessible within the limits of the experimental parameters, such as field strength and temperature. Figure 7.3 (b) depicts the evolution of f_α as a function of φ. A periodicity of 60° is supported by the data. The frequency f_α is maximal for $(n + 1/2) \cdot 60°$ ($n \in \mathbb{N}_0$), i. e. the $\langle 100 \rangle$-directions, at $f_\alpha(\langle 100 \rangle) \approx 1460$ T and minimal for $n \cdot 60°$, i. e. the $\langle 120 \rangle$-directions, at $f_\alpha(\langle 120 \rangle) \approx 1365$ T. We also note that the signal strength is maximal for $\varphi = -7.5°, 7.5°, 52.5°$ ... while the oscillation amplitude is minimal and barely detectable in the

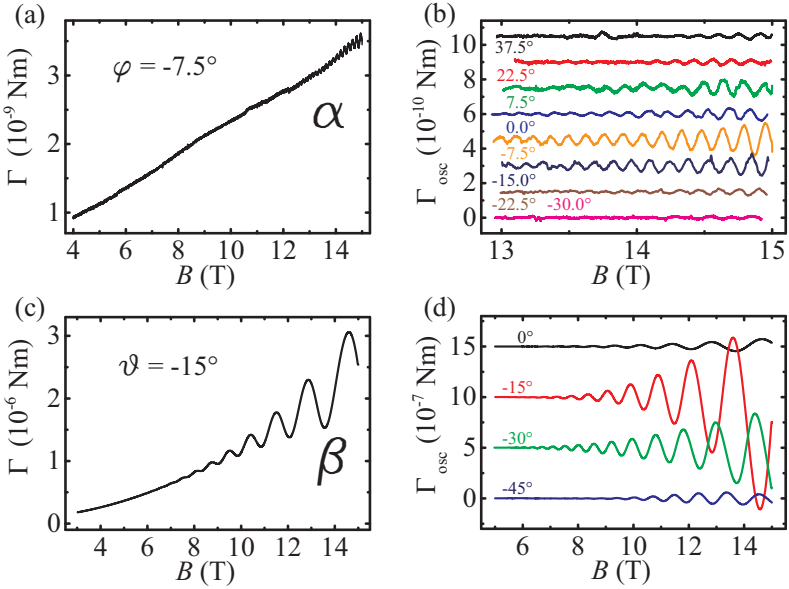

Figure 7.2: (a) Raw data of torque Γ for $\varphi = -7.5°$ in the basal plane. (b) Oscillatory component Γ_{osc} of Γ for different angles in the basal plane. (c) Raw data of torque Γ for $\vartheta = -15°$ in the [001]-[100]-plane. (d) Oscillatory component Γ_{osc} of Γ for different angles in the [001]-[100]-plane. The amplitudes of the two observed dHvA frequencies α and β differ by approximately four orders of magnitude.

proximity of the maximal value of f_α, i. e. for $\varphi \approx -30°$, 30°, and 90°. This fact is reflected in the size of the error bars in Fig. 7.3 (b). Also, the resolution for the period $0 \leq \varphi \leq 60°$ is better than for other values. This is a consequence of the orientation of the cantilever. For this period the paddle of the cantilever is oriented horizontally or points downward. It is found that this generally results in a better resolution than for the cantilever pointing upwards or placed in an upside-down position.
Similarly, in the [001]-[100]-plane, the frequency f_β was traced over an angular range of 270° and FFT spectra were calculated for every angle ϑ. Figures 7.4 (a,c) illustrate the corresponding results. Figure 7.4 (c)

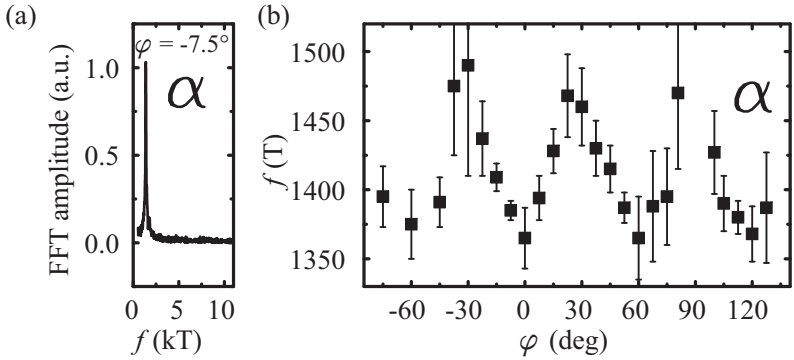

Figure 7.3: Experimental results for rotation of $\mathbf{B}$ in the basal plane. (a) Fast Fourier transform of $M_{\mathrm{osc}}(1/B)$ at $\varphi = -7.5°$ revealing one orbit α with frequency $f_\alpha = 1385\,\mathrm{T}$. (b) Angular dependence of f_α for $-75° \leq \varphi \leq 127.5°$. The orbit features a 60° periodicity.

shows four FFT spectra corresponding to the torque data of Fig. 7.2 (d). When tilting $\mathbf{B}$ away from the c-axis, the frequency f_β increases. We also recover the evolution of the signal strength described in Sec. 7.2 in the FFTs: The signal strength increases from 0° to −15° and decreases for −30° and −45°. Figure 7.4 (a) illustrates the evolution of f_β in the $[001]$-$[100]$-plane. A 180° periodicity is observed. Frequency f_β is minimal along the c-axis where $f_\beta = 102\,\mathrm{T}$. When $\mathbf{B}$ tilts away from the c-axis, f_β increases adopting large values of $f_\beta(-52.5°) = 188\,\mathrm{T}$, $f_\beta(50°) = 166\,\mathrm{T}$, and $f_\beta(130°) = 183\,\mathrm{T}$. For $50° < \vartheta < 130°$, f_β was not observed.
In the $[001]$-$[120]$-plane, measurements were performed for $0° \leq \psi \leq 90°$ in increments of 10°. A dHvA frequency $f_{\beta'}$ belonging to an orbit β' is observed for $0° \leq \psi \leq 50°$. The angular dependence of $f_{\beta'}$ is depicted in Fig. 7.4 (b). The tendency $f_{\beta'}(\psi)$ is similar to $f_\beta(\vartheta)$ in Fig. 7.4 (a) with $f_{\beta'}$ slightly exceeding f_β for larger angles.
The 60° periodicity of α is consistent with the six-fold symmetry of the crystal in the hexagonal plane. Since α exhibits a non-zero signal strength for a full period (and more), it can be concluded that it stems from a closed sheet of the Fermi surface. As f_α varies only by about 7%, the corresponding surface sheet has a nearly constant area for cross sections perpendicular

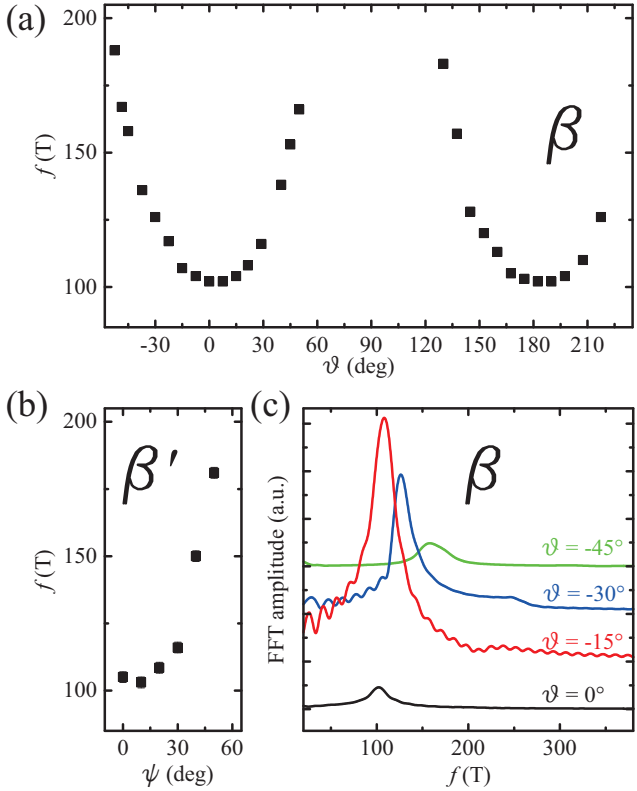

Figure 7.4: Experimental results for rotations of $\mathbf{B}$ in the [001]-[100]-plane and the [001]-[120]-plane. (a) Angular dependence of f_β for $-52.5° \leq \vartheta \leq 217.5°$. Measurements were taken in approximately equal increments. Orbit β was not observed for $\vartheta \leq -60°$ and $57.5° \leq \vartheta \leq 122.5°$. (b) Angular dependence of $f_{\beta'}$ for $0° \leq \psi \leq 50°$. Orbit β' was not observed for $60° \leq \psi \leq 90°$. (c) Fast Fourier transforms of $M_{\mathrm{osc}}(1/B)$ for four different angles ϑ corresponding to the data in Fig. 7.2 (d) showing orbit β shifting to higher frequencies for $\mathbf{B}$ tilting away from the c-axis

to the hexagonal plane.
To explain the variation of the signal strength $\Gamma = M_\perp \cdot B$, we recall that the component of the magnetization $M_{\perp,i}^{\mathrm{osc}} = -\frac{1}{f} \cdot \frac{\partial f}{\partial \theta_i} M_\parallel^{\mathrm{osc}}$ depends on the so-called anisotropy factor $1/f \cdot \partial f/\partial \theta_i$, being the logarithmic derivative of the dHvA frequency with respect to θ_i (cf. Eqs. 2.29 and 2.30 and Fig. 2.2). Hereby, the angle θ_i measures the orientation of $\mathbf{B}$ in the plane of $\mathbf{B}$ and the considered component $M_{\perp,i}^{\mathrm{osc}}$. Furthermore, in Sec. 3.3 it was shown that only the bending torque component Γ_t, associated with the perpendicular magnetization component $M_{\perp,y}$ inside the plane spanned by the cantilever beam and the direction of the field $\mathbf{B}$ (Fig. 3.1), has a substantial coupling to the measurement signal. Therefore, we can deduce that the relevant angle θ_i for the derivative in the anisotropy term is identical to the respective experimental angle defined in Fig. 7.1. This insight will be important for the further discussion of the experimental results. We henceforth only state the anisotropy term with the respective experimental angle for the derivative, e. g. for the rotation of $\mathbf{B}$ in the basal plane the anisotropy term is $1/f \cdot \partial f/\partial \varphi$. It is plausible that Γ_osc is reduced in the $\langle 100 \rangle$- and $\langle 120 \rangle$-directions as the anisotropy term of high-symmetry directions should ideally vanish.
Also, it is worthwhile to note that $M_\parallel^{\mathrm{osc}}$ in turn (and hence $M_\perp^{\mathrm{osc}}$ as well) scale with $1/\sqrt{A''}$ where A'' is the curvature of the extremal area of the Fermi surface in the direction of $\mathbf{B}$. From the data, it can also be inferred that either the anisotropy for $\langle 100 \rangle$ is smaller than for $\langle 120 \rangle$ or the curvature along $\langle 100 \rangle$ is larger or a combination thereof as the signal strength is higher for the minima of f_α (along $\langle 120 \rangle$) than for the maxima of f_α (along $\langle 100 \rangle$).
In the $[001]$-$[100]$-plane, the $180°$ periodicity of f_β is also consistent with the crystal symmetry. In contrast to f_α however, f_β disappears for certain field directions indicating that β belongs to an open Fermi sheet. The exceptionally high signal strength hints to a very low curvature and/or a large anisotropy $1/f \cdot \partial f/\partial \vartheta$, i. e. the sheet should locally resemble an elongated, cylindrical shape along the c-direction.
For orbit β' we assume the same origin in the Fermi surface as for orbit β due to their close similarity in angular frequency dependence. In fact, as both constellation $\vartheta = 0°$ and constellation $\psi = 0°$ coincide with $\mathbf{B}$ parallel to the c-axis, f_β and $f_{\beta'}$ should be identical for these angles, which is fulfilled. For this reason, we henceforth identify β' with β.

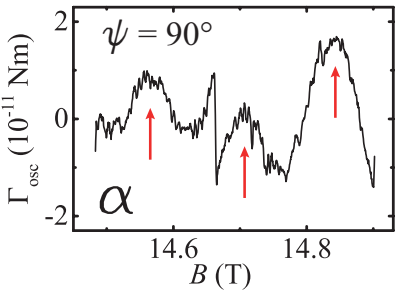

Figure 7.5: Signature of orbit α for a rotation of $\mathbf{B}$ in the $[001]$-$[120]$-plane at $\psi = 90°$, i. e. the coincidence angle with $\varphi = 0°$. The jump of Γ_{osc} at $B = 14.66\,\mathrm{T}$ is caused by measurement artifacts. Two periods of the dHvA oscillation can be resolved with the three maxima indicated by red arrows.

Since we inferred that α stems from a closed Fermi sheet, its absence in the experiments in the $[001]$-$[100]$- and the $[001]$-$[120]$-plane must be explained. We attribute its absence to two reasons: (1) As noted in Sec. 7.2, the observed signals for $\mathbf{B}$ inside and outside the basal plane differ by four orders of magnitudes. If it is assumed that M_{osc} for α is on a similar scale outside and inside the basal plane, the effective sensitivity of the capacitance bridge employed in the experiments is not sufficient to resolve both f_α and f_β at the same time, as explained in Sec. 3.5. (2) Explanation (1) cannot hold for $\vartheta, \psi \approx 90°$, i. e. in the proximity of the basal plane, where β is not observed. Although $\vartheta = 90°$ coincides with $\varphi = 30°$ and $\psi = 90°$ conincides with $\varphi = 0°$, the resulting torques can however greatly differ due to the different anisotropy factors $1/f \cdot \partial f/\partial\varphi$, $1/f \cdot \partial f/\partial\vartheta$, and $1/f \cdot \partial f/\partial\psi$ for the different constellations. We thus assume that the anisotropy of the α-sheet for $\mathbf{B}$ varied within the basal plane is larger than for $\mathbf{B}$ passing through the basal plane. We mention that signatures of α were found in some measurements with $\mathbf{B}$ in the proximity of the basal plane, i. e. for ϑ or ψ, respectively, close to $90°$. Figure 7.5 illustrates exemplary data. The data quality, however, does not support a detailed quantitative analysis.

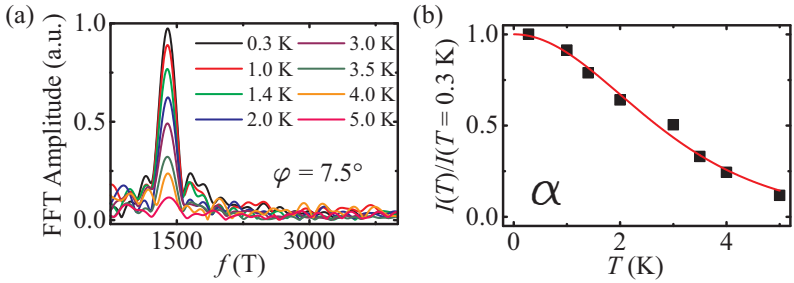

Figure 7.6: Temperature dependence of orbit α. (a) Temperature-dependent fast Fourier transforms of $M_{\mathrm{osc}}(1/B)$ at $\varphi = 7.5°$ for $T = 0.3\,\mathrm{K}, 1.0\,\mathrm{K}, 1.4\,\mathrm{K}, 2.0\,\mathrm{K}, 3.0\,\mathrm{K}, 3.5\,\mathrm{K}, 4.0\,\mathrm{K}$, and $5.0\,\mathrm{K}$. (b) Normalized FFT amplitudes $I(T)$ corresponding to the data in Fig. (a) (points) and fit of Eq. 7.1 (red line) to the data points as a function of temperature. The fit reveals an effective mass of $m^{\star}_{\alpha} = (0.79 \pm 0.03)\, m_{\mathrm{e}}$.

7.4 Temperature dependence

The temperature dependence of $M_{\mathrm{osc}} = \Gamma_{\mathrm{osc}}/B$ for both orbit α and orbit β was studied for one fixed angle φ and ϑ, respectively.
For orbit α, $\varphi = 7.5°$ was chosen as this orientation yields the strongest signal. Figure 7.6 (a) shows FFT spectra for temperatures T ranging from $0.3\,\mathrm{K}$ to $5.0\,\mathrm{K}$. The FFT spectra base on $M_{\mathrm{osc}}(1/B)$ limited to the field range between $13.75\,\mathrm{T}$ and $15\,\mathrm{T}$. The peak of α at $f_{\alpha} = 1390\,\mathrm{T}$ decays for increasing temperature, vanishing almost completely for $T = 5.0\,\mathrm{K}$.
According to the Lifshitz-Kosevich formula (Eq. 2.39), the temperature dependence of the dHvA amplitude at constant field $\mathbf{B}$ can be related to the effective electron mass $m^{\star}$ of the corresponding band and at corresponding K-space coordinates via the reduction factor

$$R_{\mathrm{T}} = \frac{X}{\sinh X}, \quad \text{with} \quad X = \frac{2\pi^2 k_{\mathrm{B}} m^{\star} T}{\hbar e B}. \tag{7.1}$$

Equation 7.1 was fitted to the normalized temperature-dependent peak heights $I(T)/I(T = 0.3\,\mathrm{K})$ extracted from the FFTs of Fig. 7.6 (a). For B the arithmetic mean of the analyzed field range $\bar{B} = 14.375\,\mathrm{T}$ was inserted and

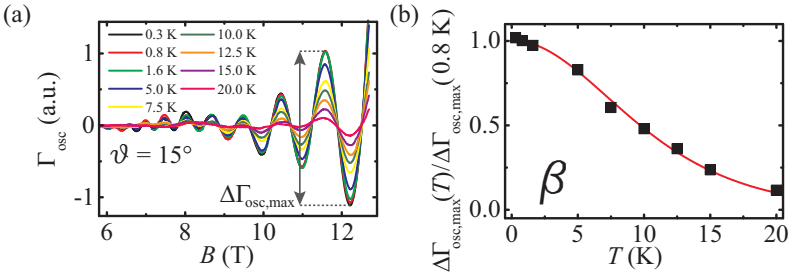

Figure 7.7: Temperature dependence of orbit β. (a) Temperature-dependent oscillatory torque $\Gamma_{\mathrm{osc}}(B)$ at $\vartheta = 15°$ for $T = 0.3\,\mathrm{K}$, $0.8\,\mathrm{K}$, $1.6\,\mathrm{K}$, $5.0\,\mathrm{K}$, $7.5\,\mathrm{K}$, $10.0\,\mathrm{K}$, $12.5\,\mathrm{K}$, $15.0\,\mathrm{K}$, and $20.0\,\mathrm{K}$. (b) Normalized amplitude of "last" oscillation period $\Delta\Gamma_{\mathrm{osc,max}}(T)$ corresponding to the data in Fig. (a) (points) and fit of Eq. 7.1 (red line) to the data points as a function of temperature. The fit reveals an effective mass of $m^{\star}_{\beta} = (0.182 \pm 0.004)\,m_{\mathrm{e}}$.

$m^{\star}$ and a multiplicative constant were used as free fit parameters. The extracted data (points) as well as the fitted reduction factor (line) are depicted in Fig. 7.6 (b). The fit yields $m^{\star}_{\alpha} = (0.79 \pm 0.03)\,m_{\mathrm{e}}$.
Similarly, for β the temperature was varied between $0.3\,\mathrm{K}$ and $20\,\mathrm{K}$ at fixed angle $\vartheta = 15°$. Figure 7.7 (a) depicts data Γ_{osc} versus magnetic field B. However, in contrast to the analysis for α, the amplitude data in Fig. 7.7 (b) is not based on FFTs over a finite field range, but corresponds to the amplitude of only the last observed oscillation period (i. e. at maximal field) $\Delta\Gamma_{\mathrm{osc,max}}(T)$. Because of the low value of f_{β}, this method is expected to yield a more accurate result since Eq. 7.1 depends on the field strength B and the full Lifshitz-Kosevich formula Eq. 2.39 contains an additional field-dependent reduction factor R_{D}. The fit of Eq. 7.1 yields a small effective mass of $m^{\star}_{\beta} = (0.182 \pm 0.004)\,m_{\mathrm{e}}$.

7.5 Field dependence

While the dependence of M_{osc} on temperature T at fixed field B yields the effective mass (Sec. 7.4), study of the dependence on B at fixed T can provide the mean free path of the respective charge carriers. For this, we consider the Lifshitz-Kosevich formula for Γ_{osc} restricted to the first harmonics of the dHvA frequencies,

$$\Gamma_{\mathrm{osc}} = \sum_{i\in\{\alpha,\beta,\dots\}} C_i^0 \cdot B^{\frac{3}{2}} \underbrace{\exp\left(-\frac{\pi m_{\mathrm{b},i}}{eB\tau}\right)}_{R_{\mathrm{D},i}} \underbrace{\frac{X_i}{\sinh X_i}}_{R_{\mathrm{T},i}} \sin\left(\frac{2\pi f_i}{B} + \phi_i\right), \quad (7.2)$$

where the sum runs over all orbits $\{\alpha, \beta, \dots\}$, $R_{\mathrm{D},i}$ is the Dingle reduction factor with $m_{\mathrm{b},i}$ being the band mass of the respective orbit and τ being the scattering time, $X_i = (2\pi^2 k_{\mathrm{B}} m_i^\star T)/(\hbar e B)$ is defined as in Sec. 7.4, ϕ_i accounts for phase differences of the contributing frequencies f_i, and C_i^0 are prefactors weighting the contributions. As we do not observe more than one dHvA frequency simultaneously, the sum collapses to just one summand and we can use C_α^0 (C_β^0), $m_{\mathrm{b},\alpha}/\tau$ ($m_{\mathrm{b},\beta}/\tau$), and ϕ_α (ϕ_β) as free fit parameters while we use f_α (f_β) and $m_\alpha^\star$ ($m_\beta^\star$) as obtained in the previous sections. Figure 7.8 (a,b) show Γ_{osc} of α for $\varphi = -7.5°$ and Γ_{osc} of β for $\vartheta = 15°$, respectively (black lines). The red lines depict the Lifshitz-Kosevich formula Eq. 7.2 fitted to the data. Assuming free electrons, m_{b}/τ can be replaced by $\hbar k_{\mathrm{F}}/l$ in Eq. 7.2 with l being the mean free path. Here, k_{F} denotes the Fermi wave vector. Following Refs. [136, 137], we further set $\pi k_{\mathrm{F}}^2 = 2\pi e f/\hbar$, which implies the approximation that frequency f stems from a circular orbit on the Fermi surface. Applying these approximations, the fits yield $l_\alpha = 25\,\mathrm{nm}$ and $l_\beta = 21\,\mathrm{nm}$ for the mean free paths.

7.6 Band structure and Fermi surface

Band structure calculations for VB_2 were performed by J. Kuneš[1]. The local density approximation of density functional theory using the full-potential linearized augmented plane-wave method implemented in the

[1] Institute of Physics, Academy of Sciences, Cukrovarnicka 10, Praha 6 16253, Czech Republic

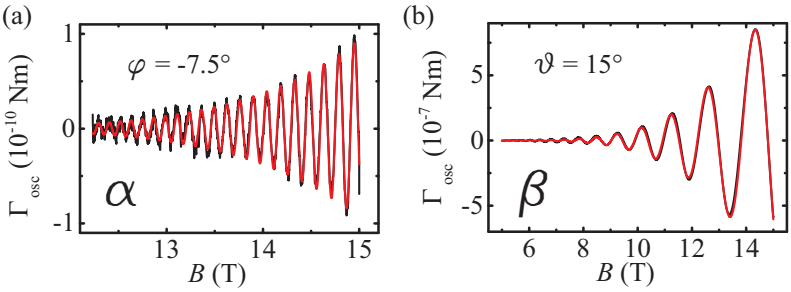

Figure 7.8: Field dependence of orbit α and β. (a) Γ_{osc} for α at $\varphi = -7.5°$ as a function of field strength B (black line). The red line is a fit of Eq. 7.2 to the data using f_α and $m^\star_\alpha$ as determined in the previous sections. It yields the free mean path $l_\alpha = 25\,\mathrm{nm}$. (b) $\Gamma_{\mathrm{osc}}(B)$ for β at $\vartheta = 15°$ (black line). The fit of Eq. 7.2 (red line) to the data using f_β and $m^\star_\beta$ as determined above yields the free mean path $l_\beta = 21\,\mathrm{nm}$.

WIEN2k package was applied [138–140]. The 90 K lattice constants $a = 2.998\,\text{Å}$ and $c = 3.044\,\text{Å}$ from Ref. [131] were used. Figure 7.9 depicts the band structure along high-symmetry directions of the Brillouin zone. The results are similar to previous calculations [116, 119, 120, 131]. We revisited such calculations as we will use the data to extract dHvA effect frequencies f_i in the following. We aim at identifying relevant Fermi surface cross sections. In total, three bands highlighted in blue, green, and red cross the Fermi Energy E_{F}. In the following, we refer to them as band 10, 11, and 12, respectively[1]. The density of states $n(E)$ (DOS), normalized to one formula unit (f. u.), i. e. per one V atom and two B atoms, as a function of energy E as derived from the calculated band structure is shown in Fig. 7.10. In Fig. 7.10, contributions to the DOS originating from B-$2s$ orbitals, B-$2p$ orbitals, and V-$3d$ orbitals are illustrated separately, and additionally the total density of states is shown. The typical DOS of non-magnetic transition metal diborides (as discussed in Sec. 6.1) is recovered.

[1] The numbering of the bands is adopted from the WIEN2k results. The WIEN2k calculations were performed for 21 electrons/f. u., neglecting the deeply bound core electrons $[\mathrm{Ne}]\,3s^2$ at the V sites. Taking spin degeneracy into account, this explains that E_{F} resides approximately centered between band 10 and 11 as in Fig. 7.9. Apart from that, the numbering can be regarded as purely conventional.

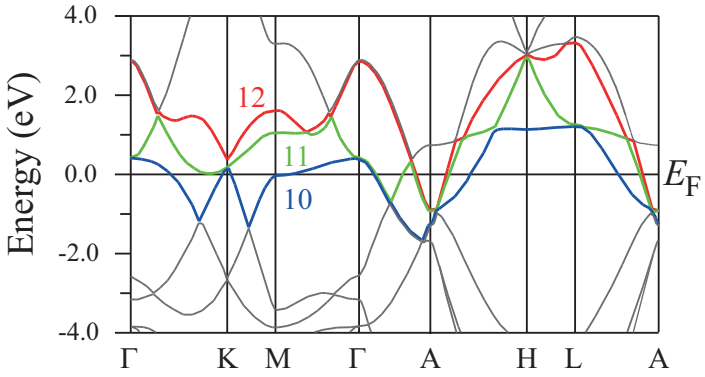

Figure 7.9: Calculated band structure of VB_2 using the WIEN2k package along high-symmetry directions of K-space. Three bands (blue, green, red) cross E_F, denoted as band 10, 11, and 12.

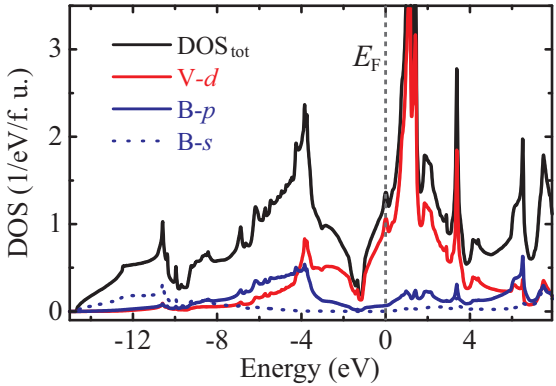

Figure 7.10: Density of states (DOS) of VB_2 per formula unit (f. u.) as inferred from the calculated band structure. The total DOS is shown and additionally the contributions from B-2s, B-2p, and V-3d states are drawn separately. The typical DOS of non-magnetic transition metal diborides (as discussed in Sec. 6.1) is recovered. The Fermi energy E_F, by convention set to $E_F = 0$, resides at the left flank of the V-d peak. The states at E_F are dominated by V-d components with an admixture of B-p orbitals.

The Fermi energy E_F, by convention set to $E_\mathrm{F} = 0$, resides on the left flank of the V-d peak. The DOS for VB_2 is very similar to the DOS for hypothetically non-magnetic CrB_2, which has been discussed in Ref. [71]. The main difference between the two DOS arises from the additional electron in CrB_2, which makes the Fermi energy move even closer to the d-peak in CrB_2 and consequently causes the itinerant antiferromagnetism found in CrB_2 in contrast to VB_2. From Fig. 7.10, it can also be deduced that the character of the bands around E_F is dominated by V-d orbitals with only a small admixture of the B-p DOS. In more detail, it can furthermore be inferred from the band structure calculations that the B-p component at E_F mainly consists of B-p_{xy} contributions. The B-p_z states are pushed away from E_F. Corresponding fat bond plots, indicating B-p_{xy}, B-p_z, and V-d contributions to the bands separately, can be found in App. A. As argued in App. A, the character of the states at E_F can in summary be described as V-d with a varying degree of B-p_{xy} contributions depending on band index and K-space direction. A further treatment of the nature of the electronic states at E_F is postponed to a comparative discussion of the experimental results for VB_2 along with the isostructural compounds MnB_2, CrB_2, and MgB_2 in section 8.9.

Figures 7.11 (a-c) depict the three sheets of the Fermi surface in the Brillouin zone corresponding to the three bands 10, 11, and 12, which cross E_F. For clarity, they are drawn separately. In accordance with the numbering of their associated bands, we denote them by sheet 10, 11, and 12, respectively. Figure 7.11 (d) illustrates the real space geometry with the experimental angles φ, ϑ, and ψ. Note that for the hexagonal lattice the Brillouin zone is oriented parallel to the real space (Bravais) unit cell, i. e. the real space direction $\langle 100 \rangle$ is parallel to the connecting line of Γ and K and the real space direction $\langle 120 \rangle$ is perpendicular to faces of the Brillouin zone. As a scale reference, we note that the equivalent areas of each face and the hexagonal plane of the Brillouin zone are $52\,\mathrm{kT}$ and $53\,\mathrm{kT}$, respectively. The blue sheet 10 in Fig. 7.11 (a) originates from (blue) band 10 in Fig. 7.9. It consists of a thick trunk parallel to the c-axis from which six roots extend toward the edges of the Brillouin zone both in the upper and the lower half of the zone. Close to the zone boundary, pairs of each one upper root and one lower root unite and then separate again into two branches that perpendicularly penetrate the faces. On every face two branches of two neighboring pairs of roots slightly merge at the M-point. The green sheet 11 in Fig. 7.11 (b) stems from the green band in Fig. 7.9.

It consists of an ellipsoidal electron pocket at A and two copies of another smaller electron pocket halfway between Γ and A with a tear drop-like form. Similarly, the red sheet 12 of Fig. 7.11 (c) originates from the red band in Fig. 7.9 and has a spherical shape centered at A, but it is smaller than the ellipsoid of the green sheet at the same position.

7.7 Extraction of dHvA frequencies

The SKEAF program (Supercell K-space Extremal Area Finder) [141] was employed to extract dHvA frequencies from the band energies calculated with WIEN2k. The tool allows for the calculation of extremal orbits and their corresponding dHvA frequencies for rotations of $\mathbf{B}$ in arbitrary planes. Additionally, it provides the corresponding band mass, sheet curvature, the type of the orbit (i. e. electron- or hole-like), and the average K-space coordinates. In order to compare the results directly with the experiment, we extracted extremal areas for rotations in the same planes as in Fig. 7.1. Figure 7.12 illustrates results for the basal plane. Figure 7.12 (a) shows dHvA frequencies versus angle φ for band 11 and 12, Fig. 7.12 (b) is a blow-up of Fig. 7.12 (a), Fig. 7.12 (c) depicts dHvA frequencies versus φ for band 10, and Fig. 7.12 (d) shows curvature data for the orbit of Fig. 7.12 (b). The three calculated orbits in Fig. 7.12 (a) have frequencies on the order of 1 kT. The two orbits illustrated by triangle symbols (△) stem from band 11. The orbit at ~ 1.9 kT belongs to the ellipsoid at A, the other orbit at ~ 1.35 kT originates from the tear drop-like pockets. The middle orbit depicted by diamond symbols (◇) originates from the sphere of sheet 12. The frequencies of the two orbits stemming from the pockets at A of band 11 and 12 vary very little with φ while the variation of the tear drop pocket frequency is more pronounced. From Fig. 7.12 (b) it can be inferred that this variation is approximately 40 T. As can be expected from the complicated form of the sheet in Fig. 7.11 (a), the dHvA spectrum of band 10 is richer than the one of band 11 and 12. DHvA Frequencies up to 40 kT were found by the SKEAF tool. In Fig. 7.12 (c) the frequencies up to 12.5 kT are illustrated. A complete assignment of all orbits to the corresponding features of the Fermi surface is omitted. As an example, we point out that the orbit at $\varphi = 0°$ and $f = 5.7$ kT stems from the two touching branches on the faces forming a dumbbell-like cross section.
In a similar fashion, Fig. 7.13 illustrates the SKEAF results for rotations

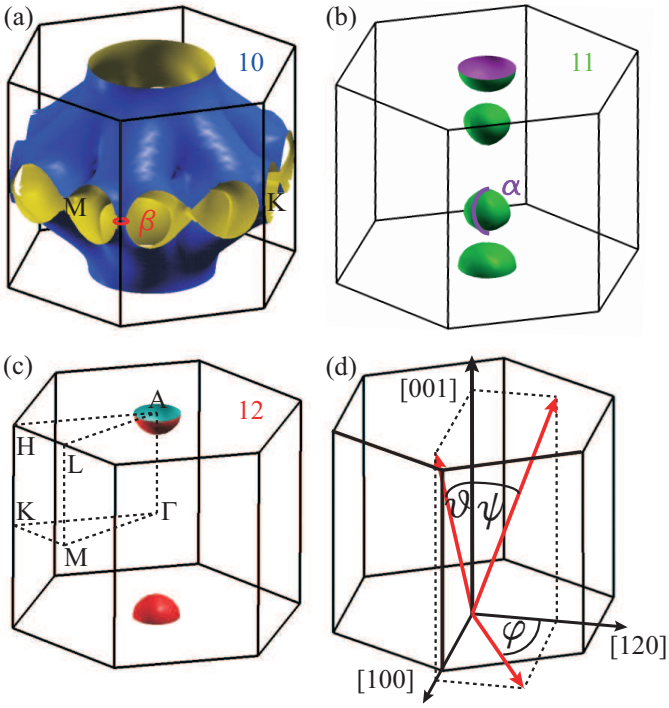

Figure 7.11: (a-c) Fermi surface sheets of the three bands crossing E_F depicted in the Brillouin zone. For clarity, they are drawn separately. (a) Sheet 10 consists of a trunk with a complicated root structure protruding from the trunk to the faces of the Brillouin zone. (b) Sheet 11 consists of ellipsoidal pockets at the A-points and two copies of a tear drop-like pocket halfway between Γ and A. (c) Sheet 12 consists of a nearly spherical pocket at A. The areas of the faces and the hexagonal plane of the Brillouin zone are equivalent to dHvA frequencies of 52 kT and 53 kT, respectively. (d) Real space coordinate system with the experimental angles φ, ϑ, and ψ. The Bravais unit cell is oriented parallel to the Brillouin zone of reciprocal space. The experimentally observed extremal orbits stem from small hole-like capillaries at the K-points of sheet 10 (orbit β, Fig. (a)) and the electron-like tear drop pockets of band 11 (orbit α, Fig. (b)).

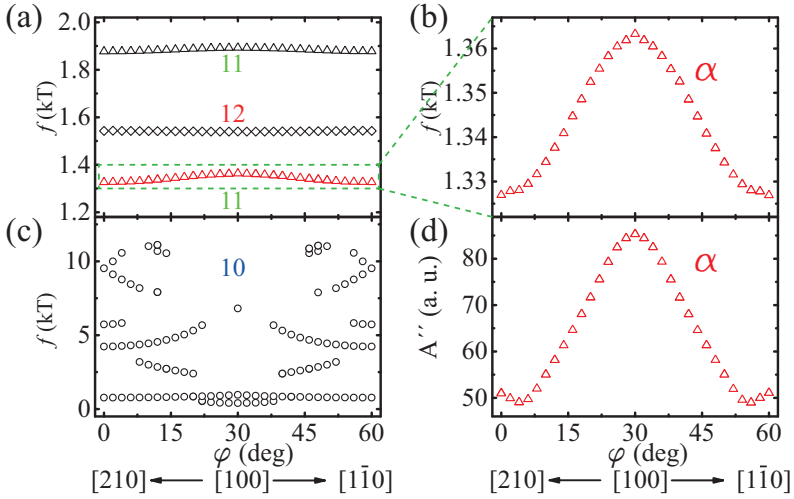

Figure 7.12: Angular dependence of dHvA frequencies and of curvature of extremal orbits versus angle φ for rotations of $\mathbf{B}$ in the basal plane as extracted from the band structure calculations using the SKEAF tool [141]. (a) Angular dependence of extremal orbits of band 11 and 12 corresponding to the surface sheets in Figs. 7.11 (b,c). Two orbits stemming from band 11 are depicted as triangles $\triangle$. The orbit from band 12 is represented by diamonds $\diamond$. The lowest orbit, highlighted in red, is shown in an magnified view in (b). The experimentally observed orbit α is assigned to this orbit stemming from the tear drop-like pockets of Fig. 7.11 (b). (c) Angular dependence of extremal orbits of band 10 corresponding to the surface sheet in Fig. 7.11 (a). Many orbits are found. Only frequencies below 12.5 kT are shown. (d) Angular dependence of curvature A'' along $\mathbf{B}$ of the extremal orbit in (b).

through the c-axis, i. e. for the experimental azimutal angles ϑ and ψ. The left column of subfigures (a,c,e) depicts orbit frequencies versus angle for the $[001]$-$[100]$-plane, i. e. angle ϑ while the right column (b,d,f) shows data for the $[001]$-$[120]$-plane, i. e. angle ψ. The first row of subfigures (a,b) again illustrates the orbits of band 11 (triangles $\triangle$) and 12 (diamonds $\diamond$). A very similar angular dependence for rotations over the edges (ϑ, Fig. 7.13(a)) and over the faces (ψ, Fig. 7.13 (b)) of the Brillouin zone is found. We recover the spherical, the ellipsoidal, and the tear drop-like pocket of the sheets in Figs. 7.11 (b,c) with the tear drop orbits having the lowest frequencies. All orbit frequencies feature a significant dependence on the azimutal angles with each of them having its maximum for $\mathbf{B}$ along the c-axis and its minimum for $\mathbf{B}$ in the basal plane. We note that the frequency from the tear drop pocket has a very flat frequency dependence around the basal plane for both ϑ and ψ, but more pronounced for ϑ. Again, band 10 has a more complicated frequency spectrum (Figs. 7.13 (c,d)). Frequencies up to 40 kT are extracted of which Figs. 7.13 (c,d) show the part up to 12.5 kT. We do not assign all orbits here, but restrict ourselves to a few examples: The orbit at $\vartheta = \psi = 0°$ and $f = 11.4$ kT stems from the cross section of the trunk at the A-point. The frequency band between ~ 3.5 kT and 5 kT for $12.5° \leq \vartheta \leq 72.5°$ (and mirrored angles $107.5° \leq \vartheta \leq 167.5°$) originates from the roots protruding from the trunk. The dumbbell cross section of the branches on the Brillouin zone faces can be traced between for $65° \leq \psi \leq 115°$ ranging from 5.7 kT to 7.4 kT. Attention should be paid to the lowest frequency band of Figs. 7.13 (c,d) (highlighted in red), which is shown in a magnified view in Figs. 7.13 (e,f). For both angles ϑ and ψ, it extends from $0°$ to $52.5°$ (and mirrored angles $180°$ to $127.5°$). Its minimum at $f = 106$ T coincides with the c-axis. The frequency increases in a (approximately) parabolic fashion for increasing angles, but it is not found for angles $\vartheta, \psi \geq 55°$ (the increment for the SKEAF calculations was $\Delta\vartheta = \Delta\psi = 2.5°$). The maximal values at $\vartheta = \psi = 52.5°$ are 246 T and 252 T, respectively. The origin of this small orbit in the Fermi surface are thin capillaries formed at the K-points of the Brillouin zone by root branches from neighboring Brillouin zones. For a visualization it is better to change from the representation of the sheets in the Brillouin zone of reciprocal space as in Fig. 7.11 to a representation in the primitive unit cell of reciprocal space. This is depicted in Fig. 7.14, where the capillaries at the K-points can be recognized more easily.

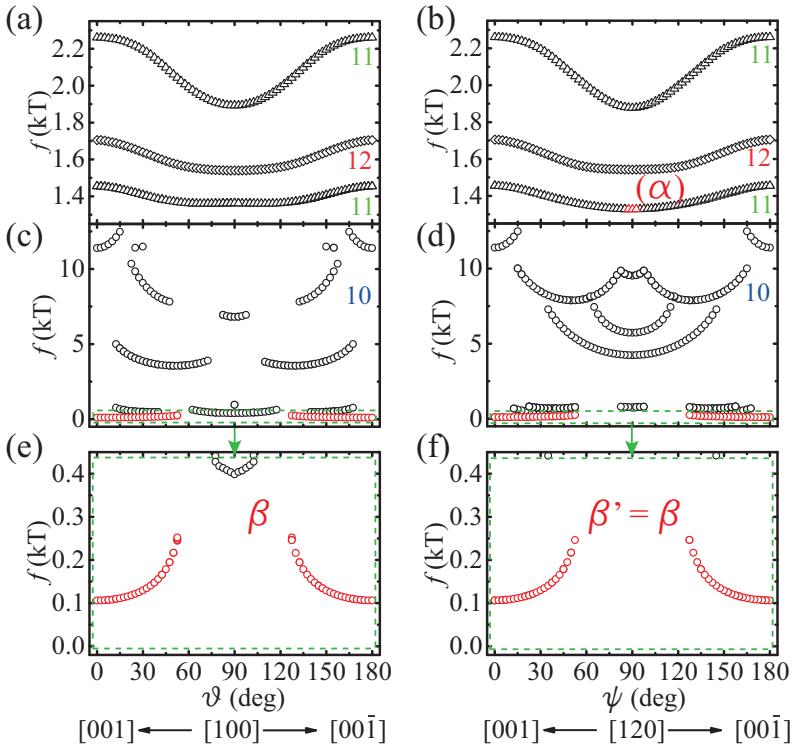

Figure 7.13: Angular dependence of dHvA frequencies of extremal orbits versus angle ϑ and ψ for rotations of $\mathbf{B}$ in the [001]-[100]-plane (left column) and in the [001]-[120]-plane (right column), respectively, as extracted from the band structure calculations using the SKEAF tool [141]. (a,b) Angular dependence of extremal orbits of band 11 and 12 corresponding to the surface sheets in Figs. 7.11 (b,c). Two orbits stemming from band 11 are depicted as triangles $\triangle$. The orbit from band 12 is represented by diamonds $\diamond$. Experimentally, only signatures of the lowest orbit (α) stemming from the tear drop-like pockets in Fig. 7.11 (b) were found for these rotation planes. The best resolution was found for $\psi \approx 90°$ (highlighted in red). (c,d) Angular dependence of extremal orbits of band 10 corresponding to the surface sheet in Fig. 7.11 (a). Many frequency branches were extracted. Only frequencies below 12.5 kT are shown. (e,f) Magnified view of the orbit highlighted in red in (c,d). The experimentally observed orbit β is assigned to this orbit stemming from the capillaries at the K-points of the Brillouin zone in Fig. 7.11 (a) and Fig. 7.14.

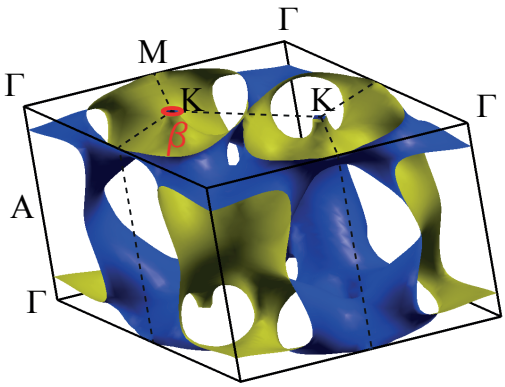

Figure 7.14: Depiction of the Fermi surface sheet of band 10 in the primitive unit cell of reciprocal space, where the capillaries forming orbit β can be recognized better than in the visualization of Fig. 7.11.

7.8 Comparison of experiment and theory

In the following, experimental and theoretical results are compared and an assignment of the experimentally observed dHvA frequencies to the orbits extracted from the band structure calculations is suggested. Similar to Ref. [12], we base the assignment on the accordance of the following quantities: dHvA frequencies and angular frequency evolutions in experiment and theory, measured effective masses and calculated band masses, and uniqueness of the theory candidate for the observed orbit.
For orbit α we suggest an identification with the tear drop-like pocket of band 11 in Fig. 7.11 (b). In the SKEAF results in Fig. 7.12 and Fig. 7.13, it is highlighted in red for those angle ranges of φ and ψ for which it has been observed. Both the observed and the theory orbit feature a 60° periodicity consistent with the lattice symmetry where the frequency is minimal for $\langle 120 \rangle$-directions and maximal for $\langle 100 \rangle$-directions (cf. Fig. 7.3 (b) and Figs. 7.12 (a,b)). The experimental frequency has an average value of 1410 T which is in very good agreement with the calculated average frequency of 1350 T. The experimental variation of the orbit frequency over φ is 95 T which is larger than the theoretical variation of 40 T. Relative to the size scale of Brillouin zone faces, which are equivalent to 52 kT, the

deviations amount to 0.1%. This is, altogether, a very good agreement of experiment and theory. The effective mass from experiment $m_\alpha^\star = 0.79\, m_\mathrm{e}$ (measured at $\varphi = 7.5°$) is enhanced by a factor of 1.6 over the calculated band mass of $m_{\mathrm{b},\alpha} = 0.49\, m_\mathrm{e}$ (extracted at $\varphi = 8°$). The enhancement of the effective mass over the band mass can be attributed to many-body interactions not taken into account in the band structure calculations [142]. If it is assumed that electron phonon interactions dominate this mass renormalization, an upper bound for the electron phonon coupling constant λ can be determined via $m^\star = (1 + \lambda)\, m_\mathrm{b}$ [143]. The analysis yields $\lambda_\alpha = 0.6$ for orbit α[1]. In principle, the ellipsoid and the sphere at the A-point from band 11 and 12, respectively, are also candidates for orbit α as they also represent closed sheets and their frequency is on the correct scale (cf. Fig. 7.12 (a)). However, we do favor the tear drop pocket over the two spheres for the following reasons: The frequency match of the tear drop pockets to α is better. The frequency variation of the observed orbit is larger than the variation of any of the three theoretical orbits, but the tear drop orbit has the greatest frequency variation of the three, hence being closest to the experiment. Finally, the frequency of the tear drop orbit is the lowest, making it the most likely to be observed within experimental limitations of finite field strength and temperature. We even find a qualitative consistency of the SKEAF calculations with the fading of the signal strength of α observed for $\varphi = \pm 30°$ (cf. Fig. 7.2 (b)) and equivalent angles and with the absence of α for rotations *through* the basal plane.
The fading for $\varphi = \pm 30°$ can be explained by the increased curvature of the sheet for this direction. In Fig. 7.12 (d) curvature A'' for orbit α is plotted for rotations of $\mathbf{B}$ in the basal plane, i. e. versus angle φ. The maximum of curvature is found at $\varphi = 30°$, thus suppressing M_osc for this direction.
In Sec. 7.3 it was argued that α should also be present for rotations in the $[001]$-$[100]$-plane and in the $[001]$-$[120]$-plane if it belongs to a closed Fermi surface sheet. However, only signatures such as in Fig. 7.5 were found in these planes (highlighted data points in Fig. 7.13 (b)). We can relate this finding to a lower anisotropy $1/f \cdot \partial f_\alpha/\partial\vartheta$ and $1/f \cdot \partial f_\alpha/\partial\psi$

[1] There is only little insight on basis of theoretical studies into the question to which degree electron phonon interactions contribute to λ in VB_2 and other transition metal diborides. Vajeeston et al. compare calculated and measured electronic specific heat coefficients and deduce for the electron phonon coupling $\lambda = 0.952$ for VB_2 and $\lambda = 0.26$ for spin-polarized MnB_2 [115]. Heid et al. report an average electron phonon coupling of $\lambda = 0.28$ for VB_2 from ab initio DFT calculations [144].

than the anisotropy in the basal plane $1/f \cdot \partial f_\alpha/\partial\varphi$ reflected in the flat frequency curves for α in Figs. 7.13 (a,b). If we approximate the anisotropy factors by the corresponding difference quotients of the SKEAF results, we in fact find a difference by a factor of three and ten, respectively

$$\left.\frac{\Delta f_\alpha}{\Delta\varphi}\right|_{\varphi=30^\circ} = 0.7\frac{\mathrm{T}}{\mathrm{deg}}, \quad \left.\frac{\Delta f_\alpha}{\Delta\psi}\right|_{\psi=90^\circ} = 0.24\frac{\mathrm{T}}{\mathrm{deg}}, \quad \left.\frac{\Delta f_\alpha}{\Delta\vartheta}\right|_{\vartheta=90^\circ} = 0.07\frac{\mathrm{T}}{\mathrm{deg}}.$$

The reduced anisotropies for ϑ and ψ might explain the absence of orbit α in the $[001]$-$[100]$- and $[001]$-$[120]$-plane in the torque experiment. These considerations are in very good agreement with the inferences from the measurements discussed in Sec. 7.3.

For β only one orbit of the SKEAF calculations matches, which is the one highlighted in red in Fig. 7.13 (c-f) stemming from the capillaries of Fig. 7.14. The agreement with experiment is striking: Experimentally, it was observed in an angular range of 102.5° while theory predicted 105°. The experimental frequency range is $102 - 188\,\mathrm{T}$ compared to $106 - 252\,\mathrm{T}$ in the calculations. We find an approximately parabolic dependence on angle in both experiment and theory. The measured effective mass $m^\star_\alpha = 0.182\,m_\mathrm{e}$ (measured at $\vartheta = 15^\circ$) is enhanced over the band mass $m_{\mathrm{b},\beta} = 0.126\,m_\mathrm{e}$ (extracted at $\vartheta = 15^\circ$) by a factor of 1.4, very similar to the enhancement of $m_{\mathrm{b},\alpha}$. The very high signal strength of β (cf. Fig. 7.2) compared to α is caused by a combination of large anisotropy $1/f \cdot \partial f_\beta/\partial\vartheta$ and small curvature along the elongated capillaries depicted in Fig. 7.14 and by the small mass.

The band structure calculations imply that both α and β have predominantly V-d character. Compared to the orbits arising from the two pockets at A of band 11 and 12, the B-p_{xy} contribution is small. Table 7.1 summarizes the experimental and theoretical results for VB_2. Karki et al. performed pulsed high-field dHvA measurements for VB_2 [131], which is the only other dHvA study of VB_2 we are aware of. Orbit β is not observed in this study. We identify our orbit α with frequency Fa = 1404 T (for $\mathbf{B} \parallel [100]$) in Ref. [131]. The agreement with our $f_\alpha = 1460\,\mathrm{T}$ for corresponding angle $\varphi = 30^\circ$ is good. Surprisingly, Karki et al. report an effective mass of $m^\star = 0.53\,m_\mathrm{e}$ for Fa. This value conincides with the "naked" band mass $m_{\mathrm{b},\alpha} = 0.52\,m_\mathrm{e}$ (extracted at $\varphi = 30^\circ$) of our band calculations, meaning essentially an absence of renormalizing many-body interactions. A corresponding analysis is however not found in Ref. [131].

Orbit	Band	f_{calc} (T)	f_{exp} (T)	$m^\star/m_\mathrm{e}$	$m_\mathrm{b}/m_\mathrm{e}$	l (nm)	λ
α	electron V-d	1350 (av.)	1410 (av.)	0.79 ± 0.03	0.49	25	0.6
β	hole V-d	106 ($\mathbf{B} \parallel [001]$)	102 ($\mathbf{B} \parallel [001]$)	0.182 ± 0.004	0.126	21	0.4

Table 7.1: Band origin, experimental and calculated dHvA frequencies, effective masses $m^\star$, band masses m_b, mean free paths l, and electron phonon coupling constants λ (upper bounds) of the experimentally observed orbits α and β in VB_2.

It seems worthwhile to comment on the absence of the majority of frequency branches found by SKEAF in the measurements. According to the calculations, all of them have either a larger mass, a higher frequency, or both, if compared to the observed orbits. Experimental limitations of finite temperature T and field strength B and sample quality consequently make their observation less likely. Larger masses lead to smaller dHvA signals via the thermal reduction factor R_T and higher frequencies are more strongly reduced via the Dingle factor R_D of Lifshitz-Kosevich theory. The Dingle temperatures (Eq. 2.36) corresponding to the mean free paths given in Table 7.1 correspond to 24 K (α) and 30 K (β), indicating only an intermediate sample quality. Thus, it is not surprising that frequencies above the 1 kT scale are not observed in the experiment. The two spherical pockets of band 11 and 12 at the A-point have band masses of 0.37 m_e and 0.29 m_e. They are interesting in that they possess the highest contribution of B-p_{xy} states of all extremal orbits determined by SKEAF. Even though they have a smaller band mass than α, we have not observed them. This can be attributed to slightly higher frequencies, smaller anisotropies, and to smaller curvatures suggested by the calculations. Potentially, their absence is also a consequence of their B-p_{xy} contributions due to higher mass enhancements of B-p_{xy}-derived states, which was observed in both CrB_2 and MgB_2 [12, 145]. For comparative purposes their observation would be particularly interesting in consecutive experiments.
In summary, we find the two experimentally observed orbits α and β along with their angular frequency dependence in very good agreement with the band structure calculations. The measured effective masses are enhanced over the calculated band masses by similar factors 1.6 and 1.4, respectively, which also indicates a consistency as both orbits share their origin

from V-d states. Furthermore, the angular variation of observed dHvA signal intensities can be related to the angular dependence of calculated sheet anisotropies and curvatures. Effectively, the dHvA measurements for VB_2 thus confirm the high reliability of DFT band structure calculations, specifically for non-magnetic compounds. Future experiments at higher fields and lower temperatures could allow for the observation of more orbits predicted by the calculations and provide useful information on many-body interactions in VB_2, particularly the electron phonon coupling of B-p_{xy}-derived states.

8 De Haas-van Alphen effect and Fermi surface properties of MnB_2

In this chapter, the de Haas-van Alphen (dHvA) effect of single crystal MnB_2 is investigated in order to derive Fermi surface properties of MnB_2. The dHvA effect is derived from the quantum oscillatory component of the torque measured by cantilever magnetometry.
The chapter is organized as follows: The general experimental procedure is briefly explained in Sec. 8.1. Experimental results of the angular, temperature, and field dependence of the dHvA effect are presented and analyzed in Sec. 8.2-8.5. This is followed by a presentation and analysis of results of band structure calculations in Sec. 8.6-8.7, before turning to a comparison of the experimental findings and the calculations in Sec. 8.8. The chapter is concluded with a comparison of the results for MnB_2 and VB_2 with the isostructural compounds CrB_2 and MgB_2 in Sec. 8.9.

8.1 Experimental procedure

For the magnetization experiments with the MnB_2 sample, which has been described in Ch. 6, a procedure very similar to the one for VB_2 (Sec. 7.1) was followed. The sample was glued onto a CuBe cantilever (Sec. 3.2), which itself was mounted onto a rotary stage of a ^{3}He insert operated in a 15 T-superconducting magnet. The capacitive readout technique (Sec. 3.3) was used. However, for MnB_2 the orientation of the magnetic field $\mathbf{B}$ could only be varied within the basal plane. Figure 8.1 (a) shows the orientation of the crystal relative to the applied field and the convention for the experimental angle φ, denoting the orientation of $\mathbf{B}$ relative to the $[120]$-axis. Note that the crystal was placed on the cantilever with a different orientation than for VB_2 in Ch. 7, but the convention for φ is identical with the notation of Ch. 7 relative to the crystal structure.
Outside the basal plane, magnetization measurements were not fruitful because the magnetic moment along the c-axis resulting from the canting of the localized momenta in the hexagonal planes (cf. Ch. 6) caused an irre-

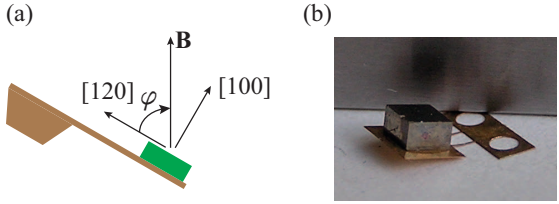

Figure 8.1: (a) Side view of CuBe cantilever with the MnB_2 sample attached to it. The orientation of the magnetic field $\mathbf{B}$ with respect to the sample was varied wihtin the basal plane. The angle φ represents the angle of $\mathbf{B}$ in the basal plane relative to the $[120]$-axis. (b) Deformed cantilever with attached sample after an attempt of magnetization experiments in the $[001]$-$[120]$-plane.

versible deformation of the cantilever for these orientations. Fig. 8.1 (b) shows a photography of a cantilever with the MnB_2 sample attached to it after an attempt to perform torque measurements with $\mathbf{B}$ oriented in the $[001]$-$[120]$-plane. The paddle has been bent considerably by the large torque.

8.2 Experimental findings

Typical experimental data are illustrated in Fig. 8.2. Figure 8.2 (a) shows raw data, i. e. capacitance C versus magnetic field B for three different angles φ. Depending on angle φ, a large non-oscillatory background signal is present. The origin of the background signal is not the topic of this thesis. However, it necessitates a more careful subtraction procedure than for VB_2 to arrive at the oscillatory part of the magnetization M_{osc}. Generally, a polynomial was fitted to the raw capacitance data as a function of field strength B and then subtracted. Then for every value of B, the subtracted data were multiplied by $C_0^2/C(B)^2 \cdot K(C_0)$, where $C(B)$ is the the capacitance data value and $K(C_0)$ is the calibration constant at capacitance C_0. For large variations of the overall capacitance, this modification of the calibration scheme is necessary to account for the dependence of the calibration constant $K(C)$ on capacitance C since K scales with the inverse square of the cantilever's capacitance (cf. Sec. 3.4). To further reduce the non-oscillatory part of the signal, a moving average of the signal as a function of $1/B$ was subtracted. The number of data points to be averaged over

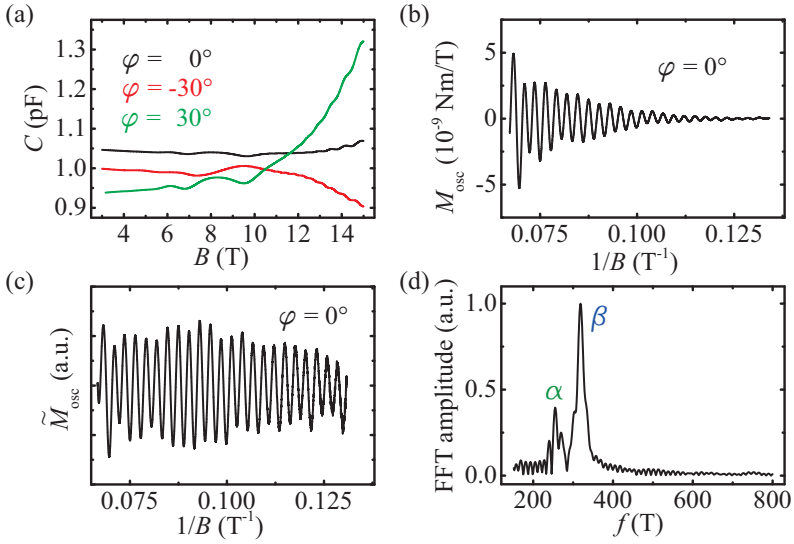

Figure 8.2: (a) Raw capacitance data C as a function of magnetic field B for $\varphi = -30°$, $0°$, and $30°$. (b) Oscillatory part of magnetization M_{osc} for $\varphi = 0°$ versus inverse magnetic field. (c) "Inflated" oscillatory part of magnetization $\tilde{M}_{\mathrm{osc}}(1/B)$ versus inverse magnetic field for $\varphi = 0°$. (d) FFT data exhibiting two dHvA orbits α and β.

was adjusted such that the signal was effectively disposed of frequencies lower than 40 T. Figure 8.2 (b) shows resulting data for the oscillatory part of magnetization M_{osc} as a function of inverse field $1/B$ for $\varphi = 0°$. The signal shows a slight beating pattern. This can be inferred from the fact that the envelope function is not a pure decay for increasing inverse field since the amplitudes of consecutive oscillations do not decrease continuously. Hence, more than one frequency must be present. To enhance the frequency resolution, the analysis of Ch. 7 was adapted to this finding: the FFTs are not based on $M_{\mathrm{osc}}(1/B)$ solely, but on $M_{\mathrm{osc}}(1/B) \cdot \exp(\xi/B)$ where $\exp(\xi/B)$ is a heuristic, exponentially increasing factor to counterbalance the Dingle reduction factor R_{D} originating from finite relaxation time τ. Fig. 8.2 (c) shows the resulting function $\tilde{M}_{\mathrm{osc}}(1/B)$, which corresponds to $M_{\mathrm{osc}}(1/B)$ in Fig. 8.2 (b). Figure 8.2 (d) depicts a fast Fourier

transform of magnetization $\tilde{M}_{\mathrm{osc}}(1/B)$. Two frequencies f_α and f_β belonging to two orbits α and β, respectively, can clearly be resolved where the amplitude of f_β exceeds the one of f_α by a factor of approximately 2.5. Using the scaling factor $\exp(\xi/B)$, the two frequencies were resolved in the entire basal plane.
We note that the "inflation" procedure - while sharpening the main peaks - increases the height of the side lobes of the FFT peaks. For example, the lobe right to the α-peak in Fig. 8.2 (d) is not attributed to a distinct third frequency. It is shifted by 15 T, which coincides exactly with the position where the first side lobe of the α-peak is to be expected for the given window width of the signal in $1/B$. A similar analysis was performed for all FFTs of the angle-dependent measurements of the following section.

8.3 Angular dependence

The angular dependence of orbits α and β was studied in the basal plane in an angular range of 165° with increments of 7.5°. FFTs of the "inflated" magnetization $\tilde{M}_{\mathrm{osc}}(1/B)$ were analyzed for every angle φ to extract the dHvA frequencies. Orbit β was traced over the entire angular range and orbit α was detected for a range of 120°. Fig. 8.3 illustrates the angular dependencies of frequencies f_β (black squares) and f_α (open circles). The fact that α could not be resolved for $\varphi < -67.5°$ and $\varphi > 52.5°$ is assumed to be due to experimental limitations. In these angle ranges the overall capacitance signal C as a function of magnetic field B features a sharp peak at positions between 9.5 T and 12.5 T. The exact position was found to vary in different measurements. Typical data are shown in Fig. 8.4 for $\varphi = -60°$ and $\varphi = 60°$. The origin of this feature is not known. No systematic dependence was found: The position of the peak did not coincide with angles reflecting specific crystal symmetries. The two angles of Fig. 8.4 ($\varphi = -60°$ and $\varphi = 60°$) as well as the data for $\varphi = 0°$ in Fig. 8.2 (a) were in fact equivalent with respect to the symmetry of the hexagonal plane. However, for $\varphi = -60°$ and for $\varphi = 60°$ the positions of the peak significantly differed while for $\varphi = 0°$ the peak was not found at all. Moreover, the position of the peak did not coincide in different measurements for one angle after the orientation of the cantilever had been varied to a different angle and then changed back to the former angle again. Also, the position of the peak did not coincide in subsequent cool-down cycles. Fur-

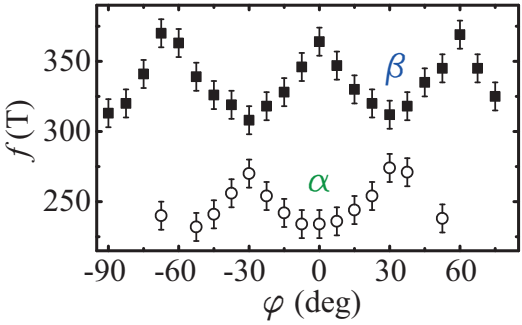

Figure 8.3: Angular dHvA frequency dependencies of orbit α and β for a rotation of the magnetic field $\mathbf{B}$ in the basal plane. Both orbits exhibit a 60° periodicity.

thermore, a dependence on the canting of the ordered magnetic momenta (cf. Sec. 6.3) could be ruled out. For this, the temperature was increased to 180 K, i. e. beyond $T_C \approx 157$ K, below which the canting is assumed to occur. However, the peak feature still appeared. We therefore assume that the cause of this feature is probably not purely magnetic, but more likely a complicated interplay between magnetic and mechanical, possibly magnetostrictive effects. A further investigation was not within the scope of this thesis. It is noteworthy that the sharp capacitance peak decreased the frequency resolution of respective experiments by reducing the inverse field range on which the FFTs were based. We therefore strongly assume that the absence of α for the corresponding angles is not a feature of the Fermi surface, but only due to the discussed experimental limitation.
Both f_α and f_β feature a 60° periodicity consistent with the sixfold symmetry of the hexagonal plane. Frequency f_α varies between ~ 235 T and ~ 270 T and f_β varies between ~ 310 T and ~ 365 T. Thereby, minima of f_α coincide with maxima of f_β at $\varphi = -60°$, 0°, and 60° and likewise maxima of f_α coincide with minima of f_β at $\varphi = -30°$ and 30°. This antiphase behavior of f_α and f_β will be explained in the context of the discussion of the Fermi surface sheet from which the two orbits arise in Sec. 8.8.
Both orbits α and β stem from closed Fermi surface sheets since they were observed for a full 60° period (and more). The peak-to-peak variation of extremal area corresponding to the observed frequency variation is 15%

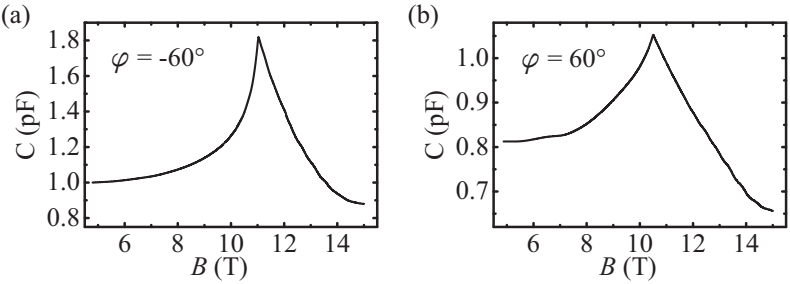

Figure 8.4: Raw data for $\varphi < -57.5°$ and $\varphi > 52.5°$ feature a sharp peak in the field range between 9.5 T and 12.5 T. The origin of this feature is not the subject of this thesis, but resolution of the FFTs for determination of dHvA frequencies is effectively reduced by the peaks.

and 18%, respectively.

8.4 Temperature dependence

The temperature dependence of the dHvA signals from α and β was studied at angle $\varphi = -15°$ for temperatures $T = 0.3\,\mathrm{K}$, $0.8\,\mathrm{K}$, $1.25\,\mathrm{K}$, $2.0\,\mathrm{K}$, $3.0\,\mathrm{K}$, and $4.0\,\mathrm{K}$ in order to determine the effective masses of the respective orbits. FFT spectra of $\tilde{M}_{\mathrm{osc}}$ were analyzed to extract the temperature-dependent Fourier amplitude $I(T)$ for both α and β. The spectra are based on an inverse field range corresponding to $B_{\mathrm{min}} = 6.3\,\mathrm{T}$ and $B_{\mathrm{max}} = 14.0\,\mathrm{T}$. Figure 8.5 illustrates the experimental data. In Fig. 8.5 (a) the FFT amplitude $I(f)$ is depicted versus frequency f. Both peaks decrease with increasing temperature and almost completely vanish for $T = 4.0\,\mathrm{K}$. In Fig. 8.5 (b) the peak heights of the FFTs of Fig. 8.5 (a), normalized to the peak height at $T = 0.3\,\mathrm{K}$, are plotted versus temperature T. The black squares represent frequency f_β and the open circles represent f_α. Similarly to Sec. 7.4, the temperature reduction factor R_{T} Eq. 2.32 (multiplied by a multiplicative constant) is fitted to each data set to extract the effective mass $m^\star$ of the respective extremal orbit. For B the arithmetic mean $\bar{B} = (B_{\mathrm{min}} + B_{\mathrm{max}})/2$ of the analyzed field range was inserted. The fits are depicted as solid lines in Fig. 8.5 (b), green corresponding to α and

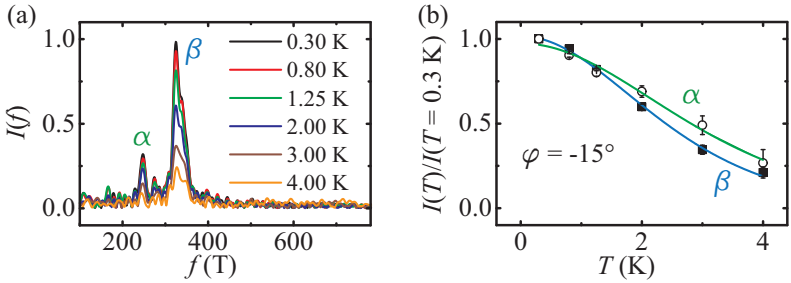

Figure 8.5: Temperature dependence of the signal strength of dHvA frequencies f_α and f_β. (a) Temperature-dependent fast Fourier transforms of $\tilde{M}_{\mathrm{osc}}(1/B)$ at $\varphi = -15°$ for $T = 0.3\,\mathrm{K}, 0.8\,\mathrm{K}, 1.25\,\mathrm{K}, 2.0\,\mathrm{K}, 3.0\,\mathrm{K}$, and $4.0\,\mathrm{K}$. (b) Normalized FFT amplitudes $I(T)/I(T = 0.3\,\mathrm{K})$ corresponding to the data in (a) and fits of Eq. 7.1 to the data points as a function of temperature. Open circles (data points) and the solid green line (fit) represent data for orbit α. Black squares (data points) and the solid blue line (fit) represent data for orbit β. The fits reveal effective masses of $m^\star_\alpha = (0.50 \pm 0.05)\, m_\mathrm{e}$ and $m^\star_\beta = (0.64 \pm 0.03)\, m_\mathrm{e}$.

blue corresponding to β. The effective masses determined by this analysis are $m^\star_\alpha = (0.50 \pm 0.05)\, m_\mathrm{e}$ and $m^\star_\beta = (0.64 \pm 0.03)\, m_\mathrm{e}$.

8.5 Field dependence

Similar to Sec. 7.5, the mean free path l_β of orbit β was determined after extraction of the effective masses. For this, the full Lifshitz-Kosevich formula

$$\Gamma_{\mathrm{osc}} = C^0_\beta \cdot B^{\frac{3}{2}} \underbrace{\exp\left(-\frac{\pi m_{\mathrm{b},\beta}}{eB\tau}\right)}_{R_{\mathrm{D},\beta}} \underbrace{\frac{X_\beta}{\sinh X_\beta}}_{R_{\mathrm{T},\beta}} \sin\left(\frac{2\pi f_\beta}{B} + \phi_\beta\right), \qquad (8.1)$$

was fitted to the torque data Γ_{osc} at angle $\varphi = 0°$, where C^0_β, $m_{\mathrm{b},\beta}/\tau$, and ϕ_β were used as free fit parameters and values for f_β and $m^\star_\beta$ were inserted as determined above. The approximation of free electrons on a circular orbit was again applied by replacing $m_{\mathrm{b},\beta}/\tau$ through $\hbar k_\mathrm{F}/l_\beta$ and

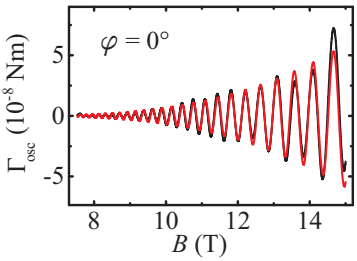

Figure 8.6: Dingle analysis of orbit β. (a) Γ_{osc} for $\varphi = 0°$ as a function of field strength B (black line). The red line is a fit of Eq. 8.1 to the data using f_β and $m^\star_\beta$ as determined in the previous sections. It yields the free mean path $l_\beta = 48\,\mathrm{nm}$.

$\pi k_{\mathrm{F}}^2 = (2\pi e f_\beta)/\hbar$ (cf. Sec. 7.5). Figure 8.6 depicts the experimental torque data (black line) as well as the fit (red line). The fit yields the mean free path $l_\beta = 48\,\mathrm{nm}$. It was also tried to fit Eq. 7.2 for both frequencies f_α and f_β to the data, increasing the number of free parameters to six (C^0_α, C^0_β, $m_{\mathrm{b},\alpha}/\tau$, $m_{\mathrm{b},\beta}/\tau$, ϕ_α, ϕ_β). However, the fit did not provide physically meaningful results for orbit α. It is assumed that the contribution of α and the field range window is too small and the number of free parameters is too large in order to extract reasonable mean free paths for both orbits.

8.6 Band structure and Fermi surface

Band structure calculations for MnB_2 were performed by J. Kuneš applying the local spin density approximation method of density functional theory. Experimental lattice constants of $a = 3.0062\,\text{Å}$ and $c = 3.0288\,\text{Å}$ were used, which were determined by X-ray diffraction at $T = 12\,\mathrm{K}$ for a sample grown in the same float-zoning process as the investigated sample [146]. Different from VB_2, MnB_2 exhibits magnetic order below $T_{\mathrm{N}} = 760\,\mathrm{K}$ as discussed in Ch. 6. In the calculations, the pure AF-c state was considered, i. e. the canting of the localized moments at the Mn sites towards the c-axis was not taken into account. The AF-c structure corresponds to a doubling of the magnetic unit cell in c-direction or equivalently to cutting the Brillouin zone of reciprocal space in half. The corresponding backfolding results in a doubling of bands in K-space compared to a hypo-

thetically non-magnetic compound. Figure 8.7 depicts the band structure along high-symmetry directions of the Brillouin zone. In total, four bands highlighted in red, blue, purple, and green cross the Fermi Energy E_{F}. In the following, we refer to them as bands 21, 22, 23, and 24, respectively[1]. Figure 8.8 shows the density of states $n(E)$, normalized to one formula unit (f. u.), as a function of energy E as derived from the calculated band structure assuming the AF-c ordered state. Similar to Sec. 7.6, in addition to the total DOS, the contributions from B-2s, B-2p, and Mn-3d states are also drawn separately. The main difference to the DOS of non-magnetic transition metal diborides, as discussed in Sec. 6.1, is the splitting of the Mn-d peak into two peaks by the AF-c order, one below and one above the Fermi energy E_{F}, by convention again set to $E_{\mathrm{F}} = 0$. Hereby, the DOS is depicted for a Mn atom Mn1 with a localized moment and the two peaks relate to spin-up and spin-down projection with respect to the polarization of Mn1 (density of states DOS1). For a second Mn atom in a neighboring hexagonal plane, Mn2, i. e. with opposite polarization, the density of states DOS2 would be the same. Only the up- and down-labels of the peaks would be reversed, thus restoring the symmetry of the DOS with respect to spin projection[2]. The Fermi energy resides in the region of low DOS between the two Mn-d peaks. Despite of the Mn-d peak splitting, the states at E_{F} still have predominantly Mn-d character with an admixture of B-p orbitals as in non-magnetic transition metal diborides. In more detail, similar to VB_2, the B-p admixture to the bands around E_{F} is almost entirely from B-p_{xy} states. The B-p_z states are pushed away from E_{F}. Hereby, the degree of the B-p_{xy} admixture varies depending on K-space direction and band index. This can be derived from corresponding fat band plots, discussed in App. A, indicating B-p_{xy}, B-p_z, and Mn-d contributions to the bands separately. We postpone a detailed discussion of the nature of the electronic states at E_{F} to a comparative discussion of the experimental results for MnB_2 along with the isostructural compounds VB_2, CrB_2, and MgB_2 in Sec. 8.9.

In Fig. 8.9 the Fermi surface sheets of the four bands that cross E_{F} are depicted in the Brillouin zone. For clarity they are drawn in separate subfig-

[1] Similarly to Sec. 7.6, the numbering of the bands is adopted from the WIEN2k results. The doubling of the unit cell by the magnetic order explains the fact that there are approximately twice as many occupied bands as in VB_2.

[2] The density of states DOS1 and DOS2 are related to each other by DOS1(↑) = DOS2(↓) and DOS1(↓) = DOS2(↑).

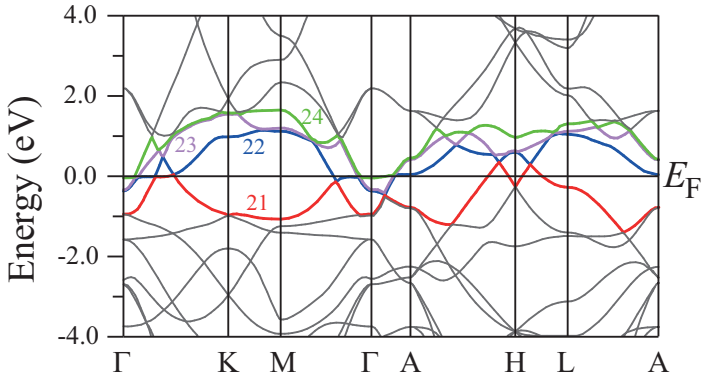

Figure 8.7: Calculated band structure of MnB_2 with AF-c magnetic order using the WIEN2k package along high-symmetry directions of K-space. Four bands (red, blue, purple, green) cross E_F, denoted as band 21, 22, 23, and 24.

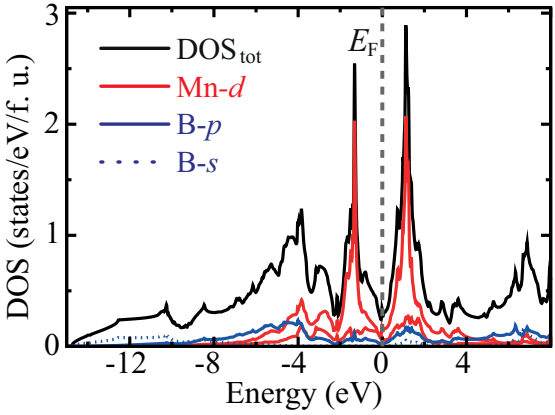

Figure 8.8: Density of states (DOS) of MnB_2 per formula unit (f. u.) as inferred from the calculated band structure with AF-c order. The total DOS is shown and additionally the contributions from B-2s, B-2p, and V-3d states are drawn separately. The M-d peak of the typical DOS of non-magnetic transition metal diborides MB_2, discussed in Sec. 6.1, splits into two peaks by the AF-c order. Hereby, the Fermi energy E_F, by convention set to $E_F = 0$, resides in the region of low DOS between the two peaks. The states at E_F are dominated by Mn-d components with an admixture of B-p orbitals.

ures. Since the unit cell was doubled in the c-direction for the calculation, the Brillouin zone is correspondingly cut in half. The hexagonal plane and the faces of the Brillouin zone have equivalent areas of 53 kT and 26 kT, respectively. The red sheets in Fig. 8.9 (a) represent the Fermi surface of band 21. The sheets are composed of tori at the H-points with horn-like protrusions pointing towards the Γ-points. Each torus is segmented into six identical parts, each part belonging to one of the six neighboring Brillouin zones at each H-point. For this reason, the sheet of band 21 is better drawn in the primitive unit cell of reciprocal space as in Fig. 8.10. In this representation, the six segments of neighboring Brillouin zones complement each other to form one torus with six protrusions at each of the two H-points of the primitive unit cell. The Fermi surface sheets of bands 22, 23, and 24 are located at the Γ-points and depicted in Fig. 8.9 (b-d). Sheet 22 in Fig. 8.9 (b) resembles a spinning top with its axis oriented along the c-axis. Both band 23 and band 24 feature sheets that are nearly ellipsoidal with their elongated axes oriented along the c-axis. Hereby, the ellipsoid of band 24 is smaller and closer to a sphere than the one from band 23.

8.7 Extraction of dHvA frequencies

The SKEAF program (Sec. 7.7, [141]) was employed to extract dHvA frequencies from the band structure data calculated with WIEN2k. Since magnetization experiments were only performed in the hexagonal plane, we restrict ourselves in this chapter to the presentation of the results for a rotation of $\mathbf{B}$ in this plane. The calculated dHvA frequencies for rotations of $\mathbf{B}$ through the hexagonal plane are presented in App. B. Figure 8.11 depicts the results for the hexagonal plane. DHvA frequencies are plotted versus angle φ in every subfigure. Figure 8.11 (a) represents the results of band 21 corresponding to the tori of Fig. 8.9 (a) while the frequencies of bands 22, 23, and 24 corresponding to the sheets of Fig. 8.9 (b-d) are summarized in Fig. 8.11 (b). In Fig. 8.11 (b), dHvA frequencies stemming from the spinning top of band 22 are represented by squares $\square$, frequencies from the ellipsoid of band 23 are represented by triangles $\triangle$, and frequencies from the ellipsoid of band 24 are represented by diamonds $\diamond$, with the $\square$-branch of band 22 having the highest frequencies and the $\diamond$-branch of band 24 having the lowest frequencies.
All frequency branches depicted in Fig. 8.11 (a) arise from the tori with

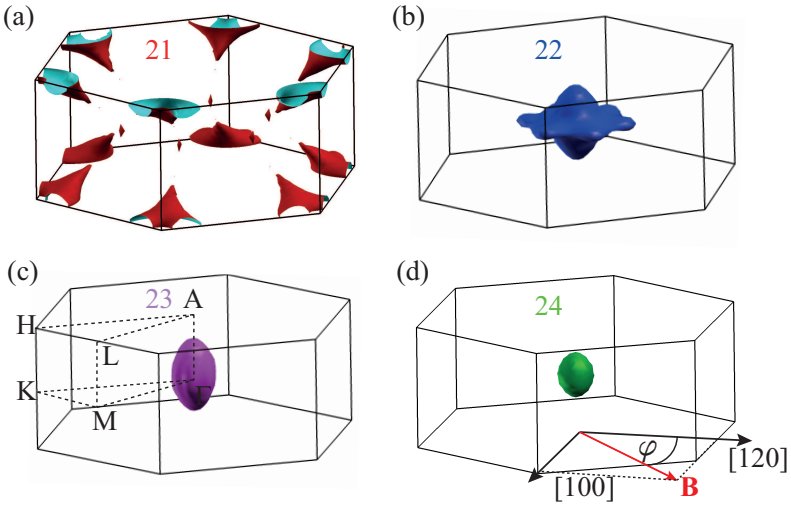

Figure 8.9: Fermi surface sheets of the four bands crossing E_F depicted in the Brillouin zone. For clarity, they are drawn separately. (a) Sheet 21 consists of tori at the H-points with horn-like protrusions pointing towards Γ. Each torus is segmented into six parts distributed over neighboring zones. (b) Sheet 22 resembles a spinning top at Γ with its axis oriented along the c-axis. (c) Sheet 23 is an ellipsoidal pocket at Γ with its elongated axis along the c-axis. (d) Sheet 24 also consists of an ellipsoidal pocket at at Γ with its elongated axis along the c-axis. It is less elongated than sheet 23. Fig. (d) also depicts the real-space crystal orientations $[100]$ and $[120]$ relative to the Brillouin zone along with the experimental angle φ. The areas of the faces and the hexagonal plane of the Brillouin zone are equivalent to dHvA frequencies of 26 kT and 53 kT, respectively.

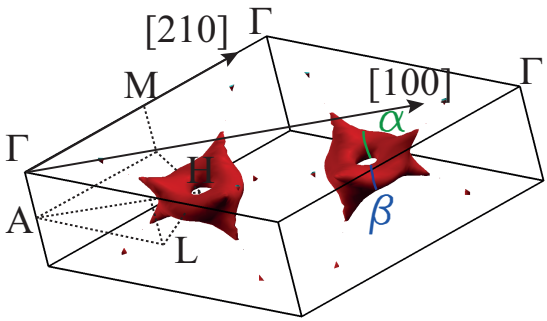

Figure 8.10: Depiction of the Fermi surface sheet of band 21 in the primitive unit cell of reciprocal space, where the torus segments of neighboring Brillouin zones complement each other to form one torus with six protrusions at each of the two H-points of the primitive unit cell. The experimentally observed orbits α and β are assigned to the minimal torus cross sections. The origin of the orbits from the minimal cross sections of a simple torus varied by the addition of the protrusions explains the antiphase behavior of α and β observed in the experiment. Real-space orientations $[100]$ and $[210]$ are indicated.

the protrusions at the H-points. To understand how they arise, a simple torus is considered first as depicted in Fig. 8.12. For orientations of the magnetic field in the plane perpendicular to the rotational axis of the torus, a simple torus has two extremal areas with two copies each. One extremal cross section arises from the two identical circles of radius r perpendicular to $\mathbf{B}$ (depicted in green). These areas are minimal areas. For continuity reasons there must also be maximal areas (depicted in red) whose exact position depends on the ratio of r and R. For an ideal torus, the area of minimal and maximal cross sections does not depend on the orientation of $\mathbf{B}$ in the plane perpendicular to the rotational axis. For the tori of band 21 at the H-points of reciprocal space (Fig. 8.10), the protrusions towards the Γ-points alter the above considerations: There are two smaller extremal cross sections to be compared with the green circles of the simple torus, whose areas are not necessarily the same because they are varied by the protrusions depending on the orientation of $\mathbf{B}$. These are minimal cross sections. Accordingly, there are also two maximal cross sections, which are to be compared with the red areas of the simple torus. Their areas are

also varied by the protrusions depending on the orientation of $\mathbf{B}$. For this reason, the two copies of the green minimal cross sections (circles) and the two copies of the red maximal cross sections of the simple torus split into four frequency bands in Fig. 8.11 (a). If $\mathbf{B}$ is oriented along Γ-K-lines, the two smaller extremal areas coincide for symmetry reasons and hence the two corresponding frequency branches cross. This constellation corresponds to $\langle 100 \rangle$-orientations or alternatively for $\varphi = 30° + n \cdot 60°$ ($n \in \mathbb{Z}$) (cf. Fig. 8.10). Similarly, the two larger extremal areas coincide if $\mathbf{B}$ is oriented along Γ-M-lines, i. e. $\langle 120 \rangle$-orientations, which corresponds to $\varphi = n \cdot 60°$. Between $\varphi = 10°$ and $12°$ (and mirrored angles $48°$ and $50°$), the upper frequency band of the smaller extremal areas jumps by approximately 0.5 kT. This a consequence of the fact that in the proximity of the horn-like protrusions the surface normal abruptly changes its orientation. For this reason, the extremal cross section is located "on" the horn for angles $\varphi \leq 10°$. Between $10°$ and $12°$, the extremal cross section "slips off" the horn and is located besides the horn on the torus for angles $\varphi \geq 12°$ where it has a considerably smaller area.

8.8 Comparison of experiment and theory

In the following, experimental and theoretical results are compared and an assignment of the experimentally observed dHvA frequencies to the orbits extracted from the band structure calculations is suggested. We again base the assignment on the accordance of: dHvA frequencies and angular frequency evolutions in experiment and theory, measured effective masses and calculated band masses, and uniqueness of the theory candidate for the observed orbit.

We suggest that the observed orbits α and β stem from the two minimal cross sections of the tori with the protrusions, whose origins have been discussed in Sec. 8.7. The corresponding frequency branches are highlighted in green and blue in Fig. 8.11 (a). Of all the frequency branches in Figs. 8.11 (a,b) the frequency match for the the two small torus orbits is the best although the theoretical values exceed the experiment by ~ 180 T. This corresponds however to only 0.3 % of the area of the hexagonal basal plane of the Brillouin zone, which represents a good agreement. A rigid band shift of only ~ 60 meV can bring the calculated frequency branches into very good coincidence with the measured frequencies of α and β.

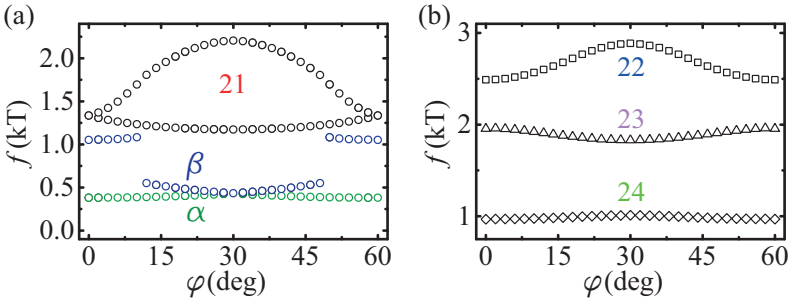

Figure 8.11: Angular dependence of dHvA frequencies of extremal orbits versus angle φ for rotations of $\mathbf{B}$ in the basal plane as extracted from the band structure calculations using the SKEAF tool [141]. (a) Angular dependence of extremal orbits of band 21 corresponding to the surface sheet in Fig. 8.9 (a) or Fig. 8.10, respectively. Four frequency branches are present. They arise from two minimal and two maximal cross sections of the tori at the H-points. (b) Angular dependence of extremal orbits of bands 22-24. DHvA frequencies from band 22 are represented by squares □, frequencies from band 23 are represented by triangles △, and frequencies from band 24 are represented by diamonds ◇. The experimentally observed orbits α and β are assigned to the two lower frequency branches in (a) stemming from the minimal cross sections of the tori.

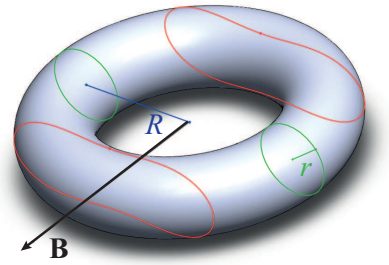

Figure 8.12: Extremal areas of a simple torus for orientations of the magnetic field $\mathbf{B}$ perpendicular to the rotational axis of the torus. There are two identical minimal cross sections (green circles) and two identical maximal cross sections (red areas).

The antiphase frequency evolutions of α and β in experiment (Fig. 8.3) and of the two minimal cross sections of the horned tori in the calculations (Fig. 8.11 (a)) are similar. The two branches separate when $\mathbf{B}$ tilts towards $\langle 120 \rangle$ ($\varphi = -60°, 0°, \ldots$) both in experiment and in theory. The calculated branches cross each other for $\langle 100 \rangle$-directions ($\varphi = -30°, 30°, \ldots$). This crossing is not observed in experiment, but in experiment the f_α and f_β branch are closest for the same angles. Moreover, we do not observe a jump for f_β like the jump for the upper (blue) frequency branch in Fig. 8.11 (a). The pronounced horns of the tori in Fig. 8.10, which cause the jumps, could be an exaggerated feature of the calculations as a consequence of the fact that the DFT calculations do not take fully into account all interactions. Inclusion of further interactions generally smooths out Fermi surfaces [147], which could explain the absence of the jumps in the measurements. Moreover, the non-crossing of the experimental frequency branches could be caused by a slight mismatch of the sample edges and the crystal symmetry axes, by a slight misalignment of the sample on the cantilever, a slight misalignment of the cantilever with respect to the magnetic field, or a combination thereof. There is additional support for the attribution of α and β to the two smaller extremal cross sections of the tori: (1) Other candidate frequencies have a higher frequency mismatch thus requiring more substantial band shifts to bring calculations and measurements into coincidence. (2) We note that the torque signals for the two branches f_α and f_β have similar intensities for $\varphi = -30°, 30°, \ldots$, i. e., where the branches are closest in experiment. This supports that they stem in fact from the same Fermi surface features. Also, for this orientation the two minimal torus cross sections are identical for symmetry reasons. Hence, this represents a consistency of experiment and theory. (3) For other angles, f_β has a stronger signal than f_α which is consistent with the anisotropies $1/f \cdot \partial f/\partial\varphi$ of the branches in Fig. 8.11 (a), where the corresponding derivative for the upper (blue) band is higher than for the lower (green) band. (4) All other frequency branches in Fig. 8.11 (a,b) have band masses m_b of 0.65-2.89 m_e such that their band masses surpass the measured effective masses of $m_\beta^\star = 0.64\, m_\mathrm{e}$ and $m_\alpha^\star = 0.50\, m_\mathrm{e}$, which argues against their identification with the observed orbits.

After the identification of α and β with the minimal tori cross sections, the respective mass enhancements can be determined. From the SKEAF results we extract at $\varphi = 14°$ band masses $m_{\mathrm{b},\alpha} = 0.31\, m_\mathrm{e}$ and $m_{\mathrm{b},\beta} = 0.42\, m_\mathrm{e}$, which yields a mass enhancement of the measured effective masses

Orbit	Band	f_{calc} (T)	f_{exp} (T)	$m^\star/m_\mathrm{e}$	$m_\mathrm{b}/m_\mathrm{e}$	l (nm)	λ
α	hole Mn-d	405 (av.)	250 (av.)	0.50 ± 0.05	0.31		0.6
β	hole Mn-d	490 (av.)	340 (av.)	0.64 ± 0.03	0.42	48	0.5

Table 8.1: Band origin, experimental and calculated dHvA frequencies, effective masses $m^\star$, band masses m_b, mean free paths l, and electron phonon coupling constants λ (upper bounds) of the experimentally observed orbits α and β in MnB_2.

$m^\star_\alpha = 0.50\, m_\mathrm{e}$ and $m^\star_\beta = 0.64\, m_\mathrm{e}$ by a factor of 1.6 and 1.5, respectively. Accordingly, estimates for upper bounds of the electron phonon coupling strengths are $\lambda_\alpha = 0.6$ and $\lambda_\beta = 0.5$ (cf. Sec. 7.8). The band structure calculations suggest that the torus orbits have predominantly Mn-d character. Compared to the orbits arising from sheets 22 and 23 (spinning top and ellipsoid) the B-p_{xy} contribution is small.

Table 8.1 summarizes the experimental and theoretical results for MnB_2 from our experiments, which are the first dHvA measurements for MnB_2 to the best of our knowledge. The maximal torus orbits from band 21 and the orbits from the electron pockets of bands 22-23 are absent in the experimental data. According to the SKEAF results all of them have higher masses, higher frequencies, or both properties compared to the observed orbits. By the same arguments as in Sec. 7.8, this can explain their absence. The Dingle temperature corresponding to the mean free path given in Table 8.1 corresponds to 7 K (β), indicating a better sample quality than for VB_2. The spinning top pocket of band 22 and the ellipsoidal pocket of band 23 are interesting for having significantly larger contributions of B-p_{xy} states than the tori of band 21. Their observation would therefore be particularly interesting in consecutive experiments for a comparison of electron phonon coupling strengths of B-p_{xy}-derived bands in MnB_2 with other transition metal diborides.

In summary, we find the two experimentally observed orbits α and β along with their angular frequency dependence in good agreement with the band structure calculations. They can be assigned to the same Fermi surface feature, i. e. torus-like sheets at the H-points of the Brillouin zone. The measured effective masses are enhanced over the calculated band masses by factors 1.6 and 1.5. The orbits have a hole-like Mn-d character. The agreement of measured and calculated Fermi surface features is interesting in view of the magnetic order of MnB_2: The AF-c state assumed in the

calculations reproduces measured features well and the electronic structure seems to be altered only slightly by the out-of-plane canting of the ordered moments. Experiments at higher fields and lower temperatures are expected to allow for the observation of more orbits predicted by the calculations and thus to provide useful information on many-body interactions in MnB_2. Particularly interesting are the electron phonon coupling of B-p_{xy}-derived states as well as a more rigorous test of the Fermi surface properties predicted by the calculations.

8.9 Comparison with CrB_2 and MgB_2

It is instructive to compare our results from Ch. 7 and Ch. 8 for VB_2 and MnB_2, respectively, with the isostructural compounds CrB_2 and MgB_2. We start with a short review of the experimental findings for CrB_2 in Ref. [12] and then compare the dHvA results and Fermi surface properties of transition metal diborides VB_2, CrB_2, and MnB_2. This is followed by a review of the electronic structure and Fermi surface properties of MgB_2 before we conclude with some comments on common properties as well as differences between transition metal diborides and MgB_2.

For CrB_2 Brasse et al. reported the observation of three dHvA orbits and studied the variation of dHvA effect frequencies depending on the field orientation [12]. The experimental results were compared to DFT calculations respecting the cycloidal magnetic order of CrB_2 discussed in Sec. 6.3. Two of the three orbits, β_{Cr} and δ_{Cr}, were assigned to bands with B-p_{xy} character, while the third orbit α_{Cr} was tentatively assigned to a band with Cr-d character. The phonon coupling constants λ for the two B-p_{xy} orbits were reported to be λ = 1.3 and λ = 1.0 (upper bounds), respectively. The presumable Cr-d orbit has a lower coupling constant of $\lambda \approx 0.3$. Table 8.2 summarizes the results for the transition metal (M) diborides MB_2 of Ref. [12] and Chs. 7 and 8.

The two B-p_{xy}-derived orbits in CrB_2 originate from two electron-like pockets with two copies each between the A- and the H-points of the Brillouin zone as inferred from the DFT calculations with cycloidal magnetic order. Brasse et al. also performed a non-magnetic calculation where single copies of the two pockets appear at the A-point. The doubling of the pockets and the shift along the A-H-direction is thereby caused by the lifting of the spin degeneracy and the direction of the magnetic ordering wave

Comp.	Ref.	Orbit	Band	f_{calc} (T)	f_{exp} (T)	$m^\star/m_\mathrm{e}$	$m_\mathrm{b}/m_\mathrm{e}$	λ
VB_2	Ch. 7	α_V	V-d	1350	1410	0.79	0.49	0.6
		β_V	V-d	106	102	0.182	0.126	0.4
CrB_2	Ref. [12]	α_Cr	Cr-d	(734)	308	1.22	0.93	(0.3)
		β_Cr	B-p_{xy}	1899	1608	0.86	0.37	1.3
		δ_Cr	B-p_{xy}	2452	1951	1.07	0.53	1.0
MnB_2	Ch.8	α_Mn	Mn-d	405	250	0.50	0.31	0.6
		β_Mn	Mn-d	490	340	0.64	0.42	0.5

Table 8.2: Summary of the dHvA results for VB_2, Cr_2, and MnB_2 from Chs. 7, 8 and Ref. [12]. Observed dHvA orbits along with their band origin, experimental and calculated frequencies, effective masses $m^\star$, band masses m_b, and upper bounds for electron phonon coupling constants λ are listed.

vector, respectively [12]. Inspection of the calculated band structures of (non-magnetic) VB_2 and (non-magnetic) CrB_2 reveals a close similarity where in CrB_2 the Fermi energy E_F is shifted upwards with respect to the bands by the additional electron of Cr compared to V. In CrB_2 the band 10, correspondingly identified for VB_2, does not cross E_F, but the two pockets at A of CrB_2 are essentially derived from the same bands as the pockets at A formed by bands 11 and 12 in VB_2 (Fig. 7.11). As cycloidal magnetic order in CrB_2 doubles and relocates them in the Brillouin zone, we now attribute the two pockets of orbits β_Cr and δ_Cr to corresponding pockets at the A-points in VB_2. Following similar arguments, there are analogies of CrB_2 and VB_2 also with MnB_2. As stated in Sec. 8.6, for MnB_2 the band structure calculations were performed with the unit cell doubled in c-direction in order to account for the AF-c state. This corresponds to a back-folding of the bands in the c-direction of reciprocal space. For this reason, electron pockets with B-p_{xy} character located at the zone boundary in VB_2 and CrB_2 are transferred to the Γ-point.
Experimentally, for VB_2 and MnB_2, only M-d-derived orbits have been observed with coupling constants λ of 0.4-0.6 (Table 8.2). The two orbits of CrB_2 that could be attributed to bands with B-p_{xy} contributions have significantly higher coupling constants λ of 1.0 and 1.3. This can be attributed to a high sensitivity of the strong bonds formed by the in-plane B-p_{xy} orbitals to the B-B binding length and to the light mass of B. Observation of dHvA orbits from B-p_{xy}-derived orbits in VB_2 and MnB_2

in future experiments would therefore be particularly interesting to study electron phonon coupling in the corresponding boron planes. In view of the relatively small values derived for *M*-d-attributed coupling constants in VB_2 and MnB_2 (0.4-0.6), we think that the small coupling constant of orbit α_{Cr} (0.3 in Ref. [12]) is indeed consistent with the Cr-d band, tentatively suggested in the same work. Following the analysis performed in the course of the present thesis, a B-p_{xy} band should have a more enhanced coupling constant by the above arguments.

For the following comparison with MgB_2 it is helpful to revisit a characteristic property of the electronic states in MB_2 at E_{F}: All bands at E_{F} in all the investigated transition metal diborides have a high *M*-d contribution independent from K-space direction and also independent from the magnetic order as inferred from the DFT calculations. Moreover, as a common feature of MB_2, the B-p_z states are pushed away from E_{F}. The contribution of B-p_{xy} orbitals to the states at E_{F} varies depending on band and K-space orientation. However, the calculations suggest that there are no "pure" B-p_{xy} states. A considerable *M*-d component is always present. Following this, we conclude that the electronic states at E_{F} for transition metal diborides can be characterized as *M*-d states with a varying B-p_{xy} contribution.

We now turn to a comparison of our findings with the isostructural compound MgB_2. In the light of the discovery of the superconducting transition temperature of T_{c} = 39 K in MgB_2 [16], the study of the nature of the electronic states of transition metal diborides at E_{F} is particularly interesting. This exceptionally high value of T_{c} for a conventional, phonon-mediated superconductor [148, 149] cannot solely be attributed to the light B masses raising the phonon frequency, which scales the transition temperature in conventional BCS theory [150]. Enormous effort has been devoted to the explanation of superconductivity in MgB_2 on grounds of its electronic structure [143, 151–153]. At the heart of the superconducting state of MgB_2, there is a peculiar interplay of two superconducting gaps [110, 154–157]. The two gaps arise from two different band systems at E_{F}, of which one system is derived from in-plane B-p_{xy} states (σ-bands) and the other from B-p_z states (π-bands) [158–160]. Hereby, the ionic character of the Mg^{2+} layers lowers energetically the π-bands relative to the σ-bands. This results in a considerable hole-doping of the σ-bands, where phonon coupling is strong [154]. Both band systems are almost pure, i. e. the admixture of the respective other state is very small. This

orthogonal character suppresses interband scattering which would otherwise strongly reduce T_c [161]. At the level of the Fermi surface, the two orthogonal band systems manifest themselves in four distinct sheets. Two of them belong to the σ-bands and form slightly warped cylinders along the Γ-A-axes of two-dimensional character. The two sheets formed by the π-bands resemble tubular networks extending perpendicularly to the cylinders in the Γ- and in the A-plane, respectively [159]. All four Fermi surface sheets are open. The orthogonality of the σ- and π-states leads to a very low dispersion of the σ-bands along the c-axis. This fact is reflected by the two-dimensionality of the corresponding cylindrical sheets of the Fermi surface. Similarly, the fact that all sheets are open and the absence of closed pockets of ellipsoidal shape can be regarded as a consequence of anisotropic dispersions of all bands at E_F and hence as a characteristic of the orthogonality of σ- and π-states. These features of the Fermi surface were confirmed in a series of dHvA experiments [137, 143, 145, 162]. Four σ-orbits stemming from the cylinders along Γ-A with electron phonon coupling strengths of $\lambda \sim 0.9$-1.2 and two π-orbits from the tubular networks with $\lambda \sim 0.3$-0.4 were observed [145]. The coupling constants were in very good quantitative accordance with theoretical predictions: Large electron phonon coupling was suggested for the partially filled σ-states due to the light B masses and the sensitivity of the strong covalent B-σ bonds to the B-B binding length. The B-π states have a metallic character [158, 159]. For this reason, they are less sensitive to phonons than the σ-states. Consistently their coupling constants were found to be smaller by a factor of ~ 3 compared to the σ-states [143, 145, 152].

Comparing all values for λ of the transition metal diborides in Table 8.2 to the coupling constants for MgB_2 [145], we find an accordance of two scales for λ: The M-d states in MB_2 and π-states in MgB_2 share a similar (relatively low) scale for λ of 0.3-0.6 and 0.3-0.4, respectively. In contrast, for the states with a large in-plane B-p_{xy} component in MB_2 and for the σ-states in MgB_2, λ is enhanced to 1.0-1.3 and 0.9-1.2, respectively.

While the accordance of the two scales for states with and without B-p_{xy} contributions represents a similarity in MB_2 and MgB_2, there are profound differences of the electronic nature of the states at E_F. Most importantly, the transition metal contributes $3d$-electrons, which are absent in MgB_2, and all bands at E_F are M-d states with a varying B-p_{xy} contribution. Particularly, they do not possess the orthogonality of the rather pure σ-bands (from B-p_{xy}) and π-bands (from B-p_z) of MgB_2. This results in

a common characteristic of the Fermi surfaces of the three $M\mathrm{B}_2$ compared to MgB_2: They lack quasi-two-dimensional surface sheets (cf. Sec. 2.5) like the cylinders along Γ-A in MgB_2. Instead all of them feature pockets of ellipsoidal or spherical shape with a more isotropic, three-dimensional character and closed sheets. In fact, all orbits in Table 8.2 are attributed to closed sheets except β_{V}, i. e. closed sheets have been observed for all representative $M\mathrm{B}_2$ compounds. In contrast, MgB_2 exhibits only open sheets. In summary, the transition metal diborides $M\mathrm{B}_2$ share similar scales for the coupling constant λ with MgB_2 depending on whether or not B-p_{xy} orbitals contribute to the respective bands. However, the nature of electronic states at E_{F} in MgB_2 and $M\mathrm{B}_2$ differs profoundly. In MgB_2, the orthogonality of the states gives rise to quasi-two-dimensional sheets of the Fermi surface while in $M\mathrm{B}_2$ the ever-present M-d contributions render the surface more isotropic.

9 Summary and outlook

In this work, we studied the magnetization of three materials: graphene, VB_2, and MnB_2. Additionally, we designed and implemented a new experimental setup for torque cantilever magnetometry with optical readout to be used in a vacuum loading ^{3}He system.
Torque cantilever magnetometry was employed to investigate the magnetization of samples of the three different materials at low temperatures and in high magnetic fields. We designed, fabricated, and used two types of micromechanical cantilever magnetometers (MCMs), one based on GaAs cantilever sensors, the other based on CuBe cantilever sensors, in order to account for the specific properties of the respective material and the particular experimental conditions. The mechanical properties of the CuBe cantilever sensors were analyzed in detail to allow for a correct interpretation of the experimental data. The MCMs were mounted in vacuum loading ^{3}He systems to provide temperatures as low as 0.28 K and up to 20 K with precise control. Magnetic fields of up to 14 T and 15 T were provided by two superconducting solenoids. The 15 T-magnet was set up in the framework of this thesis.
In the following, we give separate summaries of the results of the four main parts of this thesis and include a brief outlook.

Magnetization experiments on large-area graphene samples

Magnetization experiments with GaAs-based micromechanical sensors were performed on five different types of large-area graphene samples: CVD-grown graphene monolithically integrated with the GaAs-based MCM, CVD-grown graphene on a Si substrate with a thermal SiO_2 layer, epitaxial monolayer graphene (MLG) on the Si-terminated side of 6H-SiC of two differing thicknesses, quasi-free-standing monolayer graphene (QFMLG) with an intercalated hydrogen layer on the Si-terminated side of 6H-SiC. None of the approaches provided a signal that could be attributed to the respective graphene layer. To date, large-area graphene samples are not

provided with an electronic quality and sample homogeneity sufficient for the observation of magnetic quantum oscillations of the graphene electron system. Electron mobility and sample homogeneity fall short of the respective parameters achieved in 2DESs in semiconductor heterostructures, where the de Haas-van Alphen effect is routinely observed, by several orders of magnitude. Existing growth processes of graphene will likely advance and new fabrication methods might emerge, which could ultimately lead to large-scale graphene samples of sufficient quality to study the orbital magnetism of graphene. An alternative tantalizing route is the study of a single exfoliated graphene flake by means of cantilever torque magnetometry, but the path to this experiment is fraught with immense challenges, such as cleavage of a sufficiently large graphene flake with satisfactory mobility, development of dedicated sensor technology and integration of favorable graphene substrates (e. g. hexagonal boron nitride) in the sensor, development of techniques for transferring flakes and appropriate substrates onto the sensors, protection of the sensor/sample combination from deteriorating environment influences, techniques for in-situ annealing of the sample, development of a suitable readout technique, damping of the micromechanical sensor, et cetera. During the research for this thesis, we became aware of an interesting variation of the suggested MCM experiment on individual exfoliated graphene flakes. Changyao Chen presents in his thesis measurements in the quantum Hall regime of a graphene resonator formed by a suspended flake, which had directly been exfoliated on elevated source and drain electrodes with a local gate electrode patterned in a trench between them, using a capacitive readout with balanced background. Thus, the graphene flake acts as the embedded 2DES and the mechanical resonator simultaneously. A strong magneto-mechanical coupling to dHvA oscillations of the Dirac electron gas was observed [163].

Sample head for cantilever magnetometry with interferometric readout

We designed, implemented, and tested a new experimental sample head used in a vacuum loading ^{3}He system for cantilever magnetometry experiments using an interferometric readout scheme. We presented the guidelines along which the sample head was developed, such as integration into an existing ^{3}He system and use in existing superconducting solenoids,

sample fine-positioning considerations, wiring challenges for experiments at cryogenic temperatures, and access issues in experimental environments with limited space. We showed how these design challenges were successfully addressed in the implementation. The sample head was tested and will allow for highly sensitive magnetization experiments with submicrometer control of the sample position. This opens the possibility of experiments with cantilevers having lateral dimensions on the micrometer scale, carrying samples, e. g. single crystal specimen, which require higher magnetometric sensitivities than presently available.

De Haas-van Alphen effect and Fermi surface properties of VB_2

The angular, temperature, and field dependence of the dHvA effect of VB_2 was studied in all three major planes of the $C32$ crystal structure. We identified two distinct extremal orbits α and β of the Fermi surface. The experiment suggests that orbit α, having an average frequency of $f_{\alpha,\mathrm{av}} = 1410\,\mathrm{T}$, stems from a closed surface sheet while β is an open orbit with a minimal frequency of $f_{\beta,\mathrm{min}} = 102\,\mathrm{T}$. The Lifshitz-Kosevich analysis of temperature and field dependence revealed effective masses of $m^\star_\alpha = 0.79\,m_\mathrm{e}$ and $m^\star_\beta = 0.182\,m_\mathrm{e}$ and free mean paths of $l_\alpha = 25\,\mathrm{nm}$ and $l_\beta = 21\,\mathrm{nm}$, respectively. The experimental results were compared to data extracted from brand structure calculations. Orbit α could be attributed to a Fermi surface feature with a tear drop-like form and orbit β was found to originate from a thin capillary at the zone boundary formed by complicated open surface sheets of neighboring Brillouin zones. The electronic states of both orbits have predominantly V-d character. Orbit α is electron-like and orbit β is hole-like. Comparison of the measured effective masses $m^\star$ with the band masses m_b extracted from the calculations yielded mass enhancement factors of 1.6 and 1.4 and accordingly upper bounds for the electron phonon coupling constants of 0.6 and 0.4. Experimental observations of the relative dHvA signal strengths for different orientations could be consistently explained by curvature and anisotropy data of the extremal orbits as obtained from the calculations. To the best of our knowledge, our experiments represent the first detailed study of the angular dependence of the dHvA effect of VB_2. In particular, the observation of orbit β had not been reported before.
In the experiments conducted for this thesis, we were limited to tempera-

tures greater than 280 mK and magnetic fields up to 15 T. The band structure calculations suggest the existence of numerous dHvA orbits which have not been observed. All of them have either larger band masses or higher frequencies than the found orbits. The experimental limitations make their observation thus less likely. Two spherical pockets predicted by the calculations are particularly interesting in that they possess the highest contribution of B-p_{xy} states of all extracted extremal orbits. Their observation in consecutive experiments at higher fields and lower temperatures would thus allow for a comparison of electron phonon coupling constants of B-p_{xy}- and V-d-derived states in VB_2 and with the respective parameters in isostructural compounds. As the two orbits from B-p_{xy}-derived pockets have only slightly higher frequencies than α and even lower band masses, we have reason to speculate that their observation is just "right around the corner"

De Haas-van Alphen effect and Fermi surface properties of MnB_2

The angular, temperature, and field dependence of the dHvA effect of MnB_2 was studied in the basal plane of the $C32$ crystal structure. We identified two distinct extremal orbits α and β of the Fermi surface. The experiment suggests that both orbits stem from closed surface sheets. Orbit α, having an average frequency of $f_{\alpha,\mathrm{av}} = 250\,\mathrm{T}$, and orbit β with an average frequency of $f_{\beta,\mathrm{av}} = 340\,\mathrm{T}$ showed a periodic frequency variation when the field was rotated in the basal plane consistent with the crystal symmetry. More precisely, an anti-phase behavior of α and β with respect to the frequency dependence was observed. The Lifshitz-Kosevich analysis of temperature and field dependence revealed effective masses of $m^\star_\alpha = 0.50\,m_\mathrm{e}$ and $m^\star_\beta = 0.64\,m_\mathrm{e}$, respectively, and for β a free mean path of $l_\beta = 48\,\mathrm{nm}$. The experimental results were compared to data extracted from brand structure calculations considering the antiferromagnetic AF-c ground state of MnB_2, but neglecting the canting of localized moments towards the c-axis. Both orbits could be attributed to a Fermi surface sheet at the Brillouin zone boundary resembling a torus with horn-like protrusions. The anti-phase behavior of the angular frequency dependence could be explained by a variation of the two identical minimal cross sections of a simple torus by the addition of the horns. Both orbits are hole-like and originate from bands having predominantly Mn-d character.

Comparison of the measured effective masses $m^\star$ with the band masses m_b extracted from the calculations yielded mass enhancement factors of 1.6 and 1.5 and accordingly upper bounds for the electron phonon coupling constants of 0.6 and 0.5. The dHvA signal strength of frequency f_β was larger than the one of f_α, a fact found to be consistent with a higher anisotropy of the extremal area of orbit β compared to orbit α as inferred from the calculations. We thus found a good agreement of the experimental results with the predictions from band structure calculations assuming the AF-c state. To the best of our knowledge, our investigation is the first dHvA study of MnB_2.
Similarly to VB_2, the calculations suggest the existence of a variety of other dHvA orbits, which have not been observed in the experiments. According to the calculations, all of them have larger band masses or higher frequencies than the found orbits. Experimental limitations of finite temperature and magnetic fields would thus lead to a reduction of the relative strength of their dHvA signals. Future experiments in higher magnetic fields and/or at lower temperatures, e. g. in a ^{3}He/^{4}He dilution refrigerator, might allow for the exploration of orbits with heavier masses and higher frequencies. In particular, the existence of two electron-like pockets is predicted with a considerably higher contribution of B-p_{xy} states than in the observed orbits. Their observation would be particularly interesting in order to derive useful quantitative information on many-body interactions in MnB_2, particularly the electron phonon coupling of B-p_{xy}-derived states. Additionally, the observation of more orbits would allow for a more rigorous test of the calculated Fermi surface properties. It is well established that the magnetic ground state of MnB_2 is characterized by a slight canting of the AF-c ordered magnetic moments. A finite canting angle lifts the degeneracy of the band structure with respect to spin projection, resulting in a splitting of the bands for majority and minority charge carriers. The splitting of the bands could be observed in dHvA experiments and the band structure calculations could be revisited considering a finite canting angle. By comparison of such experimental and theoretical data, valuable information on the canting angle could be derived and ultimately lead to a better understanding of the peculiar nature of MnB_2 magnetism.

A detailed comparison of the experimental results for VB_2 and MnB_2 and of the inferences about the nature of the electronic states and Fermi surface properties of VB_2 and MnB_2 with a dHvA investigation of the transition

metal diboride CrB_2 [12] and with various studies of the isostructural rare earth metal diboride MgB_2 was included. In this synoptic discussion, we argued that the electronic states at the Fermi energy in all transition metal (M) diborides VB_2, CrB_2, and MnB_2 predominantly have M-d character with a varying contribution from B-p_{xy} orbitals. Hereby, the upper bound of the electron phonon coupling constant for comparatively pure M-d states is 0.4-0.6 while the states with considerable B-p_{xy} contributions have an enhanced coupling constant of 1.0-1.3. Even though the three compounds have different magnetic ground states, the electron pockets in the three Fermi surfaces with large B-p_{xy} contributions could be traced to the same origin in the band structure.
In comparison with MgB_2, we found that the transition metal diborides MB_2 share similar scales for the electron coupling constant with MgB_2 depending on whether or not B-p_{xy} orbitals contribute to the respective bands. However, the nature of electronic states at the Fermi energy in MgB_2 and MB_2 differs profoundly. The rare earth compound MgB_2 lacks $3d$-electrons. The Fermi surface is characterized by two band systems σ and π, derived from B-p_{xy} and B-p_z orbitals, respectively, with a high degree of orthogonality. This orthogonality of the states gives rise to quasi-two-dimensional sheets of the Fermi surface and explains the lack of closed sheets. In contrast, the ever-present M-d contributions to the electronic states in the transition metal diborides render the Fermi surface more isotropic and closed Fermi surface sheets of ellipsoidal or spherical shape were found for all representative MB_2 compounds both in experiments and calculations.

A Details of electronic structure calculations for VB_2 and MnB_2

In this appendix, details of the electronic structure calculations for VB_2 and MnB_2 are presented in order to substantiate the statements in the main text about the atomic origin of the various bands of the compounds and in particular of the bands at the Fermi Energy E_{F} constituting the Fermi surface and the dHvA orbits.

A.1 Atomic orbital origin of VB_2 band structure

For the discussion of the origin of the VB_2 bands from atomic orbitals, we refer to Fig. A.1 for illustration. Figure A.1 depicts the electronic band structure of VB_2 for high-symmetry directions in K-space as inferred from density functional theory calculations performed by J. Kuneš. In the corresponding energy range, it is identical to Fig. 7.9. Figure A.1 (a) illustrates the contributions from B-p orbitals. The radii of black (red) circles indicate the degree of B-p_{xy} (B-p_z) contributions. The out-of-plane B-p_z states are pushed away from E_{F}, by convention at zero energy. This is a common feature of transition metal diborides. At E_{F} the B-p_z contributions are small for all bands. In contrast, the in-plane B-p_{xy} contributions at E_{F} vary depending on band and K-space orientation. As can be seen from Fig. A.1 (a), the B-p_{xy} contribution at E_{F} is largest for the two bands crossing E_{F} in the proximity of the A-point. These two bands (labelled 11 and 12 in Ch. 7) give rise to the ellipsoidal and the spherical Fermi surface sheet at the A-point (cf. Figs. 7.11 (b,c)) discussed in Ch. 7. Figure A.1 (b) illustrates the contribution from V-d orbitals. All bands at E_{F} have a high degree of V-d components. In this sense, the electronic states at E_{F} can be essentially characterized as V-d states with a varying B-p_{xy} contribution.
In Figs. A.1 (a,b), we have indicated the positions of the experimentally observed orbits α and β, which stem from a tear drop-like electron pocket half-way between Γ and the A-point (Fig. 7.11 (b)) and capillaries at the K-point (Figs. 7.11 (a) and 7.14). The bubble plot Fig. A.1 (a) suggests

that neither of the two has substantial B-p_{xy} components compared to the pockets at the A-points. In this sense, the character of orbits α and β is described as V-d type in Ch. 7.

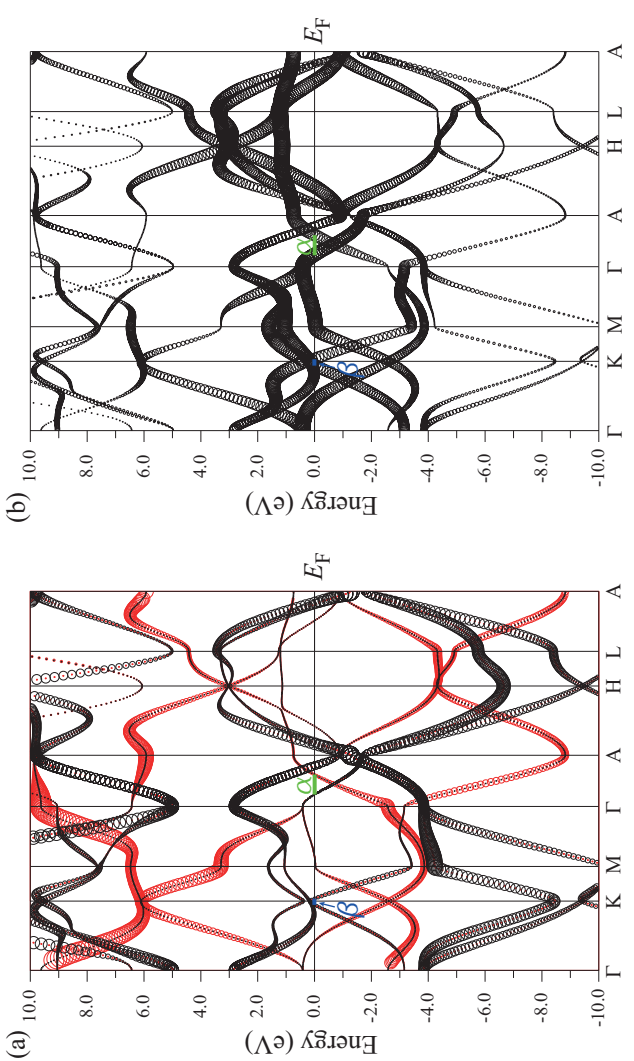

Figure A.1: Band structure of VB_2 for high-symmetry directions in K-space with circle radius indicating the atomic orbital character. (a) B-p character. The radii of black (red) circles indicate the degree of B-p_{xy} (B-p_z) contributions. (b) Radii indicate V-d character. The electronic states at E_F can be characterized as V-d states with a varying B-p_{xy} contribution depending on band and K-space orientation. Experimentally observed dHvA orbits α and β are indicated in (a) and (b). They have V-d character. Figure provided by J. Kuneš and adapted by the present author.

A.2 Atomic orbital origin of MnB_2 band structure

For the discussion of the origin of the MnB_2 bands from atomic orbitals, we refer to Fig. A.2 for illustration. Figure A.2 depicts the electronic band structure of MnB_2 for high-symmetry directions in K-space as inferred from density functional theory calculations performed by J. Kuneš. In the corresponding energy range it is identical to Fig. 8.7. As the AF-c order of MnB_2 doubles the unit cell in real space, which corresponds to a back-folding of bands along the c-direction, twice as many bands are present compared to Fig. A.1. Figure A.2 (a) illustrates the contributions from B-p orbitals. The radii of black (red) circles indicate the degree of B-p_{xy} (B-p_z) contributions. Similarly to VB_2 and other transition metal diborides, the out-of-plane B-p_z states are pushed away from E_F, by convention at zero energy. The states with considerable B-p_{xy} character are centered around Γ. This is a consequence of the back-folding. In VB_2 and CrB_2, they are at the zone boundary. More precisely, in VB_2 and non-magnetic CrB_2 [12] they are located around the A-point and in cycloidally ordered CrB_2 they are shifted along the A-H-line [12]. Figure A.2 (b) illustrates the contribution from Mn-d orbitals. The color labels relate to the electron spin projection (red = up, black = down) with respect to an arbitrary Mn atom Mn1. For a second Mn atom in a neighboring hexagonal plane, Mn2, i. e. with opposite polarization, the labelling would be reversed, thus restoring the symmetry of the band structure with respect to spin projection. Independent from this, all bands at E_F have a high degree of Mn-d components. In this sense, the electronic states at E_F can be essentially characterized as Mn-d states with a varying B-p_{xy} contribution.
In Figs. A.2 (a,b) we have indicated the positions of the experimentally observed orbits α and β, which stem from the two small cross sections of the tori at the H-points (Fig. 8.10) as discussed in Ch. 8. The bubble plot Fig. A.2 (a) suggests that neither of the two has substantial B-p_{xy} components compared to the Γ-centered pockets. In this sense, the character of orbits α and β is described as Mn-d type in Ch. 8.

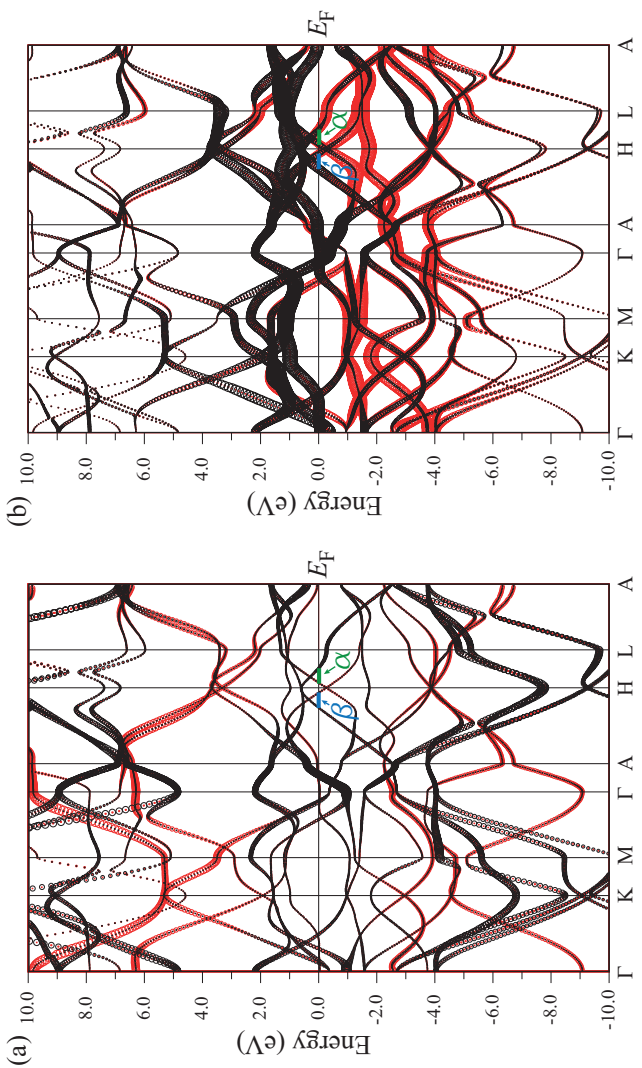

Figure A.2: Band structure of MnB_2 for high-symmetry directions in K-space with circle radius indicating the atomic orbital character. (a) B-p character. The radii of black (red) circles indicate the degree of B-p_{xy} (B-p_z) contributions. (b) Radii indicate Mn-d character. The color labels relate to the electron spin projection with respect to an arbitrary Mn atom Mn1. For a second Mn atom Mn2 they would be reversed. The electronic states at E_F can be characterized as Mn-d states with a varying B-p_{xy} contribution depending on band and K-space orientation. Experimentally observed dHvA orbits α and β are indicated in (a) and (b). They have Mn-d character. Figure provided by J. Kuneš and adapted by the present author.

B Supplementary results from de Haas-van Alphen frequency calculations for MnB_2

In this appendix, we report the dHvA frequencies extracted from the band structure calculations for MnB_2 using the SKEAF tool [141] corresponding to rotations of the magnetic field $\mathbf{B}$ in the $[001]$-$[100]$-plane and in the $[001]$-$[120]$-plane. Hereby, the conventions used for the angles ϑ and ψ coincide with the ones used for VB_2 as defined in Fig. 7.1 and Fig. 7.11 (d). Figs. B.1 (a-d) show the resulting dHvA frequencies versus the respective angles ϑ and ψ where the left column of subfigures (a,c) shows the frequencies for the $[001]$-$[100]$-plane and the right column of subfigures (b,d) shows the frequencies for the $[001]$-$[120]$-plane. The first row of subfigures (a,b) corresponds to the Fermi surface sheet arising from band 21 as depicted in Fig. 8.9 (a) and Fig. 8.10 while the second row of subfigures (c,d) summarizes the frequencies arising from the Fermi surface sheets of bands 22-24 as depicted in Figs. 8.9 (b-d). DHvA frequencies stemming from band 22 are represented by squares $\square$, frequencies from band 23 are represented by triangles $\triangle$, and frequencies from band 24 are represented by diamonds $\diamond$.

In Figs. B.1 (a,b), two dHvA frequencies are found for $\vartheta = \psi = 0$, which corresponds to $\mathbf{B}$ oriented along the c-axis. In the model of the simple torus (cf. Fig. 8.12), they correspond to the inner and outer circle of the torus when viewed from above. The orientations of $\mathbf{B}$ corresponding to $\vartheta = 90°$ and $\psi = 90°$ are identical to $\varphi = 30°$ and $\varphi = 0°$, respectively, when $\mathbf{B}$ is rotated in the basal plane. Consequently, we recover the same three frequencies at these angles as in Fig. 8.11 (a). These directions are the high-symmetry directions where the two maximal cross sections of the horned torus ($\vartheta = 90°$) or the two minimal cross sections of the horned torus ($\psi = 90°$) are identical. For angle values of ϑ and ψ between $0°$ and $90°$, a transition from the situation where the inner and outer circle of the torus constitute the extremal orbits to the situation discussed in Sec. 8.7 should obviously be found and this is reflected in Figs. B.1 (a,b).

In Figs. B.1 (c,d), the dependencies of the dHvA frequencies arising from

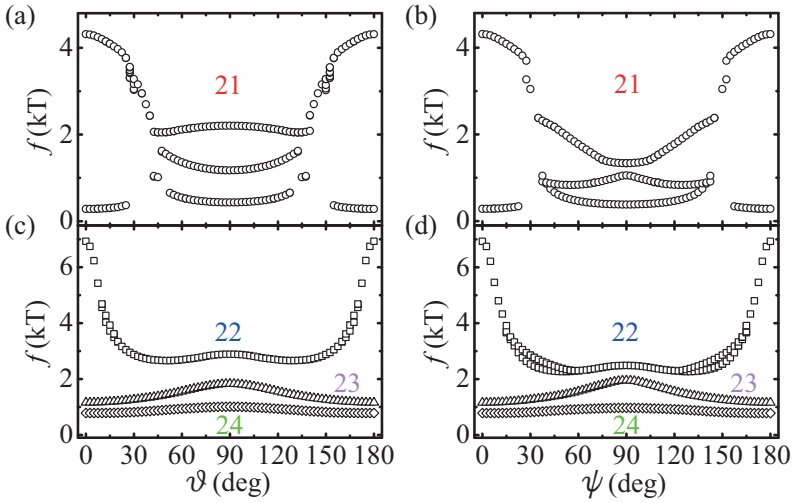

Figure B.1: Angular dependence of dHvA frequencies of extremal orbits versus angle ϑ and ψ for rotations of $\mathbf{B}$ in the [001]-[100] plane (left column) and in the [001]-[120] plane (right column), respectively, as extracted from the band structure for MnB_2 calculations using the SKEAF tool [141]. (a,b) Angular dependence of extremal orbits of band 21 corresponding to the surface sheet in Fig. 8.9 (a) or Fig. 8.10, respectively. (c,d) Angular dependence of extremal orbits of bands 22-24. DHvA frequencies from band 22 are represented by squares □, frequencies from band 23 are represented by triangles △, and frequencies from band 24 are represented by diamonds ◇.

Fermi surface sheets 22, 23, and 24 are similar for ϑ and ψ. The frequency from the spinning top sheet 22 is relatively high (6.9 kT) for $\mathbf{B} \parallel \mathbf{c}$, i. e. $\vartheta = \psi = 0°$. When $\mathbf{B}$ tilts away from the c-axis, it decreases to values between 2 kT and 3 kT when the extremal area "leaves" the broadened surface region of the spinning top in the basal plane (cf. Fig. 8.9 (b)). The extremal cross sections from Fermi surface sheet 23 show a frequency variation as a function of ϑ and ψ corresponding to the ellipsoidal shape of the sheet while the nearly spherical sheet 24 leads to a frequency branch with a relatively small variation.

List of abbreviations

abbreviation	explicit
2DES	two-dimensional electron system
AFM	atomic force microscopy/microscope
Al_2O_3	aluminium oxide
AuPd	gold palladium
CrB_2	chromium diboride
CuBe	copper beryllium
CVD	chemical vapor deposition
DFT	density functional theory
dHvA	de Haas-van Alphen
DOS	density of states
$FeCl_3$	iron chloride
FFT	fast Fourier transform
GaAs	gallium arsenide
HfB_2	hafnium diboride
IVC	inner vacuum chamber
MCM	micromechanical cantilever magnetometer
MgB_2	magnesium diboride
MgZnO	magnesium zinc oxide
MLG	monolayer graphene
MnB_2	manganese diboride
QFMLG	quasi-free-standing monolayer graphene
ScB_2	scandium diboride
SiC	silicon carbide
SKEAF	Supercell K-space Extremal Area Finder
TiB_2	titanium diboride
VB_2	vanadium diboride
ZnO	zinc oxide
ZrB_2	zirconium diboride

List of figures

List of tables

Bibliography

[1] G. E. Moore: Cramming More Components onto Integrated Circuits Electronics. *Electronics* **38**, 114 (1965).

[2] J. D. Meindl, Q. Chen, and J. A. Davis: Limits on Silicon Nanoelectronics for Terascale Integration. *Science* **293**, 2044 (2001).

[3] R. Keyes: Fundamental limits of silicon technology. *Proceedings of the IEEE* **89**, 227 (2001).

[4] K. S. Novoselov, A. K. Geim, S. V. Morozov, D. Jiang, Y. Zhang, S. V. Dubonos, I. V. Grigorieva, and A. A. Firsov: Electric Field Effect in Atomically Thin Carbon Films. *Science* **306**, 666 (2004).

[5] C. Berger, Z. Song, T. Li, X. Li, A. Y. Ogbazghi, R. Feng, Z. Dai, A. N. Marchenkov, E. H. Conrad, P. N. First, and W. A. de Heer: Ultrathin Epitaxial Graphite: 2D Electron Gas Properties and a Route toward Graphene-based Nanoelectronics. *The Journal of Physical Chemistry B* **108**, 19912 (2004).

[6] X. Li, W. Cai, J. An, S. Kim, J. Nah, D. Yang, R. Piner, A. Velamakanni, I. Jung, E. Tutuc, S. K. Banerjee, L. Colombo, and R. S. Ruoff: Large-Area Synthesis of High-Quality and Uniform Graphene Films on Copper Foils. *Science* **324**, 1312 (2009).

[7] A. K. Geim and K. S. Novoselov: The rise of graphene. *Nature materials* **6**, 183 (2007).

[8] Graphene Flagship. Website. Online available at `http://graphene-flagship.eu/`; accessed Jan, 12th 2015.

[9] K. S. Novoselov, V. Fal'ko, L. Colombo, P. Gellert, M. Schwab, and K. Kim: A roadmap for graphene. *Nature* **490**, 192 (2012).

[10] M. Y. Han, B. Özyilmaz, Y. Zhang, and P. Kim: Energy Band-Gap Engineering of Graphene Nanoribbons. *Physical Review Letters* **98**, 206805 (2007).

[11] L. Britnell, R. V. Gorbachev, R. Jalil, B. D. Belle, F. Schedin, A. Mishchenko, T. Georgiou, M. I. Katsnelson, L. Eaves, S. V. Morozov, N. M. R. Peres, J. Leist, A. K. Geim, K. S. Novoselov, and L. A. Ponomarenko: Field-Effect Tunneling Transistor Based on Vertical Graphene Heterostructures. *Science* **335**, 947 (2012).

[12] M. Brasse, L. Chioncel, J. Kuneš, A. Bauer, A. Regnat, C. G. F. Blum, S. Wurmehl, C. Pfleiderer, M. A. Wilde, and D. Grundler: de Haas-van Alphen effect and Fermi surface properties of single-crystal CrB_2. *Physical Review B* **88**, 155138 (2013).

[13] A. Bauer, A. Regnat, C. G. F. Blum, S. Gottlieb-Schönmeyer, B. Pedersen, M. Meven, S. Wurmehl, J. Kuneš, and C. Pfleiderer: Low-temperature properties of single-crystal CrB_2. *Physical Review B* **90**, 064414 (2014).

[14] M. Kasaya and T. Hihara: Magnetic Structure of MnB_2. *Journal of the Physical Society of Japan* **29**, 336 (1970).

[15] S. Funahashi, Y. Hamaguchi, T. Tanaka, and E. Bannai: Helical magnetic structure in CrB_2. *Solid State Communications* **23**, 859 (1977).

[16] J. Nagamatsu, N. Nakagawa, T. Muranaka, Y. Zenitani, and J. Akimitsu: Superconductivity at 39 K in magnesium diboride. *Nature* **410**, 63 (2001).

[17] W. de Haas and P. van Alphen: The dependence of the susceptibility of diamagnetic metals upon the field. In: *Proceedings of the Academy of Science of Amsterdam*, vol. 33, pp. 1106–1118 (1930).

[18] F. Schwabl: *Quantenmechanik*. Springer (1998).

[19] J. J. Sakurai and S. F. Tuan: *Modern quantum mechanics*. Addison-Wesley Reading (1985).

[20] D. Shoenberg: *Magnetic oscillations in metals*. Cambridge University Press (1984).

[21] L. Onsager: Interpretation of the de Haas-van Alphen effect. *Philosophical Magazine* **43**, 1006 (1952).

[22] L. Landau and E. Lifshitz: *Statistical Physics Part 1*. Pergamon Press (1980).

[23] F. Schwabl: *Statistische Mechanik*. Springer (2006).

[24] S. Engelsberg and G. Simpson: Influence of Electron-Phonon Interactions on the de Haas-van Alphen Effect. *Physical Review B* **2**, 1657 (1970).

[25] C. J. Palin: Amplitude of the De Haas-Van Alphen Effect in Mercury. *Proceedings of the Royal Society of London A: Mathematical, Physical and Engineering Sciences* **329**, 17 (1972).

[26] R. B. Dingle: Some Magnetic Properties of Metals. II. The Influence of Collisions on the Magnetic Behaviour of Large Systems. *Proceedings of the Royal Society of London A: Mathematical, Physical and Engineering Sciences* **211**, 517 (1952).

[27] I. M. Lifschitz and A. M. Kosevich: On the theory of the de Haas-van Alphen effect for particles with an arbitrary dispersion law. In: *Doklady Akademii Nauk SSSR*, vol. 96, p. 963 (1954).

[28] I. M. Lifshitz and A. M. Kosevich: Theory of magnetic susceptibility in metals at low temperatures. *Soviet Physics - JETP* **2**, 636 (1956).

[29] D. Shoenberg and P. J. Stiles: The de Haas-Van Alphen Effect in Alkali Metals. *Proceedings of the Royal Society of London A: Mathematical, Physical and Engineering Sciences* **281**, 62 (1964).

[30] L. Windmiller: de Haas-van Alphen Effect and Fermi Surface in Antimony. *Physical Review* **149**, 472 (1966).

[31] A. Goldstein, S. J. Williamson, and S. Foner: Low Frequency Field Modulation Differential Magnetometer; Applications to the De Haas-Van Alphen Effect. *Review of Scientific Instruments* **36**, 1356 (1965).

[32] R. Stark and L. Windmiller: Theory and technology for measuring the de Haas-van Alphen type spectra in metal. *Cryogenics* **8**, 272 (1968).

[33] L. R. Windmiller and J. B. Ketterson: Techniques and Instrumentation for Measuring the de Haas-van Alphen Effect in Metals. *Review of Scientific Instruments* **39**, 1672 (1968).

[34] M. Priestley: Pulsed-Field de Haas-van Alphen Effect in Thallium. *Physical Review* **148**, 580 (1966).

[35] M. A. Wilde, D. Grundler, and D. Heitmann: Magnetization of Interacting Electrons. In: D. Heitmann (Editor), *Quantum Materials*, chap. 10, p. 245. Springer (2010).

[36] G. A. Gibson and S. Schultz: Magnetic force microscope study of the micromagnetics of submicrometer magnetic particles. *Journal of Applied Physics* **73**, 4516 (1993).

[37] M. Willemin, C. Rossel, J. Brugger, M. H. Despont, H. Rothuizen, P. Vettiger, J. Hofer, and H. Keller: Piezoresistive cantilever designed for torque magnetometry. *Journal of Applied Physics* **83**, 1163 (1998).

[38] C. Lupien, B. Ellman, P. Grütter, and L. Taillefer: Piezoresistive torque magnetometry below 1 K. *Applied Physics Letters* **74**, 451 (1999).

[39] R. Griessen: A capacitance torquemeter for de Haas-van Alphen measurements. *Cryogenics* **13**, 375 (1973).

[40] M. Wilde: *Magnetization Measurements on Low-Dimensional Electron Systems in High-Mobility GaAs and SiGe Heterostructures*. Ph.D. thesis, Universität Hamburg (2004).

[41] H. Gross, W. Hauger, J. Schröder, and W. A. Wall: *Technische Mechanik 2*. Springer (2011).

[42] A. C. Ugural and S. K. Fenster: *Advanced Strength and Applied Elasticity, Fourth Edition*. Prentice Hall (2003).

[43] NGK-Berylco: Kupfer-Beryllium Legierung. Website (2014). Online available at `www.ngk-alloys.com/NGK_Berylco_Catalogue_D.pdf`; accessed Dec, 19th 2014.

[44] P. R. Wallace: The Band Theory of Graphite. *Physical Review* **71**, 622 (1947).

[45] J. W. McClure: Band Structure of Graphite and de Haas-van Alphen Effect. *Physical Review* **108**, 612 (1957).

[46] J. C. Slonczewski and P. R. Weiss: Band Structure of Graphite. *Physical Review* **109**, 272 (1958).

[47] N. D. Mermin: Crystalline Order in Two Dimensions. *Physical Review* **176**, 250 (1968).

[48] A. K. Geim: Graphene: Status and Prospects. *Science* **324**, 1530 (2009).

[49] A. H. Castro Neto, F. Guinea, N. M. R. Peres, K. S. Novoselov, and A. K. Geim: The electronic properties of graphene. *Reviews of Modern Physics* **81**, 109 (2009).

[50] F. Schwierz: Graphene transistors. *Nature nanotechnology* **5**, 487 (2010).

[51] M. S. Fuhrer, C. N. Lau, and A. H. MacDonald: Graphene: Materially Better Carbon. *MRS Bulletin* **35**, 289 (2010).

[52] S. Das Sarma, S. Adam, E. Hwang, and E. Rossi: Electronic transport in two-dimensional graphene. *Reviews of Modern Physics* **83**, 407 (2011).

[53] K. Novoselov, A. K. Geim, S. Morozov, D. Jiang, M. Katsnelson, I. Grigorieva, S. Dubonos, and A. Firsov: Two-dimensional gas of massless Dirac fermions in graphene. *Nature* **438**, 197 (2005).

[54] Y. Zhang, Y.-W. Tan, H. L. Stormer, and P. Kim: Experimental observation of the quantum Hall effect and Berry's phase in graphene. *Nature* **438**, 201 (2005).

[55] N. M. R. Peres, F. Guinea, and A. H. Castro Neto: Electronic properties of disordered two-dimensional carbon. *Physical Review B* **73**, 125411 (2006).

[56] L. Brey and H. A. Fertig: Edge states and the quantized Hall effect in graphene. *Physical Review B* **73**, 195408 (2006).

[57] L. Brey and H. A. Fertig: Electronic states of graphene nanoribbons studied with the Dirac equation. *Physical Review B* **73**, 235411 (2006).

[58] S. G. Sharapov, V. P. Gusynin, and H. Beck: Magnetic oscillations in planar systems with the Dirac-like spectrum of quasiparticle excitations. *Physical Review B* **69**, 075104 (2004).

[59] J. W. McClure: Diamagnetism of Graphite. *Physical Review* **104**, 666 (1956).

[60] O. Espinosa and V. H. Moll: A generalized polygamma function. *Integral Transforms and Special Functions* **15**, 101 (2004).

[61] J. Choi: Finite summation formulas involving binomial coefficients, harmonic numbers and generalized harmonic numbers. *Journal of Inequalities and Applications* **2013**, 49 (2013).

[62] J. Jobst, D. Waldmann, F. Speck, R. Hirner, D. K. Maude, T. Seyller, and H. B. Weber: Quantum oscillations and quantum Hall effect in epitaxial graphene. *Physical Review B* **81**, 195434 (2010).

[63] J. Jobst, D. Waldmann, F. Speck, R. Hirner, D. K. Maude, T. Seyller, and H. B. Weber: Transport properties of high-quality epitaxial graphene on 6H-SiC(0001). *Solid State Communications* **151**, 1061 (2011).

[64] A. K. Mlynarski: *Characterization of Electric and Magnetic Properties of Chemical-Vapour Deposited Few-Layer Graphene*. Diploma thesis (unpublished), Technische Universität München (2011).

[65] L. H. Hess, M. V. Hauf, M. Seifert, F. Speck, T. Seyller, M. Stutzmann, I. D. Sharp, and J. A. Garrido: High-transconductance graphene solution-gated field effect transistors. *Applied Physics Letters* **99**, 033503 (2011).

[66] S.-H. Chalkidis: *Anomalous magnetic oscillations observed on epitaxial graphene*. Diploma thesis (unpublished), Technische Universität München (2012).

[67] M. Block: *An Approach for Magnetization Measurements on Dirac Fermions*. Master thesis (unpublished), Technische Universität München (2013).

[68] F. Speck, J. Jobst, F. Fromm, M. Ostler, D. Waldmann, M. Hundhausen, H. B. Weber, and T. Seyller: The quasi-free-standing nature of graphene on H-saturated SiC(0001). *Applied Physics Letters* **99**, 122106 (2011).

[69] F. Fromm: private communication (Lehrstuhl für Technische Physik, Friedrich-Alexander-Universität Erlangen-Nürnberg, presently at Technische Universität Chemnitz).

[70] M. P. Schwarz, D. Grundler, I. Meinel, C. Heyn, and D. Heitmann: Micromechanical cantilever magnetometer with an integrated two-dimensional electron system. *Applied Physics Letters* **76**, 3564 (2000).

[71] M. Brasse: *Magnetization of correlated electron systems: MnSi thin films, CrB_2 single crystals and two-dimensional electron systems in MgZnO/ZnO*. Ph.D. thesis, Technische Universität München (2014).

[72] C. Berger, Z. Song, X. Li, X. Wu, N. Brown, C. Naud, D. Mayou, T. Li, J. Hass, A. N. Marchenkov, E. H. Conrad, P. N. First, and W. A. de Heer: Electronic Confinement and Coherence in Patterned Epitaxial Graphene. *Science* **312**, 1191 (2006).

[73] W. A. de Heer, C. Berger, X. Wu, P. N. First, E. H. Conrad, X. Li, T. Li, M. Sprinkle, J. Hass, M. L. Sadowski, M. Potemski, and G. Martinez: Epitaxial graphene. *Solid State Communications* **143**, 92 (2007).

[74] C. Virojanadara, M. Syväjarvi, R. Yakimova, L. I. Johansson, A. A. Zakharov, and T. Balasubramanian: Homogeneous large-area graphene layer growth on $6H$-SiC(0001). *Physical Review B* **78**, 245403 (2008).

[75] Y.-M. Lin, C. Dimitrakopoulos, K. A. Jenkins, D. B. Farmer, H.-Y. Chiu, A. Grill, and P. Avouris: 100-GHz Transistors from Wafer-Scale Epitaxial Graphene. *Science* **327**, 662 (2010).

[76] T. Seyller, A. Bostwick, K. V. Emtsev, K. Horn, L. Ley, J. L. McChesney, T. Ohta, J. D. Riley, E. Rotenberg, and F. Speck: Epitaxial graphene: a new material. *physica status solidi (b)* **245**, 1436 (2008).

[77] C. Riedl, C. Coletti, and U. Starke: Structural and electronic properties of epitaxial graphene on SiC(0001): a review of growth, characterization, transfer doping and hydrogen intercalation. *Journal of Physics D: Applied Physics* **43**, 374009 (2010).

[78] P. N. First, W. A. de Heer, T. Seyller, C. Berger, J. A. Stroscio, and J.-S. Moon: Epitaxial Graphenes on Silicon Carbide. *MRS Bulletin* **35**, 296 (2010).

[79] T. Seyller, K. Emtsev, K. Gao, F. Speck, L. Ley, A. Tadich, L. Broekman, J. Riley, R. Leckey, O. Rader, A. Varykhalov, and A. Shikin: Structural and electronic properties of graphite layers grown on SiC(0001). *Surface Science* **600**, 3906 (2006).

[80] K. V. Emtsev, F. Speck, T. Seyller, L. Ley, and J. D. Riley: Interaction, growth, and ordering of epitaxial graphene on SiC0001 surfaces: A comparative photoelectron spectroscopy study. *Physical Review B* **77**, 155303 (2008).

[81] J. Hass, W. A. de Heer, and E. H. Conrad: The growth and morphology of epitaxial multilayer graphene. *Journal of Physics: Condensed Matter* **20**, 323202 (2008).

[82] N. Ruhe, J. Springborn, C. Heyn, M. Wilde, and D. Grundler: Simultaneous measurement of the de Haas-van Alphen and the Shubnikov-de Haas effect in a two-dimensional electron system. *Physical Review B* **74**, 235326 (2006).

[83] M. Wilde, M. Schwarz, C. Heyn, D. Heitmann, D. Grundler, D. Reuter, and A. Wieck: Experimental evidence of the ideal de Haas–van Alphen effect in a two-dimensional system. *Physical Review B* **73**, 125325 (2006).

[84] B. Rupprecht, S. Heedt, H. Hardtdegen, T. Schäpers, C. Heyn, M. Wilde, and D. Grundler: Frequency anomaly in the Rashba-effect induced magnetization oscillations of a high-mobility two-dimensional electron system. *Physical Review B* **87**, 035307 (2013).

[85] M. Brasse, S. M. Sauther, J. Falson, Y. Kozuka, A. Tsukazaki, C. Heyn, M. A. Wilde, M. Kawasaki, and D. Grundler: Enhanced quantum oscillatory magnetization and nonequilibrium currents in an interacting two-dimensional electron system in MgZnO/ZnO with repulsive scatterers. *Physical Review B* **89**, 075307 (2014).

[86] J. Jobst: private communication (Lehrstuhl für Angewandte Physik, Friedrich-Alexander-Universität Erlangen-Nürnberg, presently at Universiteit Leiden).

[87] M. Schwarz, D. Grundler, H. Rolff, M. Wilde, S. Groth, C. Heyn, and D. Heitmann: De Haas–van Alphen effect in a two-dimensional electron system. *Physica E: Low-dimensional Systems and Nanostructures* **12**, 140 (2002).

[88] M. P. Schwarz, D. Grundler, M. Wilde, C. Heyn, and D. Heitmann: Magnetization of semiconductor quantum dots. *Journal of Applied Physics* **91** (2002).

[89] M. P. Schwarz, M. Wilde, S. Groth, D. Grundler, C. Heyn, and D. Heitmann: Sawtoothlike de Haas–van Alphen oscillations of a two-dimensional electron system. *Physical Review B* **65**, 245315 (2002).

[90] M. P. Schwarz, D. Grundler, C. Heyn, D. Heitmann, D. Reuter, and A. Wieck: Induced nonequilibrium currents in the magnetization of mesoscopic dots in the quantum Hall regime. *Physical Review B* **68**, 245315 (2003).

[91] M. Wilde, J. Springborn, C. Heyn, D. Heitmann, and D. Grundler: Magnetization of GaAs quantum wires with quasi one-dimensional electron systems. *Physica E: Low-dimensional Systems and Nanostructures* **22**, 729 (2004).

[92] M. Wilde, M. Rhode, C. Heyn, D. Heitmann, D. Grundler, U. Zeitler, F. Schäffler, and R. Haug: Direct measurements of the spin and valley split-

tings in the magnetization of a $Si/SiGe$ quantum well in tilted magnetic fields. *Physical Review B* **72**, 165429 (2005).

[93] J. Springborn, N. Ruhe, C. Heyn, M. Wilde, D. Heitmann, and D. Grundler: Gate-controlled de Haas–van Alphen effect in an interacting two-dimensional electron system. *Physica E: Low-dimensional Systems and Nanostructures* **34**, 172 (2006).

[94] M. A. Wilde, J. I. Springborn, O. Roesler, N. Ruhe, M. P. Schwarz, D. Heitmann, and D. Grundler: Magnetometry on quantum Hall systems: Thermodynamic energy gaps and the density of states distribution. *physica status solidi (b)* **245**, 344 (2008).

[95] M. A. Wilde, D. Reuter, C. Heyn, A. D. Wieck, and D. Grundler: Inversion-asymmetry-induced spin splitting observed in the quantum oscillatory magnetization of a two-dimensional electron system. *Physical Review B* **79**, 125330 (2009).

[96] N. Ruhe, G. Stracke, C. Heyn, D. Heitmann, H. Hardtdegen, T. Schäpers, B. Rupprecht, M. Wilde, and D. Grundler: Origin and limiting mechanism of induced nonequilibrium currents in gated two-dimensional electron systems. *Physical Review B* **80**, 115336 (2009).

[97] T. Windisch, X. Huang, S. Dasgupta, B. Rupprecht, C. Heyn, M. Bichler, A. Fontcuberta i Morral, M. Grayson, G. Abstreiter, M. Wilde, and D. Grundler: De Haas-van Alphen effect and energy gaps of a correlated two-dimensional electron system in an AlAs two-valley pseudospin system. *Physical Review B* **80**, 205306 (2009).

[98] B. Rupprecht, W. Krenner, U. Wurstbauer, C. Heyn, T. Windisch, M. A. Wilde, W. Wegscheider, and D. Grundler: Magnetism in a Mn modulation-doped InAs/InGaAs heterostructure with a two-dimensional hole system. *Journal of Applied Physics* **107**, 093711 (2010).

[99] J. G. E. Harris, R. Knobel, K. D. Maranowski, A. C. Gossard, N. Samarth, and D. D. Awschalom: Magnetization Measurements of Magnetic Two-Dimensional Electron Gases. *Physical Review Letters* **86**, 4644 (2001).

[100] D. P. Weber, D. Rüffer, A. Buchter, F. Xue, E. Russo-Averchi, R. Huber, P. Berberich, J. Arbiol, A. Fontcuberta i Morral, D. Grundler, and M. Poggio: Cantilever Magnetometry of Individual Ni Nanotubes. *Nano Letters* **12**, 6139 (2012).

[101] J. G. E. Harris, D. D. Awschalom, F. Matsukura, H. Ohno, K. D. Maranowski, and A. C. Gossard: Integrated micromechanical cantilever magnetometry of $Ga_{1-x}Mn_xAs$. *Applied Physics Letters* **75**, 1140 (1999).

[102] D. W. Pohl: Dynamic piezoelectric translation devices. *Review of Scientific Instruments* **58**, 54 (1987).

[103] A. Tsukazaki, A. Ohtomo, T. Kita, Y. Ohno, H. Ohno, and M. Kawasaki: Quantum Hall Effect in Polar Oxide Heterostructures. *Science* **315**, 1388 (2007).

[104] M. Brasse, S. M. Sauther, J. Falson, Y. Kozuka, A. Tsukazaki, C. Heyn, M. A. Wilde, M. Kawasaki, and D. Grundler: Enhanced quantum oscillatory magnetization and nonequilibrium currents in an interacting two-dimensional electron system in MgZnO/ZnO with repulsive scatterers. *Physical Review B* **89**, 075307 (2014).

[105] R. Naslain: Crystal Chemistry of Boron and of Some Boron-Rich Phases; Preparation of Boron Modifications. In: V. Matkovich (Editor), *Boron and Refractory Borides*, pp. 139–202. Springer Berlin Heidelberg (1977).

[106] S. Veprek, R. Zhang, and A. Argon: Mechanical properties and hardness of boron and boron-rich solids. *Journal of Superhard Materials* **33**, 409 (2011).

[107] W. G. Jr. and S. Soffer: A galvanomagnetic investigation of TiB_2, NbB_2 and ZrB_2. *Journal of Physics and Chemistry of Solids* **36**, 627 (1975).

[108] D.-C. Tian and X.-B. Wang: Electronic structure and equation of state of TiB_2. *Journal of Physics: Condensed Matter* **4**, 8765 (1992).

[109] S. Aydin and M. Simsek: First-principles calculations of MnB_2, TcB_2, and ReB_2 within the ReB_2-type structure. *Physical Review B* **80**, 134107 (2009).

[110] H. J. Choi, D. Roundy, H. Sun, M. L. Cohen, and S. G. Louie: The origin of the anomalous superconducting properties of MgB_2. *Nature* **418**, 758 (2002).

[111] R. Barnes and R. Creel: Chromium-like antiferromagnetic behavior of CrB_2. *Physics Letters A* **29**, 203 (1969).

[112] J. Castaing, R. Caudron, G. Toupance, and P. Costa: Electronic structure of transition metal diborides. *Solid State Communications* **7**, 1453 (1969).

[113] D. Armstrong: The electronic structure of the first-row transition-metal diborides. *Theoretica chimica acta* **64**, 137 (1983).

[114] X.-B. Wang, D.-C. Tian, and L.-L. Wang: The electronic structure and chemical stability of the AlB_2-type transition-metal diborides. *Journal of Physics: Condensed Matter* **6**, 10185 (1994).

[115] P. Vajeeston, P. Ravindran, C. Ravi, and R. Asokamani: Electronic structure, bonding, and ground-state properties of AlB_2-type transition-metal diborides. *Physical Review B* **63**, 045115 (2001).

[116] I. Shein and A. Ivanovskii: Band structure of ZrB_2, VB_2, NbB_2, and TaB_2 hexagonal diborides: Comparison with superconducting MgB_2. *Physics of the Solid State* **44**, 1833 (2002).

[117] A. V. Fedorchenko, G. E. Grechnev, A. S. Panfilov, A. V. Logosha, I. V. Svechkarev, V. B. Filippov, A. B. Lyashchenko, and A. V. Evdokimova: Anisotropy of the magnetic properties and the electronic structure of transition-metal diborides. *Low Temperature Physics* **35** (2009).

[118] L. Voroshnin, L. Lyakhovich, G. Panich, and G. Protasevich: The structure of Fe-B alloys. *Metal Science and Heat Treatment* **12**, 732 (1970).

[119] S. T. Mahmud, A. K. M. A. Islam, and F. N. Islam: VB_2 and ZrB_2: a density functional study. *Journal of Physics: Condensed Matter* **16**, 2335 (2004).

[120] X. Zhou, H. Zhang, C. Cheng, J. Gao, G. Xu, Y. Li, and Y. Luo: First-principles study of structural, electronic and elastic properties of diboride of vanadium. *Physica B: Condensed Matter* **404**, 1527 (2009).

[121] A. Bauer: *Investigations of itinerant antiferromagnets and cubic chiral helimagnets*. Ph.D. thesis, Technische Universität München (2014).

[122] M. Cadeville: Proprietes magnetiques des diborures de manganese et de chrome: MnB_2 et CrB_2. *Journal of Physics and Chemistry of Solids* **27**, 667 (1966).

[123] L. Andersson, B. Dellby, and H. Myers: Ferromagnetic MnB_2. *Solid State Communications* **4**, 77 (1966).

[124] M. Kasaya, T. Hihara, and Y. Koi: NMR Study in MnB_2. *Journal of the Physical Society of Japan* **26**, 1549 (1969).

[125] E. Legrand and S. Neov: Neutron diffraction study of MnB_2. *Solid State Communications* **10**, 883 (1972).

[126] S. Khmelevskyi and P. Mohn: Magnetic ordering in MnB_2: an ab initio study. *Solid State Communications* **113**, 509 (2000).

[127] S. Khmelevskyi and P. Mohn: Covalent magnetism, exchange interactions and anisotropy of the high temperature layered antiferromagnet MnB_2. *Journal of Physics: Condensed Matter* **24**, 016001 (2012).

[128] A. R. Williams, R. Zeller, V. L. Moruzzi, C. D. Gelatt, and J. Kubler: Covalent magnetism: An alternative to the Stoner model. *Journal of Applied Physics* **52**, 2067 (1981).

[129] Y. Kitaoka, H. Yasuoka, T. Tanaka, and Y. Ishizawa: Nuclear magnetic resonance of ^{11}B in CrB_2. *Solid State Communications* **26**, 87 (1978).

[130] Y. Kitaoka and H. Yasuoka: NMR Investigations on the Spin Fluctuations in Itinerant Antiferromagnets III. CrB_2. *Journal of the Physical Society of Japan* **49**, 493 (1980).

[131] A. B. Karki, D. P. Gautreaux, J. Y. Chan, N. Harrison, D. A. Browne, R. G. Goodrich, and D. P. Young: Magnetotransport properties and the Fermi surface of single crystal VB_2. *Journal of Physics: Condensed Matter* **20**, 035209 (2008).

[132] V. B. Pluzhnikov, I. V. Svechkarev, A. V. Dukhnenko, A. V. Levchenko, V. B. Filippov, and A. Chopnik: de Haas–van Alphen effect in the diborides ScB_2, ZrB_2, and HfB_2. *Low Temperature Physics* **33**, 350 (2007).

[133] T. Tanaka, Y. Ishizawa, E. Bannai, and S. Kawai: Fermi surface measurement of ZrB_2 by the de Haas-van Alphen effect. *Solid State Communications* **26**, 879 (1978).

[134] T. Tanaka and Y. Ishizawa: The electron Fermi surface of HfB_2. In: *AIP Conference Proceedings*, vol. 231, p. 46 (1991).

[135] T. Tanaka and Y. Ishizawa: The de Haas-van Alphen effect in TiB_2. *Journal of Physics C: Solid State Physics* **13**, 6671 (1980).

[136] B. Arnold, S. Kasahara, A. Coldea, T. Terashima, Y. Matsuda, T. Shibauchi, and A. Carrington: Nesting of electron and hole Fermi surfaces in nonsuperconducting $BaFe_2P_2$. *Physical Review B* **83**, 220504 (2011).

[137] E. Yelland, J. Cooper, A. Carrington, N. Hussey, P. Meeson, S. Lee, A. Yamamoto, and S. Tajima: de Haas–van Alphen Effect in Single Crystal MgB_2. *Physical Review Letters* **88**, 217002 (2002).

[138] P. Blaha, K. Schwarz, G. Madsen, D. Kvasnicka, and J. Luitz: wien2k. *An augmented plane wave+ local orbitals program for calculating crystal properties* (2001).

[139] K. Schwarz, P. Blaha, and G. Madsen: Electronic structure calculations of solids using the WIEN2k package for material sciences. *Computer Physics Communications* **147**, 71 (2002).

[140] J. Kuneš and R. Laskowski: Magnetic ground state and Fermi surface of bcc Eu. *Physical Review B* **70**, 174415 (2004).

[141] P. Rourke and S. Julian: Numerical extraction of de Haas van Alphen frequencies from calculated band energies. *Computer Physics Communications* **183**, 235326 (2012).

[142] A. Wasserman and M. Springford: The influence of many-body interactions on the de Haas-van Alphen effect. *Advances in Physics* **45**, 471 (1996).

[143] I. Mazin and J. Kortus: Interpretation of the de Haas–van Alphen experiments in MgB_2. *Physical Review B* **65**, 180510 (2002).

[144] R. Heid, B. Renker, H. Schober, P. Adelmann, D. Ernst, and K.-P. Bohnen: Lattice dynamics and electron-phonon coupling in transition-metal diborides. *Physical Review B* **67**, 180510 (2003).

[145] A. Carrington, P. Meeson, J. Cooper, L. Balicas, N. Hussey, E. Yelland, S. Lee, A. Yamamoto, S. Tajima, S. Kazakov, et al.: Determination of the Fermi Surface of MgB_2 by the de Haas–van Alphen Effect. *Physical Review Letters* **91**, 037003 (2003).

[146] A. Regnat: private communication (chair E51, Physics Department, Technische Universität München).

[147] N. W. Ashcroft and N. D. Mermin: *Solid State Physics*. Cengage Learning (1976).

[148] S. Bud'ko, G. Lapertot, C. Petrovic, C. Cunningham, N. Anderson, and P. Canfield: Boron Isotope Effect in Superconducting MgB_2. *Physical Review Letters* **86**, 1877 (2001).

[149] D. Hinks, H. Claus, and J. Jorgensen: The complex nature of superconductivity in MgB_2 as revealed by the reduced total isotope effect. *Nature* **411**, 457 (2001).

[150] M. Tinkham: *Introduction to superconductivity*. McCraw-Hill, New York (1996).

[151] H. Harima: Energy band structures of MgB_2 and related compounds. *Physica C: Superconductivity* **378-381**, 18 (2002).

[152] H. Rosner, J. An, W. Pickett, and S.-L. Drechsler: Fermi surfaces of diborides: MgB_2 and ZrB_2. *Physical Review B* **66**, 024521 (2002).

[153] X. X. Xi: Two-band superconductor magnesium diboride. *Reports on Progress in Physics* **71**, 116501 (2008).

[154] A. Liu, I. Mazin, and J. Kortus: Beyond Eliashberg Superconductivity in MgB_2: Anharmonicity, Two-Phonon Scattering, and Multiple Gaps. *Physical Review Letters* **87**, 087005 (2001).

[155] S. V. Shulga, S.-L. Drechsler, H. Eschrig, H. Rosner, and W. E. Pickett: The upper critical field problem in MgB_2. *eprint arXiv:cond-mat/0103154* (2001).

[156] F. Bouquet, Y. Wang, R. A. Fisher, D. G. Hinks, J. D. Jorgensen, A. Junod, and N. E. Phillips: Phenomenological two-gap model for the specific heat of MgB_2. *Europhysics Letters* **56**, 856 (2001).

[157] A. A. Golubov, J. Kortus, O. V. Dolgov, O. Jepsen, Y. Kong, O. K. Andersen, B. J. Gibson, K. Ahn, and R. K. Kremer: Specific heat of MgB_2 in a one- and a two-band model from first-principles calculations. *Journal of Physics: Condensed Matter* **14**, 1353 (2002).

[158] J. An and W. Pickett: Superconductivity of MgB_2: Covalent Bonds Driven Metallic. *Physical Review Letters* **86**, 4366 (2001).

[159] J. Kortus, I. Mazin, K. Belashchenko, V. Antropov, and L. Boyer: Superconductivity of Metallic Boron in MgB_2. *Physical Review Letters* **86**, 4656 (2001).

[160] K. Belashchenko, M. Schilfgaarde, and V. Antropov: Coexistence of covalent and metallic bonding in the boron intercalation superconductor MgB_2. *Physical Review B* **64**, 092503 (2001).

[161] I. I. Mazin, O. K. Andersen, O. Jepsen, O. V. Dolgov, J. Kortus, A. A. Golubov, A. B. Kuz'menko, and D. van der Marel: Superconductivity in MgB_2: Clean or Dirty? *Physical Review Letters* **89**, 107002 (2002).

[162] J. Cooper, A. Carrington, P. Meeson, E. Yelland, N. Hussey, L. Balicas, S. Tajima, S. Lee, S. Kazakov, and J. Karpinski: de Haas–van Alphen effect in MgB_2 crystals. *Physica C: Superconductivity* **385**, 75 (2003).

[163] C. Chen: *Graphene NanoElectroMechanical Resonators and Oscillators*. Ph.D. thesis, Columbia University (2013).

Acknowledgments

I would like to express my gratitude to all the people who contributed to this work and supported me during my Ph. D. time. In particular:

- Prof. Dr. Martin Zacharias for supervision of the Ph. D. examination, Prof. Dr. Dirk Grundler for being the first examiner, and Prof. Dr. Christian Pfleiderer for being the second examiner.
- Prof. Dr. Dirk Grundler for giving me the opportunity to work in his group and for the supervision of this thesis. I thank him for the many fruitful discussions and the great support of his students without any reservations.
- Dr. Marc Wilde for his overall support and guidance throughout this work. I thank him for countless fruitful discussions. He always has an eye not only for interesting open scientific questions, but also a realistic view of practical feasibility, and his door is always open.
- Matthias Brasse, Florian Herzog, Schorsch Sauther, and Benedikt Rupprecht, the cantilever coworkers, for their helping hands and great support. In particular, I thank Matthias for guiding me, a former theorist, in many practical aspects of lab work and showing me the tricks of cantilever magnetometry in the early stages of my work.
- Stefanos Chalkidis and Matthias Block for their commitment and contributions to this work.
- Andreas Bauer, Alexander Regnat, and Prof. Christian Pfleiderer for providing me with the VB_2 and the MnB_2 sample, MnB_2 structural data, and illuminating scientific discussions.
- Dr. Jan Kuneš, Academy of Sciences, Prague, Czech Republic, for providing the band structure calculations of VB_2 and MnB_2 and for answering many questions via e-mail and phone. Unfortunately, I did not have the chance to meet him in person and share with him my experiences and views on alpine rock climbing.

- Florian Speck, Felix Fromm, and Prof. Thomas Seyller for growth and Raman characterization of the epitaxial graphene samples. Due to our tiny sample sizes requiring very slow pumping and flushing of the furnace, Florian and Felix had to devote a lot of time. Stefanos and I enjoyed their professional, yet laid-back Franconian approach to doing research and the evening "kellerbier".

- Max Seifert, Lucas Hess, and PD José Antonio Garrido for swiftly providing CVD graphene samples.

- Dr. Yusuke Kozuka and Prof. Masashi Kawasaki, University of Tokyo, Japan, for providing me with MgZnO/ZnO samples and transport pre-characterization.

- Claudine Voelcker, Stephan Lichtenauer, Thomas Neukel, Thomas Rapp, Johannes Seitz, and Herbert Hetzl from the E10 technical and organizational staff, for organizational support, quick technical solutions, and for thousands of liter of liquid helium.

- Sebastian Neusser, Georg Dürr, Rupert Huber, Thomas Schwarze, Florian Brandl, Florian Heimbach, Yannis Stasinopoulus, Stefan Mändl, Haiming Yu, and all diploma, M. Sc., B. Sc., and exchange students for the exceptionally good and enjoyable working atmosphere at E10, and the laughs we shared in the labs and offices and during numerous coffee breaks.

- Needless to say, my family and my friends for their unlimited support and constant encouragement, especially after my accident.

This research has received funding from the Priority Program 1459: *Graphene* and from Transregio Program TRR 80: *From Electronic Correlations to Functionality* of Deutsche Forschungsgemeinschaft, which is gratefully acknowledged.